

Numerical methods in
stochastic and two-scale
shape optimization

Dissertation
zur
Erlangung des Doktorgrades (Dr. rer. nat.)
der
Mathematisch-Naturwissenschaftlichen Fakultät
der
Rheinischen Friedrich-Wilhelms-Universität Bonn

vorgelegt von
Sascha Tölkes
aus
Trier

Bonn, 2017

Angefertigt mit Genehmigung der Mathematisch-Naturwissenschaftlichen Fakultät der
Rheinischen Friedrich-Wilhelms-Universität Bonn

1. Gutachter: Prof. Dr. Martin Rumpf
2. Gutachter: Prof. Dr. Rüdiger Schultz

Tag der Promotion: 11. April 2018
Erscheinungsjahr: 2018

Abstract

In this thesis, three different models of elastic shape optimization are described. All models use phase fields to describe the elastic shapes and regularize the interface length on some level or scale to control fine-scale structures.

First, the paradigm of stochastic dominance is transferred from finite dimensional stochastic programming to elastic shape optimization under stochastic loads. The shapes are optimized under the constraint, that they dominate a given benchmark shape in a certain stochastic order. This allows for a flexible risk aversion comparison. Risk aversion is handled in the constraint rather than the objective functional, which results in an optimization over a subset of admissible shapes only. First and second order stochastic dominance constraints are examined and compared. An (adaptive) Q^1 finite element scheme is used, that was implemented for two of the models described in this thesis and is introduced here. Several stochastic loads setups and benchmark variables are discretized and optimized.

Starting with the observation that unregularized elastic shape optimization methods create arbitrarily fine microstructures in many scenarios, domains composited of a number of geometrical subdomains with prescribed boundary conditions are considered in the second model. A reference subdomain is mapped to each type of geometrical subdomains to optimize computational complexity. These are suitable to model fine scale elastic structures, that are widespread in nature. Examples are fine-scale structures in bones or plants, resulting from the need for a stiff and low-weight structure. The subdomains are coupled to simulate fine-scale structures as they appear e. g. in bones (branching periodic structures). The elastic shape is optimized only for those reference subdomains, simulating periodically repeating structures in one or more coordinate directions. The stress is supposed to be continuous over the domain. A stress-based finite volume discretization and an alternating optimization algorithm are used to find optimal elastic structures for compression and shear loads.

Finally, a model considering a fine-scale material in which the elastic shape is modeled by a phase field on the microscale is introduced. This approach further investigates the fine-scale structures mentioned above and allows for a comparison with laminated materials and previous work on homogenization. A short introduction into homogenization is given and the two-scale energies required for the optimization are derived and discretized. An estimation of the scale between macro- and microscale is derived and a finite element discretization using the Heterogeneous Multiscale Method is introduced. Numerical results for compression and shear loads are presented.

Contents

1. Introduction	3
2. Background and fundamentals	6
2.1. Preliminaries	6
2.2. An introduction to elasticity	9
2.3. Elastic materials	11
2.3.1. Isotropic materials	12
2.4. Introduction to shape optimization	16
2.5. Phase fields	17
2.5.1. Volume measurements	17
2.5.2. Interface length	18
2.5.3. Applications to shape optimization	20
3. Stochastic dominance constraints in shape optimization	22
3.1. Basic concepts of stochastic dominance	23
3.1.1. Stochastic orderings	24
3.1.2. Stochastic dominance	27
3.2. Application to discrete stochastic variables	29
3.3. The stochastic dominance problem	31
3.4. Discretization	32
3.4.1. Discretization of energies	35
3.5. Numerical Results	37
3.6. Conclusion	39
4. Composite materials and branching structures	43
4.1. Problem formulation	43
4.1.1. Elastic energy and compliance	45
4.2. Discretization	48
4.2.1. The alternating algorithm	52
4.3. Results	54
4.3.1. A simple example	56
4.3.2. Symmetry assumptions	56
4.3.3. Additional layers	56
4.3.4. Results	58
4.4. Conclusion	59

5. Fine-scale elastic shape optimization	67
5.1. Elasticity of a fine-scale material	68
5.2. Shape optimization	70
5.2.1. Deterministic fine-scale shape optimization	70
5.3. Finite element discretization	75
5.3.1. The discrete problem	76
5.4. Specific patterns on the micro-scale	79
5.4.1. Low-dimension optimization problem	82
5.5. Results	83
5.5.1. Compression load	84
5.5.2. Shear load	84
5.6. Conclusion	85
 Appendices	 86
A. Derivatives of two-scale functionals	87
A.1. Continuous quantities	87
A.2. Discretized quantities	89
 Bibliography	 93

List of Figures

1.1. Examples of optimal shapes	4
3.1. CDF of random variables used in stochastic dominance example	28
3.2. Quad-tree and corresponding mesh	33
3.3. Sketch of mesh refinement	33
3.4. Stochastic dominance results cantilever	40
3.5. Stresses for stochastic dominance results cantilever	41
3.6. Stochastic dominance results carrier plate	42
3.7. Stresses for stochastic dominance results carrier plate	42
4.1. Different local subdomain configurations of a single facet	44
4.2. Sketch of composite domain	45
4.3. Discretization of forces and edge numbering	49
4.4. Decomposition of quadratic domain using 4 and 5 reference subdomains . .	57
4.5. Decomposition of quadratic domain using 9 and 13 reference subdomains .	57
4.6. Types of loads	58
4.7. Result for compression loads on domain composed of 4 and 5 reference subdomains	61
4.8. Result for compression loads on domain composed of 9 reference subdomains	62
4.9. Result for compression loads on domain composed of 13 reference subdomains	63
4.10. Result for shear loads on domain composed of 4 and 5 reference subdomains	64
4.11. Result for shear loads on domain composed of 9 reference subdomains . . .	65
4.12. Result for shear loads on domain composed of 13 reference subdomains . .	66
5.1. Translation of stresses into microscopic affine displacements	69
5.2. HMM finite elements	76
5.3. Sketch periodic structure and cells	80
5.4. Results for fine-scale compression load scenario	84
5.5. Results for fine-scale shear load scenario	85

List of Tables

2.1. Notation used throughout this thesis.	7
3.1. Price overview for stochastic dominance example	28

Acknowledgements

I would like to express my deep gratitude to my advisor Prof. Dr. Martin Rumpf, who introduced me to shape optimization and many other interesting topics in numerical mathematics. I would like to thank him for his constant support and excellent guidance throughout the past years.

I am deeply grateful to Prof. Dr. Sergio Conti for his advice and great support throughout the years and his mentoring of my Ph.D. studies.

Furthermore, I am thankful to Prof. Dr. Rüdiger Schultz for co-reviewing this thesis.

Special thanks go to my former office mate Benedict Geihe for his advice and many discussions, that helped me understand many areas of mathematics. Furthermore, I'd like to thank (in alphabetical order) Prof. Dr. Benjamin Berkels, Alexander Effland, Dr. Martina Franken, Dr. Behrend Heeren, Pascal Huber, Dr. Martin Lenz, Nora Lüthen, Dr. Simplicie Nemadjieu, Dr. Nadine Balzani, Dr. Ricardo Perl, Stefan Simon, Gabriele Sodoge–Stork, Dr. Orestis Vantzos and Prof. Dr. Benedikt Wirth.

Finally, I am thankful to my family for their support and encouragement.

I gratefully acknowledge the support of the Bonn International Graduate School of Mathematics (BIGS) and the CRC 1060 at the University of Bonn.

1. Introduction

In this thesis, we will study several problems in the context of elastic shape optimization. In general, shape optimization aims to find an optimal shape for a certain task, for instance, a shape that withstands certain forces as well as possible. The methods used to model and solve those shape optimization problems are similar to the methods used in the context of optimal control. To be precise, shape optimization can be seen as an application of optimal control, where the control variables model the shape.

In this thesis, we will discuss three problems in the context of shape optimization: A model for stochastic dominance constraint shape optimization, an approach to modeling and optimizing branching patterns (fine patterns that appear e.g. in the spongiosa of bones) in elastic materials and an approach to modeling fine-scale elastic materials where arbitrary periodic structures can be built by the optimization on the micro-scale. All models optimize shapes under the constraint, that the partial differential equation of linear elasticity is solved (under given boundary conditions). The stochastic dominance and fine-scale model use a strain-based formulation and can be seen as extensions of work by [PRW12]. The branching model uses a stress-based formulation, which allows for an easier introduction of the required branching type boundary conditions.

Shape optimization problems, in general, are a special kind of optimal control problems and have been studied in many different contexts, e.g. aero- [RJA⁺99, Sam04] and hydrodynamics [DM01, HS07, NA16] and elasticity. In the context of elasticity and linear elasticity, there is a multitude of approaches to represent the domain [DHR98, SW00, All02, LKH05, AVCT07, AJ05, AD14, AD15], different boundary conditions (deterministic and stochastic) and target functionals (e.g. compliance and tracking type). The boundary conditions of the elastic problem determine the load scenario that is simulated. Deterministic load scenarios define a single load for each point of the boundary, while stochastic load scenarios prescribe a set of loads and assigned probabilities, simulating a set of scenarios that have potentially different probabilities to be realized. This kind of boundary conditions allows for a wider variety of simulations and can be modeled in an energy term that is either part of the target functional or can be used as a constraint, which in turn allows for comparisons between different shapes and leads to the notion of stochastic dominance (cf. [MS02]).

Figure 1.1 depicts the result of a one-scale optimization for a single (deterministic) load scenario in which the shape is clamped on the lower boundary and a force is applied to the upper boundary. On the upper boundary of both shapes, a small strip of material is fixed. The structures consist of a hard material (black) and a much softer material (white). The setup for both shapes is identical up to the constant that weights a term

1. Introduction

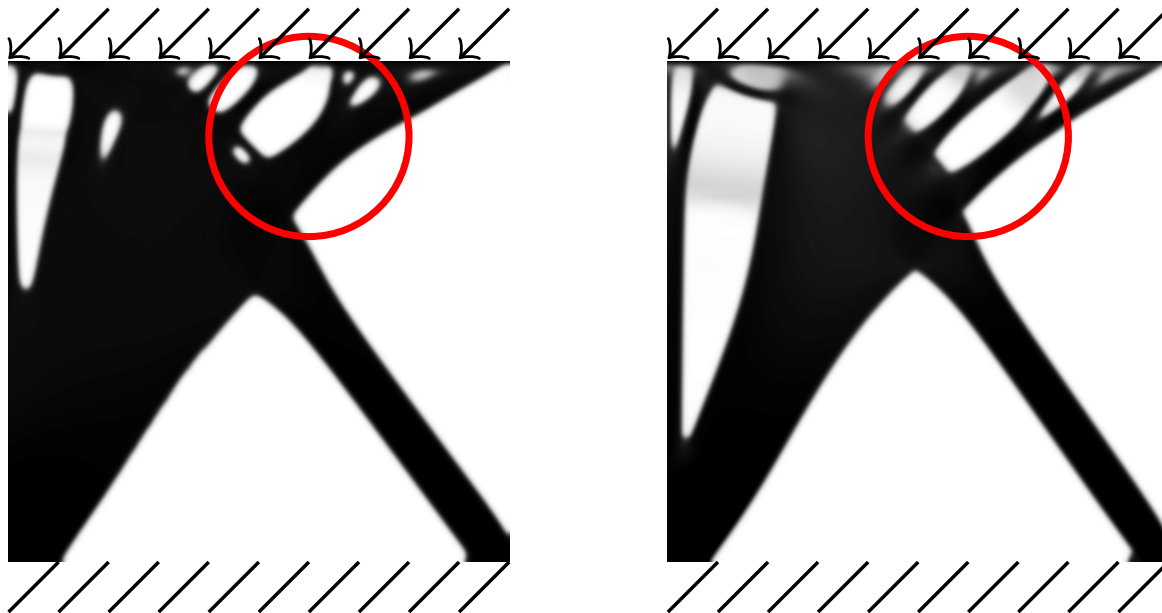


Figure 1.1.: Examples of optimal shapes for a pressure plate scenario. The amount of fine-scale structure in the optimal shape depends on the weighting of the interface-length measuring term.

measuring the interface length between the two materials. That constant is β for the left shape and $\frac{1}{2}\beta$ for the right shape and its change induces finer structures in the right shape (s. red circle: an additional beam has formed). Further reducing this weight leads to even finer (and potentially arbitrarily fine) structures. For many scenarios, this kind of fine-scale structure is optimal, depending on the forces and the domain. The scale of the optimal structure can be arbitrarily small for many combinations of domains and forces, resulting in problems that are not well-posed. This fact necessitates the introduction of a regularizing term that introduces the length of the interface between the two materials into the cost functional and controls the formation of microstructure. Without such a term, arbitrarily fine microstructures might exist in the optimal shape, but the associated characteristic function to such shapes only converges weakly (not strongly) to its limit, which makes them unfit for the models discussed in this thesis and related work.

The structures in Figure 1.1 show some regions where the material is neither hard (black) nor soft (white), but a (gray) “interphase” region. This is due to the discretization using phase fields. The size of these transitional regions between hard and soft material is also controlled by the interface term, that regularizes the shape via the interface length. Cf. Section 2.5 for an introduction to phase fields and how the shapes converge towards the pure phases of hard and soft material.

This thesis is organized as follows: In this chapter, we will describe some fundamental principles and theorems used by the models described in later chapters. In Section 2.5 we will introduce phase fields and describe how to control the length of the interface

and the size of the transitional “interphase” regions. Compared to other methods of shape encoding, phase field functions can easily handle the formation of new holes in the described shapes but introduce this kind of transitional region between the two phases, which has to be regarded as a mix of phases instead of pure phases. Still, the size of these transitional regions can be controlled. A Γ -convergence result for a term approximating the interface length will be given and it will be shown, that the phase field tends toward a shape containing the pure phases only.

In Chapter 3 we will describe a strain-based model of stochastic shape optimization using linear elasticity in the context of stochastic dominance constraints. As in the other models considered in this thesis, we try to determine which structures are necessary to support given loads and which microstructures form for given boundary conditions. As mentioned above, we use the partial differential equation of linear elasticity (as opposed to the full hyperelastic equation). This choice is justified by the fact that for all scenarios considered the deformations are small, which makes the linearization of the hyperelastic equation a good approximation. Furthermore, the linear elastic equation removes ambiguities created by non-unique solutions of the hyperelastic equation, as e.g. buckling effects do not appear when using the linear terms only. Additionally, we will describe an adaptive \mathcal{Q}^1 finite element scheme for the discretization of this model.

Next, in Chapter 4 we will consider a stress-based model of the formation of branching periodic structures in domains composited of periodic, branching periodic and non-periodic elastic cells. This model will be discretized using a finite volume approach and optimized using an alternating method. A suitable approach to handle singular matrices that result from conditions to the forces will be introduced.

Finally, in Chapter 5 we will discuss a strain-based model of fine-scale linear elastic shape optimization and compare the resulting shapes to the results presented in work by Allaire et. al. [All02]. We have to note, that even the fine-scale model discussed in this thesis has a fixed scale between the microscopic and macroscopic scales. Still, this model fits into the context of shape optimization using the homogenization method (s. [All02]), which describes the optimal microstructure in the (arbitrarily fine) limit. This structure is always given by rank- d laminates, where d is the space dimension. For the discretization, we will use a \mathcal{Q}^1 finite element Heterogeneous Multiscale Method (HMM).

2. Background and fundamentals

This thesis makes constant use of the theory of linear elasticity. In this chapter, we will introduce its basic concepts and properties and its application to shape optimization. These concepts will be used later to define different models in the context of linear elastic shape optimization. We will use the linear formulation of elasticity instead of the full (hyperelastic) equation, as this form prevents non-unique deformations — like buckling instabilities — that are introduced by the higher order terms. For small deformations (which are usually caused by small loads, s. also [Cia88]), linear elasticity is a good approximation of the full elastic equation.

2.1. Preliminaries

In this section, we introduce some general definitions, which are used throughout this thesis.

We introduce some general notation in Table 2.1. and some basic norms and function spaces in the following pages: Let $\alpha = (\alpha_1, \dots, \alpha_n) \in \mathbb{N}^n$ be a multi-index. Define $\partial_\alpha f = \partial_1^{\alpha_1} \dots \partial_n^{\alpha_n} f$ and $|\alpha| = \sum_{i=1}^n \alpha_i$. Let $k \in \mathbb{N} \cup \{\infty\}$. We define the spaces of *continuous* and *continuously differentiable* functions on a closed domain $\bar{\mathcal{D}}$ as $C^k(\bar{\mathcal{D}})$. The associated norm is

$$\|f\|_{C^0(\bar{\mathcal{D}})} = \sup_{x \in \bar{\mathcal{D}}} |f(x)| \text{ and}$$

$$\|f\|_{C^k(\bar{\mathcal{D}})} = \sum_{|\alpha| \leq k} \|\partial_\alpha f\|_{C^0(\bar{\mathcal{D}})}.$$

$C^\infty(\bar{\mathcal{D}}) := \bigcap_{k \geq 0} C^k(\bar{\mathcal{D}})$ denotes the Banach space, that contains functions for which $\partial_\alpha f$ is continuous and bounded in $C^0(\bar{\mathcal{D}})$ for all α for which $0 \leq |\alpha| \leq k$ holds for any k .

We use the standard notation for Lebesgue and Sobolev spaces on open Lipschitz-domains \mathcal{D} [AF03]: $L^p(\mathcal{D})$ and $W^{m,p}(\mathcal{D})$ for $m \in \mathbb{N}$ and $p \in [1, \infty]$. Furthermore, we define for any $m \geq 1$ and $f, g \in W^{m,2}(\mathcal{D})$, the scalar product

$$D^m f \cdot D^m g = \sum_{x_1, \dots, x_m}^n \partial_{x_1, \dots, x_m} f \cdot \partial_{x_1, \dots, x_m} g$$

and the seminorm

$$|D^m f| = (D^m f \cdot D^m f)^{\frac{1}{2}}.$$

$\mathbb{R}^{m \times n}$	the space of $m \times n$ matrices
$\mathbb{R}_{\text{sym}}^{n \times n}$	the space of symmetric $n \times n$ matrices
$\mathbb{R}_{\text{sym},+}^{n \times n}$	the space of symmetric $n \times n$ matrices with positive determinant and
$\mathbb{R}_{\text{sym},>}^{n \times n}$	the space of symmetric positive definite matrices.
$A : B = \sum_{ij} A_{ij} B_{ij}$	the component-wise multiplication for $A, B \in \mathbb{R}^{m \times m}$
C	a fourth-order elasticity tensor, often a Lamé–Navier type tensor,
\mathbf{D}	the Jacobian operator
∂_i	partial differentials in the i -th component,
d	the spatial dimension,
\mathcal{D}	an open Lipschitz-domain in \mathbb{R}^d ,
$\Gamma_D \subset \partial\mathcal{D}$	a boundary part where Dirichlet type boundary conditions are applied,
$\Gamma_N \subset \partial\mathcal{D}$	a boundary part, where Neumann boundary conditions are applied,
ϕ	deformations,
u	displacements,
v	a phase field variable,
χ	a characteristic function,
\mathcal{E}, \mathcal{J} and other calligraphic capital letters	functionals,
\mathbf{E}, \mathbf{J} and other bold face capital letters	discrete functionals,
\mathcal{H}^n	n -dimensional Hausdorff measure.

Table 2.1.: Notation used throughout this thesis.

The associated norms are denoted using $\|\cdot\|$ and can be defined as

$$\|f\|_{L^p(\mathcal{D})} = \left(\int_{\mathcal{D}} |f|^p \right)^{\frac{1}{p}} \text{ for } 1 \leq p < \infty \text{ and } \|f\|_{L^\infty(\mathcal{D})} = \inf_{N \subset \mathcal{D}, |N|=0} \sup_{x \in \mathcal{D} \setminus N} |f(x)|,$$

$$\|f\|_{W^{m,p}(\mathcal{D})} = \|D^m f\|_{L^p(\mathcal{D})},$$

$$\|f\|_{W^{m,p}(\mathcal{D})} = \left(\sum_{i=0}^m |f|_{W^{i,p}(\mathcal{D})}^p \right)^{\frac{1}{p}} \text{ for } 1 \leq p < \infty \text{ and}$$

$$\|f\|_{W^{m,\infty}(\mathcal{D})} = \max_{0 \leq l \leq m} \|D^l f\|_{L^\infty(\mathcal{D})}.$$

In the first equation, $|N|$ denotes the measure of the set N . $W_0^{m,2}(\mathcal{D})$ is defined as the

2. Background and fundamentals

closure of $C_c^\infty(\mathcal{D}) := \{f \in C^\infty : \text{supp } f \text{ is compact}\}$ with respect to the norm $\|\cdot\|_{W^{m,2}(\mathcal{D})}$ and $W^{0,p}(\mathcal{D}) = L^p(\mathcal{D})$.

To conclude this introduction on Sobolev-spaces, we state the embedding theorem for Sobolev- and Hölder functions.

Theorem 1. *Let $\mathcal{D} \subset \mathbb{R}^d$ be a non-empty, open, bounded Lipschitz domain.*

- *Let $m_1, m_2 \in \mathbb{N}$ and $p_1, p_2 \in [1, \infty)$ with*

$$m_1 - \frac{d}{p_1} \geq m_2 - \frac{d}{p_2} \text{ and } m_1 \geq m_2 .$$

Then a continuous embedding $W^{m_1, p_1}(\mathcal{D}) \hookrightarrow W^{m_2, p_2}$ exists and for all $f \in W^{m_1, p_1}$ and

$$\|f\|_{W^{m_2, p_2}} \leq C(\mathcal{D}, d, m_1, m_2, p_1, p_2) \|f\|_{W^{m_1, p_1}} .$$

If both inequalities are strict, then the embedding is compact.

- *Let $m \in \mathbb{N}^+$ and $p \in [1, \infty)$ and for any $\alpha \in (0, 1), k \in \mathbb{N}$*

$$m - \frac{d}{p} \geq k + \alpha .$$

Then, a continuous embedding $W^{m, p}(\mathcal{D}) \hookrightarrow C^{k, \alpha}(\bar{\mathcal{D}})$ exists, such that for all $f \in W^{m, p}(\mathcal{D})$ a representative \bar{f} of f exists, that fulfills $\bar{f}(x) = f(x)$ for almost every $x \in \mathcal{D}$ and

$$\|\bar{f}\|_{C^{k, \alpha}(\bar{\mathcal{D}})} \leq C(\mathcal{D}, d, m, p, k, \alpha) \|\bar{f}\|_{W^{m, p}(\mathcal{D})} .$$

If the inequality is strict, then the embedding is compact.

Proof. S. [Alt06, AF03] □

For numerical simulations, we will use finite elements on quadratic elements. Let τ denote a mesh consisting of quadratic elements, i. e. a set of elements $[a, b] \times [c, d] =: T \in \tau$ for $a, b, c, d \in \mathbb{R}$ with $b - a = d - c$ fulfilling $T_i \cap T_j = \emptyset$ for all $T_i, T_j \in \tau$ and $\cup_{T \in \tau} T = \mathcal{D}_h$ for a discretized version \mathcal{D}_h of \mathcal{D} . Denote $h := \min_{a, b} \{b - a\}$. The finite element functions will be *multilinear*, i. e. in two dimensions *bilinear*. The respective function space is defined as

$$Q_h^1(\mathcal{D}_h) = \{\phi : \mathcal{D} \rightarrow \mathbb{R} : \phi \in C_0(\mathcal{D}), \forall T \in \tau \phi|_T(x_1, x_2) = \phi_1(x_1)\phi_2(x_2), \phi_1 \text{ and } \phi_2 \text{ affine}\}$$

and consist of the functions that are continuous on \mathcal{D}_h and are affine in each coordinate direction on each element.

2.2. An introduction to elasticity

Elasticity theory aims to describe the properties of an elastic body using a partial differential equation, utilizing a deformation of or a displacement from (equivalent) a reference configuration. First, we introduce a basic concept of elasticity theory, that guarantees some properties of elastic stresses and their relationship to forces. In this introduction, we will follow along the lines of [Cia88]. We begin by introducing an important axiom.

Axiom 1 (Cauchy-Euler stress principle, cf. [Cia88, Axiom 2.2-1]). *Consider the deformed configuration $\bar{\mathcal{D}}^\varphi$ of an elastic body subject to forces, that are represented by densities $f^\varphi : \mathcal{D}^\varphi \rightarrow \mathbb{R}^3$ and $g^\varphi : \Gamma_N^\varphi \rightarrow \mathbb{R}^3$. Then a vector field $t^\varphi : \bar{\mathcal{D}}^\varphi \times \{v \in \mathbb{R}^3 : \|v\| = 1\} \rightarrow \mathbb{R}^3$ exists, that fulfills for any subdomain $A^\varphi \subset \bar{\mathcal{D}}^\varphi$:*

1. *At any point x^φ where the outer normal n^φ exists*

$$t^\varphi(x^\varphi, n^\varphi) = g^\varphi(x^\varphi)$$

holds,

2. *force balance is preserved:*

$$\int_{A^\varphi} f^\varphi(x^\varphi) dx^\varphi + \int_{\partial A^\varphi} t^\varphi(x^\varphi, n^\varphi) da^\varphi = 0,$$

where n^φ is the normal to ∂A^φ ,

3. *the angular moment balance is preserved:*

$$\int_{A^\varphi} x^\varphi \times f^\varphi(x^\varphi) dx^\varphi + \int_{\partial A^\varphi} x^\varphi \times t^\varphi(x^\varphi, n^\varphi) da^\varphi = 0.$$

The Cauchy-Euler stress principle asserts — among other things — the existence of elementary surface forces along the boundaries of all domains of the reference configuration. Among the consequences of the stress principle are the linearity and symmetry of the stress tensor, which are described in a theorem by Cauchy.

Theorem 2 (Cauchy's theorem, adapted from [Cia88, Theorem 2.3-1]). *Consider a continuously applied body force density $f^\varphi : \bar{\mathcal{D}}^\varphi \rightarrow \mathbb{R}^3$ and let the Cauchy stress vector field t^φ be continuously differentiable with respect to x^φ for each $n \in \{v \in \mathbb{R}^3 : \|v\| = 1\}$ and continuous with respect to n for each $x^\varphi \in \bar{\mathcal{D}}^\varphi$. Then the axioms of force and moment balance imply that a continuously differentiable tensor field*

$$T^\varphi : x^\varphi \in \bar{\mathcal{D}}^\varphi \rightarrow T^\varphi(x^\varphi) \in \mathbb{R}^{3 \times 3}$$

exists, such that

$$t^\varphi(x^\varphi, n) = T^\varphi(x^\varphi)n$$

2. Background and fundamentals

for all $x^\varphi \in \bar{\mathcal{D}}^\varphi$ and all $n \in \{v \in \mathbb{R}^3 : \|v\| = 1\}$. Furthermore

$$\begin{aligned} -\operatorname{div}^\varphi T^\varphi(x^\varphi) &= f^\varphi(x^\varphi) && \text{for all } x^\varphi \in \mathcal{D}^\varphi, \\ T^\varphi(x^\varphi) &= T^\varphi(x^\varphi)^T && \text{for all } x^\varphi \in \bar{\mathcal{D}}^\varphi, \\ T^\varphi(x^\varphi)n^\varphi &= g^\varphi(x^\varphi) && \text{for all } x^\varphi \in \Gamma_N^\varphi. \end{aligned}$$

The symmetric tensor $T^\varphi(\varphi^\varphi)$ is called the *Cauchy stress tensor* at $x^\varphi \in \bar{\mathcal{D}}^\varphi$. The quantities above have all been expressed in terms of variables on the deformed domain. As the deformation is one of the unknowns, a formulation based on variables on the reference domain would be preferable, which is fixed and given.

Consider the *Piola transform* $T : \bar{\mathcal{D}} \rightarrow \mathbb{R}^{3 \times 3}$ of a tensor field T^φ and the resulting equations

$$T(x) = (\det \nabla \varphi(x)) T^\varphi(x^\varphi) \nabla \varphi(x)^{-T}$$

for the *first Piola-Kirchhoff stress tensor* and

$$\operatorname{div} T(x) = (\det \nabla \varphi(x)) \operatorname{div}^\varphi T^\varphi(x^\varphi)$$

for its divergence. As $T(x)^T = \nabla \varphi(x)^{-1} T(X) \nabla \varphi(x)^T$, the tensor $T(x)$ is not symmetric. Still, a symmetric stress tensor is desirable as it simplifies the constitutive equation. Thus, we define the *second Piola-Kirchhoff stress tensor*

$$\Sigma(x) = \nabla \varphi(x)^{-1} T(x) = (\det \nabla \varphi(x)) \nabla \varphi(x)^{-1} T^\varphi(x^\varphi) \nabla \varphi(x)^{-T}.$$

Theorem 3 (adapted from [Cia88, Theorems 2.6-1 and 2.6-2]). *The first Piola-Kirchhoff stress tensor satisfies*

$$\begin{aligned} -\operatorname{div} T(x) &= f(x) && \text{for all } x \in \mathcal{D}, \\ \nabla \varphi(x) T(x) &= T(x) \nabla \varphi(x)^T && \text{for all } x \in \mathcal{D}, \\ T(x) n &= g(x) && \text{for all } x \in \Gamma_N. \end{aligned}$$

The first and third equations combined are equivalent to

$$\int_{\mathcal{D}} T : \nabla \theta \, dx = \int_{\mathcal{D}} f \cdot \theta \, dx + \int_{\Gamma_N} g \cdot \theta \, da$$

for all sufficiently smooth vector fields $\theta : \bar{\mathcal{D}} \rightarrow \mathbb{R}^3$ which satisfy $\theta = 0$ on Γ_D .

The second Piola-Kirchhoff stress tensor satisfies

$$\begin{aligned} -\operatorname{div}(\nabla \varphi(x) \Sigma(x)) &= f(x) && \text{for all } x \in \mathcal{D} \\ \Sigma(x) &= \Sigma(x)^T && \text{for all } x \in \mathcal{D} \\ \nabla \varphi(x) \Sigma(x) n &= g(x) && \text{for all } x \in \Gamma_N. \end{aligned}$$

The first and third equations combined are equivalent to

$$\int_{\mathcal{D}} \nabla \varphi(x) \Sigma(x) : \nabla \theta \, dx = \int_{\mathcal{D}} f \cdot \theta \, dx + \int_{\Gamma_N} g \cdot \theta \, da,$$

with θ as above.

2.3. Elastic materials

A material is *elastic* if a mapping

$$\hat{T}^r : (x, F) \in \bar{\mathcal{D}} \times \mathbb{R}_{\text{sym},+}^{3 \times 3} \rightarrow \hat{T}(x, F) \in \mathbb{R}_{\text{sym}}^{3 \times 3}$$

exists, such that in any deformed configuration that a body of the considered material can occupy, the Cauchy stress tensor $T^\varphi(x^\varphi)$ (where $x^\varphi = \varphi(x)$) is related to the gradient $\nabla\varphi(x)$ at the point x of the reference configuration by the *constitutive equation* of the material,

$$T^\varphi(x^\varphi) = \hat{T}^r(x, \nabla\varphi(x)).$$

As this equation is defined for all matrices $\nabla\varphi \in \mathbb{R}_{\text{sym},+}^{3 \times 3}$, materials subjected to internal constraints (materials that can only be deformed in a certain, restricted manner) are ruled out.

An equivalent definition of elastic materials is the statement, that there exist mappings

$$\hat{T} : \bar{\mathcal{D}} \times \mathbb{R}_{\text{sym},+}^{3 \times 3} \rightarrow \mathbb{R}_{\text{sym}}^{3 \times 3}, \quad \hat{T}(x, F) = (\det F) \hat{T}^r(x, F) F^{-T}$$

and

$$\hat{\Sigma} : \bar{\mathcal{D}} \times \mathbb{R}_{\text{sym},+}^{3 \times 3} \rightarrow \mathbb{R}_{\text{sym}}^{3 \times 3}, \quad \hat{\Sigma}(x) = (\det F) F^{-1} \hat{T}^r(x, F) F^{-T}$$

for all $x \in \bar{\mathcal{D}}, F \in \mathbb{R}_{\text{sym},+}^{3 \times 3}$, given as

$$T(x) = \hat{T}(x, \nabla\varphi(x)) \text{ and } \Sigma(x) = \hat{\Sigma}(x, \nabla\varphi(x))$$

for all $x \in \bar{\mathcal{D}}$.

An important property of elastic materials is, that its observable quantities are independent of the choice of the basis in which they are computed. This principle is formulated in the following axiom.

Axiom 2 (Axiom of material frame-indifference). *Let $\bar{\mathcal{D}}^\psi$ a rotated configuration of the deformed configuration $\bar{\mathcal{D}}^\varphi$, i. e. $\psi = Q\varphi$ for a rotation Q . Then*

$$t^\psi(x^\psi, Qn) = Qt^\varphi(x^\varphi, n)$$

for all $x \in \bar{\mathcal{D}}$ and all $n \in \{v \in \mathbb{R}^3 : \|v\| = 1\}$. t^ψ and t^φ denote the Cauchy stress vector fields in the respective deformed configurations.

One of the consequences of this axiom is that it reduces the number of mappings $(x, F) \mapsto \hat{T}^r(x, F)$ that can be used in the constitutive equations. This statement is stated in a more rigorous manner in the following theorem.

Theorem 4 (adapted from [Cia88, Theorem 3.3-1]). *The response function \hat{T}^r for the Cauchy stress satisfies the axiom of frame-indifference, if and only if one of the following equivalent statements hold:*

2. Background and fundamentals

- $\hat{T}^r(x, QF) = Q\hat{T}^r(x, F)Q^T$ for all $F \in \mathbb{R}_{sym,+}^{3 \times 3}$ and all rotations Q ,
- $\hat{T}^r(x, F) = R\hat{T}^r(x, U)R^T$ for all $F = RU \in \mathbb{R}_{sym,+}^{3 \times 3}$,
- There exists a mapping $\tilde{\Sigma}$ such that for the response function $\hat{\Sigma}$ to the second Piola-Kirchhoff tensor $\hat{\Sigma}(x, F) = \tilde{\Sigma}(x, F^T F)$ for all $x \in \bar{\mathcal{D}}$ and all $F \in \mathbb{R}_{sym,+}^{3 \times 3}$.

2.3.1. Isotropic materials

Theorem 4 shows how an axiom on the behavior of an elastic material can influence the structure of the Cauchy stress tensor. In this section, we will show that assumptions to the material itself can influence the tensor in a similar manner.

Definition 5. An elastic material is *isotropic* at point x if the response function to the Cauchy stress satisfies

$$\hat{T}^r(x, FQ) = \hat{T}^r(x, F)$$

for all $F \in \mathbb{R}_{sym,>}^{3 \times 3}$ and all rotations Q .

In other words: A material is isotropic at point x if the Cauchy stress tensor is not altered by rotations of the reference configuration around that point. If that statement is valid for all points, we will call the material isotropic, not specifying the point. If the statement is invalid, we will call the material *anisotropic*. The property of isotropy implies a property of the response function (which sometimes is also called isotropic):

Theorem 6 (adapted from [Cia88, Theorem 3.4-1]). *A material is isotropic at point x , if and only if there exists a mapping $\tilde{T}(x, F)$ that satisfies*

$$\hat{T}^r(x, F) = \tilde{T}(x, FF^T)$$

for all $F \in \mathbb{R}_{sym,+}^{3 \times 3}$.

Definition 7. A material is called *homogeneous*, if its response function is independent of the point considered. Materials, that are not homogeneous are called *nonhomogeneous* or *inhomogeneous*.

The Rivlin–Ericksen representation theorem

Considering an isotropic material together with the axiom of material frame-indifference, yields an important theorem on elastic material and a simple form of the response function.

Theorem 8 (Rivlin–Ericksen representation theorem, adapted from [Cia88, Theorem 3.6-1]). *A mapping $\hat{T} : \mathbb{R}_{sym,+}^{3 \times 3} \rightarrow \mathbb{R}_{sym}^{3 \times 3}$ satisfies the conditions for elastic materials with response functions that are frame-indifferent and isotropic at point $x \in \mathcal{D}$, i. e.*

$$\begin{aligned} \hat{T}(QF) &= Q\hat{T}(F)Q^T \text{ and} \\ \hat{T}(FQ) &= \hat{T}(F) \end{aligned}$$

for all $F \in \mathbb{R}_{sym,+}^{3 \times 3}$ and all rotations Q , if and only if

$$\hat{T}(F) = \tilde{T}(FF^T)$$

for all $F \in \mathbb{R}_{sym,+}^{3 \times 3}$, where $\tilde{T} : \mathbb{R}_{sym,>}^{3 \times 3} \rightarrow \mathbb{R}_{sym}^{3 \times 3}$ satisfies

$$\tilde{T}(B) = \beta_0(\iota_B)\text{id} + \beta_1(\iota_B)B + \beta_2(\iota_B)B^2$$

for all $B \in \mathbb{R}_{sym,>}^{3 \times 3}$ and β_0 , β_1 and β_2 are real-valued functions of the three principal invariants of B .

Remark 9. For a matrix $A \in \mathbb{R}^{3 \times 3}$, the principal invariants are $\iota_B = (\iota_1, \iota_2, \iota_3)$, with

$$\begin{aligned}\iota_1 &= \text{tr } A, \\ \iota_2 &= \text{tr Cof } A, \\ \iota_3 &= \lambda_1 \lambda_2 \lambda_3,\end{aligned}$$

where λ_1 , λ_2 , λ_3 are the eigenvalues of A .

As a consequence of this theorem, the response functions \hat{T}^r and $\hat{\Sigma}$ can also be expressed in terms of the principal invariants.

Theorem 10 (adapted from [Cia88, Theorem 3.6-2]). For an elastic material whose response function is frame-indifferent and isotropic at point $x \in \mathcal{D}$ and an arbitrary deformation $\varphi : \mathcal{D} \rightarrow \mathbb{R}^3$, the Cauchy stress tensor at point $x^\varphi = \varphi(x)$ is given by

$$T^\varphi(x^\varphi) = \hat{T}^r(x, \nabla\varphi(x)) = \bar{T}^r(x, \nabla\varphi(x)\nabla\varphi(x)^T),$$

where the response function $\bar{T}^r(x, \cdot) : \mathbb{R}_{sym,>}^{3 \times 3} \rightarrow \mathbb{R}_{sym}^{3 \times 3}$ is of the form

$$\bar{T}^r(x, B) = \beta_0(x, \iota_B)\text{id} + \beta_1(x, \iota_B)B + \beta_2(x, \iota_B)B^2$$

for all $B \in \mathbb{R}_{sym,>}^{3 \times 3}$. β_0 , β_1 , β_2 are real-valued functions of the principal invariants of B .

The second Piola-Kirchhoff stress-tensor at $x \in \mathcal{D}$ is given by

$$\Sigma(x) = \hat{\Sigma}(x, \nabla\varphi(x)) = \tilde{\Sigma}(x, \nabla\varphi(x)^T \nabla\varphi(x)),$$

where

$$\tilde{\Sigma} = \gamma_0(x, \iota_B)\text{id} + \gamma_1(x, \iota_B)B + \gamma_2(x, \iota_B)B^2$$

for all $B \in \mathbb{R}_{sym,>}^{3 \times 3}$. γ_0 , γ_1 , γ_2 are real-valued functions of the principal invariants of B .

Additionally, if either of the functions \bar{T}^r and $\tilde{\Sigma}$ is of the given forms, the material is isotropic at the given point x and the axiom of frame-indifference is satisfied.

2. Background and fundamentals

The Lamé–Navier tensor

If we assume, that the elastic material we consider is isotropic and homogeneous and that its reference configuration is a natural state, we can show that the response function only depends on two constants.

Theorem 11 (adapted from [Cia88, Theorem 3.8-1]). *Let the given elastic material be homogeneous and isotropic and let its reference configuration be a natural state. If the functions γ_i , for $i = 0, 1, 2$ from Theorem 10 are differentiable at $\iota = (3, 3, 1)$, there exist two constants λ and μ , such that the response function $\hat{\Sigma} : \mathbb{R}^{3 \times 3} \rightarrow \mathbb{R}_{sym}^{3 \times 3}$ has the form*

$$\hat{\Sigma}(F) = \tilde{\Sigma}(C) = \tilde{\Sigma}(E) = \lambda(\text{tr } E)\text{id} + 2\mu E + o(E), \quad (2.1)$$

where $C = F^T F = I + 2E$, $F \in \mathbb{R}^{3 \times 3}$. C denotes the right Cauchy–Green strain tensor that is associated with the quadratic form

$$(\epsilon, \epsilon) \in \mathbb{R}^3 \times \mathbb{R}^3 \rightarrow \epsilon^T C(x) \epsilon$$

and E the Green–St Venant strain tensor defined by

$$2E = C - \text{id}.$$

All materials considered in this thesis are defined using a (linearized) tensor of that type.

This Lamé–Navier type of material is especially suited for filling a structure in shape optimization, as in that case, isotropic materials are preferable (the structure is not modeled by the tensor). The actual tensor is not optimized in this thesis. For an example of material optimization by directly modifying tensor entries — so-called *free material optimization* — s. [HKLS10].

To introduce the equation of *linear* elasticity, we again consider the boundary value

$$\begin{aligned} -\text{div}(\text{id} + \nabla u)\tilde{\Sigma}(E(u)) &= f \text{ in } \mathcal{D}, \\ u &= 0 \text{ on } \Gamma_D, \\ (\text{id} + \nabla u)\tilde{\Sigma}(E(u))n &= g \text{ on } \Gamma_N. \end{aligned}$$

Recall, that the response function $\tilde{\Sigma}$ for a material described by a Lamé–Navier tensor satisfies

$$\tilde{\Sigma}(E) = \lambda(\text{tr } E)\text{id} + 2\nu E + o(\|E\|) \quad (2.2)$$

and that the Green–St Venant strain tensor is given by

$$E(u) = \frac{1}{2}(\nabla u^T + \nabla u + \nabla u^T \nabla u). \quad (2.3)$$

Linearizing equations (2.2) and (2.3) yields a *linearized* or *linear elastic tensor*

$$C = \lambda(\text{tr } E)\text{id} + 2\nu E \quad (2.4)$$

also called *Lamé–Navier* tensor. The tensor

$$\epsilon[u] = \frac{1}{2}(\nabla u^T + \nabla u).$$

is called the *linearized strain tensor*. With these linearizations, we can formulate the boundary value problem of *linear elasticity*.

$$\begin{aligned} -\operatorname{div}(\lambda(\operatorname{tr} \epsilon[u])\operatorname{id} + 2\mu\epsilon[u]) &= f \text{ in } \mathcal{D}, \\ u &= 0 \text{ on } \Gamma_D, \\ (\lambda(\operatorname{tr} \epsilon[u])\operatorname{id} + 2\mu\epsilon[u]) &= g \text{ on } \Gamma_N, \end{aligned} \tag{2.5}$$

We notice the equivalence between solving the boundary value problem and a weak form of a partial differential equation.

Theorem 12. *The task of finding a solution u for the linear boundary value problem (2.5) is equivalent to finding a solution to*

$$A(u, \theta) = \ell(\theta) \text{ for all } \theta \in W_0^{1,2}(\mathcal{D}), \tag{2.6}$$

where

$$\begin{aligned} A(u, \theta) &= \int_{\mathcal{D}} \lambda \operatorname{tr} \epsilon[u] \operatorname{tr} \epsilon[\theta] + 2\mu \epsilon[u] : \epsilon[\theta] \, dx, \\ \ell(\theta) &= \int_{\mathcal{D}} f \cdot \theta \, dx + \int_{\Gamma_N} g \cdot \theta \, da. \end{aligned}$$

$W_0^{1,2}(\mathcal{D})$ is defined as the space of functions in $W^{1,2}(\mathcal{D})$ that vanish on Γ_D in the sense of traces.

Proof. Cf. [Cia88, Theorem 6.3-1] □

Existence of solutions of problem (2.6) can be shown, but will not be treated here (s. [Cia88, Chapter 6] for details), as we will not use this specific energy alone for any of the models below.

Problem (2.6) can again be rewritten into an energy minimization problem: Solving (2.6) is equivalent to minimizing

$$\mathcal{E}[u] = \frac{1}{2}A(u, u) - \ell(u)$$

for functions u that vanish on Γ_D . This is the formulation that will be used for the problems treated in this thesis.

Up to here, all elastic objects considered have been 3-dimensional, as the theory tries to model real-world objects. Throughout this thesis though, we will only consider 2-dimensional elastic bodies. The whole theory presented above remains true, with minor changes (the tensor has only the entries related to the first two dimensions etc.), mainly reducing the number of degrees of freedom in the optimization problem. Starting from the next section, we will always assume the spatial dimension to be $d = 2$.

2.4. Introduction to shape optimization

In this section, we will formulate a basic rating of shapes. Let $\mathcal{J}[v, u[v]]$ be a functional depending on a *design parameter* v (which describes the shape) and a displacement $u[v]$. The design variable will be of phase field type and thus a continuous function $\mathcal{D} \rightarrow \mathbb{R}$. More details will be given below. As suggested by the notation, u depends on v , specifically by a *state equation*, which is the equation of linear elasticity (discussed in Section 2.2) in this case. In this setup, shape optimization can be formulated as a minimization of a target functional $\mathcal{J}[v, u[v]]$ under the constraint that u solves the equation of linear elasticity for the given design parameter v .

From the mathematical point of view, two fundamental questions have to be considered: Is the optimization problem well-posed, i. e. is there a (possibly unique) solution and what are the optimality conditions for these solutions? For insights on these questions, we refer to [All02, Chapter 3].

We formulate the optimization problem as

$$\begin{aligned} \min_v J[v, u[v]], \\ \text{s. t. } u[v] = \arg \min_{\tilde{u}} \mathcal{E}[v, \tilde{u}], \end{aligned}$$

where $\mathcal{E}[v, \tilde{u}]$ is the linear elastic energy. This energy and the target functional $\mathcal{J}[v, u[v]]$ will be defined below. We have to make sure that the deformation, as well as the volume of the shape described by v , are measured by $\mathcal{J}[v, u[v]]$, as not doing so will result in trivial solutions. It is alternatively possible to prescribe a given volume for the set of acceptable shape instead of assigning a “cost” to it. Note, that this decision influences the set of *admissible shapes*, the shapes that are considered in the minimization of $\mathcal{J}[v, u[v]]$.

Furthermore, we have to introduce a term measuring the interface length of the considered shapes. Without such a term, in many configurations arbitrarily fine structures are preferred, making the optimal shape undefined and the optimization problem ill-posed. The interface-measuring term acts as a regularizer and is usually weighted by a small constant.

Using all three of the described terms, shape optimization becomes well-defined and has been treated in [PRW12] for a hyperelastic and linear elastic, one-scale setting. In [All02], shape optimization using a homogenization method is described, which treats the issue of arbitrarily fine microstructures by upscaling the microstructures into a homogenized tensor.

The exact definitions of $\mathcal{J}[v, u[v]]$ and $\mathcal{E}[v, u]$ will vary throughout this thesis, depending on the problems considered in the respective chapters. Still, in all cases, \mathcal{J} will have the structure

$$\mathcal{J}[v, u[v]] = \mathcal{W}[v, u] + \nu \mathcal{V}^\varepsilon[v] + \beta \mathcal{L}^\varepsilon[v],$$

for constants $\nu, \beta > 0$. The *compliance* $\mathcal{W}[v, u]$ measures the deformations, $\mathcal{V}^\varepsilon[v]$ measures the volume of the shape described by the design parameter v and the interface term $\mathcal{L}^\varepsilon[v]$

measures the length of the perimeter of the shapes in $\mathring{\mathcal{D}}$. The values of these constants will determine, how much material is introduced into the considered shapes and how much microstructure is feasible.

The definition of $\mathcal{E}[v, u]$ will depend on the setup considered in the respective optimization problem: There may be a deterministic or stochastic load scenario (where the latter consists of several loads that occur with certain probabilities) and different boundary conditions.

All functionals will be described in detail in the respective chapters.

2.5. Phase fields

In all three models discussed in this thesis, the shape in question is described by a phase field as a design parameter. In general, a phase field is defined as a continuous function $v \in L^2(\mathcal{D}, \mathbb{R})$, of which two values $a \in \mathbb{R}$ and $b \in \mathbb{R}$ are identified as *phases*. The most common choices are $a = -1, b = 1$ and $a = 0, b = 1$. In any case, a and b represent different materials, e. g. a soft and hard material, void and material or a general domain decomposition as it is used in segmentation problems.

To examine the basic properties of phase field representations, let $\mathcal{O} \subset \mathcal{D}$ be the subdomain represented by the phase b of a phase field. For now, assume that $a = -1, b = 1$ or $a = 0, b = 1$. Other ranges can be handled by methods similar to the ones described in the following sections.

2.5.1. Volume measurements

To measure the volume of \mathcal{O} , we first introduce the *characteristic function* of v . It is defined by

$$\chi(v) = \frac{1}{4}(v+1)^2 \text{ for } a = -1, b = 1 \text{ and } \chi(v) = v \text{ for } a = 0, b = 1.$$

As $\mathcal{O} = \{x \in \mathcal{D} : \chi(v(x)) = 1\}$, the volume is given by

$$\mathcal{V}^\varepsilon(\mathcal{O}) = \int_{\mathcal{D}} \chi(v(x)) \, dx,$$

which can be calculated for any given phase field. Note, that the volume behaves as expected for *pure phases*, i. e. $v = a$ or $v = b$, but admits intermediate values for values of $a < v < b$. Note that in the case of $a = -1, b = 1$ a “mixture” of 50% hard and 50% soft material would not have volume $\frac{1}{2}$ with this definition of χ .

Nevertheless, we use this definition of $\chi(v)$ in two of the three models discussed in this thesis, as it is smooth on \mathbb{R} . The values of v that are important are the pure phases and errors on (the relatively small) *transitional* regions are acceptable. The width of this region is controlled by a parameter $\varepsilon > 0$, which role will be treated in more detail in the following section.

2. Background and fundamentals

2.5.2. Interface length

As v is continuous, there is no sharp interface, but an interface region of width ε , making it meaningless to define a length for any $\varepsilon > 0$. Still, the transitional region in between \mathcal{D} and $\mathcal{D} \setminus \mathcal{O}$ can be interpreted as an approximation of the circumference of \mathcal{O} .

A more meaningful measure can be defined based on work by Modica and Mortola [MM77]. First, let

$$\psi(v) := \frac{9}{16} (v^2 - 1)^2 \quad \text{or} \quad \psi(v) = \begin{cases} \frac{32}{\pi^2} (1 - v)v & v \in [0, 1] \\ \infty & \text{else} \end{cases}$$

be a *double-well potential* for the cases $a = -1, b = 1$ and $a = 0, b = 1$, respectively. $\psi(v)$ has two minima at $v = a$ and $v = b$ and will be used to push the phase field towards the two phases. Let $\varepsilon > 0$ and define the approximated interface length

$$\mathcal{L}^\varepsilon[v] := \frac{1}{2} \int_{\mathcal{D}} \varepsilon |\nabla v|^2 + \frac{1}{\varepsilon} \psi(v) \, dx. \quad (2.7)$$

$\mathcal{L}^\varepsilon[v]$ consists of two weighted terms: the double-well potential and a measure of the areas, where $|\nabla v| \neq 0$. Letting $\varepsilon \rightarrow 0$ pushes v towards the pure phases, while an $\varepsilon > 0$ determines the width of the interface region where $v \notin \{a, b\}$. More precisely, for $\varepsilon \rightarrow 0$, $\mathcal{L}^\varepsilon[v]$ Γ -converges to the length of the interface.

To understand this type of convergence, first consider the definition:

Definition 13. Similar to [Bra06, Theorem 2.1], let X be a topological space and $F_\varepsilon, F : X \rightarrow [-\infty, \infty]$. Then F_ε Γ -converges to F_0 iff the following conditions hold

1. *lim inf inequality:* For every $x \in X_0$ and for every sequence $x_\varepsilon \rightarrow x$

$$F_0(x) \leq \liminf_{\varepsilon \rightarrow 0} F_\varepsilon(x_\varepsilon) \quad (2.8)$$

holds.

2. *Recovery sequence/lim sup-inequality:* For every $x \in X_0$ exists a sequence $x_\varepsilon \rightarrow x$ which fulfills

$$F_0(x) \geq \limsup_{\varepsilon \rightarrow 0} F_\varepsilon(x_\varepsilon). \quad (2.9)$$

To explore an important property of Γ -convergence, consider minimizers of F_ε and F_0 : Let $m_\varepsilon := \min_{x_\varepsilon \in X_\varepsilon} F_\varepsilon(x_\varepsilon)$ and $m_0 := \min_{x_0 \in X_0} F_0(x_0)$ and the following definition.

Definition 14. F_ε is *equi-coercive* if there exists a lower semicontinuous coercive function Ψ , s. t. $F_\varepsilon \geq \Psi$ for all ε . Cf. [DM93, Definition 7.6 and Proposition 7.7] for a more detailed introduction.

Corollary 15 (Adapted from [Bra06, Chapter 1]). *Let X be a topological space. If F_ε is equi-coercive and F_ε Γ -converges to F_0 , then minimizers m_ε of F_ε converge to the minimizers m_0 of F_0 and every cluster point of minimizing sequences is a minimum of F_0 .*

Proof. For equi-coercive families, equation (2.8) implies

$$\inf F_0 \leq F_0(x_0) \leq \liminf_{\varepsilon \rightarrow 0} F_\varepsilon(x_\varepsilon) = \liminf_{\varepsilon \rightarrow 0} \inf F_\varepsilon.$$

Additionally, equation (2.9) leads to

$$\inf F_0 \geq \limsup_{\varepsilon \rightarrow 0} \inf F_\varepsilon.$$

□

When modeling shape optimization problems with phase field approaches, interfaces between different material domains are smeared out: Instead of a sharp interface, an interface region of width $\varepsilon > 0$ is introduced. Thus, a notion of convergence for $\varepsilon \rightarrow 0$, is desirable, as it provides a sense of convergence towards a limit problem. With those definitions, we can now prove that the interface measure $\mathcal{L}^\varepsilon[v]$ approximates the interface of the described shape.

Theorem 16 (Adapted from [Bra06, Theorem 7.3]). *For*

$$\psi = \frac{9}{16} (v^2(x, y) - 1)^2 \text{ for } a = -1, b = 1 \text{ or } \psi = \frac{32}{\pi} (1 - v)v \text{ for } a = 0, b = 1$$

the functional (2.7) Γ -converges to

$$\mathcal{L}^0[v] = \begin{cases} \mathcal{H}^{n-1}(\partial\{v = 1\} \cap \mathcal{D}) & \text{if } v \in [a, b] \text{ almost everywhere,} \\ \infty & \text{else.} \end{cases}$$

with respect to the L^1 -topology.

Proof. The proof will only be given in one dimension to illustrate the concepts and will follow along the lines of [Bra06, Theorem 7.3]. For a proof of the theorem in higher dimensions, refer to that source.

Suppose, that $\mathcal{L}^\varepsilon[v_\varepsilon] < \infty$, let $\zeta > 0$ and an interval I such, that v_ε is equal to ζ and $1 - \zeta$ at the endpoints of that interval. Then - using the algebraic inequality $a^2 = b^2 \geq 2ab$ and a change of variables $s = v_\varepsilon(t)$ - the *Modica-Mortola trick* (cf. [Bra06]) implies

$$\int_I \left(\frac{1}{\varepsilon} \psi(v_\varepsilon) + \varepsilon |v'_\varepsilon|^2 \right) dt \geq 2 \int_I \sqrt{\psi(v_\varepsilon)} |v'_\varepsilon| dt \geq 2 \int_\zeta^{1-\zeta} \sqrt{\psi(s)} ds =: C_\zeta. \quad (2.10)$$

This implies, that the number of transitions between ζ and $1 - \zeta$ is bounded by a constant A for all ε .

2. Background and fundamentals

Since $\int_{\mathcal{D}} \psi(v_\varepsilon) dt \leq \varepsilon C$ the statement

$$\lim_{\varepsilon \rightarrow 0} \mathcal{H}(\{x \in \mathbb{R} : \min_{y \in \{0,1\}} |v_\varepsilon(x) - y| \geq \delta\}) = 0$$

holds for all $\delta > 0$. This is called the convergence $v_\varepsilon \rightarrow \{0, 1\}$ *in measure*. Additionally $v_\varepsilon \rightarrow v$ with v piecewise constant taking values a and b only. Denote the discontinuity points of v by $S(v)$. Then

$$\liminf_{\varepsilon} \mathcal{L}^\varepsilon(v_\varepsilon) \geq C_\zeta \#(S(v))$$

and the lower bound is achieved because ζ can be chosen freely.

For the limsup inequality take w as the solution of

$$w'(s) = \sqrt{\psi(w)} \quad w(0) = \frac{a+b}{2}.$$

(suppose a global solution exists for simplicity) and define $w_\varepsilon = w(\frac{t}{\varepsilon})$. w is strictly increasing and $a < w(t) < b$ for all t . Furthermore $\lim_{t \rightarrow -\infty} w(t) = a$ and $\lim_{t \rightarrow \infty} w(t) = b$, which implies that

$$w_\varepsilon(t) \rightarrow \bar{w} = \begin{cases} a & t < 0 \\ b & t \geq 0. \end{cases} \quad (2.11)$$

Every w_ε optimizes (2.10) in the sense that

$$\frac{1}{\varepsilon} \psi(w_\varepsilon) + \varepsilon |w'_\varepsilon|^2 = 2\sqrt{\psi(w_\varepsilon)} |w'_\varepsilon|$$

and as such provides a recovery sequence for $v = \bar{w}$ as given in (2.11). For more general v with $v(t) \in \{0, 1\}$ we can construct a recovery sequence by gluing $w_\varepsilon((\bar{t} \pm t)/\varepsilon)$ for $\bar{t} \in S(v)$. \square

Remark 17. [Bra06, Theorem 7.3] gives an more general result: For general $a, b \in \mathbb{R}$ and $\psi \geq 0$ with $\psi(v) = 0$ only if $v = a$ or $v = b$ and $\psi(v) \geq c(|v|^2 - 1)$, the functional converges to a multiple of the perimeter.

Thus, \mathcal{L}^ε is a suitable measure of the interface length, for the two functions $\psi(v)$ introduced in Theorem 16, or if the appropriate constant is used. Additionally, the interface width is determined by the parameter ε and can thus be controlled.

2.5.3. Applications to shape optimization

To model a shape optimization problem, two kinds of materials are associated with the two phases: A hard material is used wherever $v = b$ and a softer material is used wherever $v = a$. We define the *elastic energy* stored in a material under a given deformation $u : \mathcal{D} \mapsto \mathbb{R}^n$ as

$$\mathcal{W}^\delta := \int_{\mathcal{D}} ((1 - \delta)\chi(v) + \delta) C_{LN} \epsilon[u] : \epsilon[u] dx. \quad (2.12)$$

In formula (2.12), $\delta > 0$ is the ratio between hard and soft material, $\epsilon[u] = \frac{Du^T + Du}{2}$ is the strain tensor or *symmetrized gradient* and C_{LN} is a Lamé–Navier type tensor.

Let $\ell[u] := \int_{\Gamma_N} g \cdot u \, da$ and define the *equilibrium displacement* $u \in W^{1,2}(\mathcal{D}, \mathbb{R}^d)$ as the minimizer of the elastic *free energy*

$$\mathcal{E}[v, u] = \mathcal{W}^\delta[u] - \ell[u].$$

For shape optimization, a target functional, i.e. the functional by which admissible shapes are rated, has to be defined. For the computations described here, a *compliance* type functional is used: Let $\nu, \beta \in \mathbb{R}^+$ and

$$\mathcal{J}[v, u] = 2\mathcal{W}^\delta[v, u] + \nu\mathcal{V}^\epsilon[v] + \beta\mathcal{L}^\epsilon[v]. \quad (2.13)$$

Optimizing (2.13) over v and u does not give useful results in the shape optimization context. Instead, minimizing $\mathcal{J}[v] = \mathcal{J}[v, u[v]]$ where $u[v] = \arg \min_u \mathcal{E}[v, u]$ over v only considers the equilibrium displacements for each shape under given loads (which will be defined by boundary conditions).

Lemma 18. *Let $v \in W^{1,2}(\mathcal{D})$ with $a \leq v \leq b$ and $\arg \min_u \mathcal{E}[v, u[v]] \in W^{1,2}$, then*

$$\Gamma\text{-}\lim_{\epsilon \rightarrow 0} \mathcal{J}[v_\epsilon, u] = \mathcal{J}[v, u]$$

with respect to the $L^1(\mathcal{D})$ -topology.

For a proof of this lemma cf. [PRW12] (using some arguments of [Bra02]).

Be reminded, that not all double-well potentials $\psi(v)$ ensure that $a \leq v \leq b$: The potential

$$\psi(v) = \begin{cases} \frac{32}{\pi^2}(1-v)v & v \in [0, 1] \\ \infty & \text{else} \end{cases}$$

does ensure v is within the bounds, as the energy is ∞ else, while the potential $\psi(v) := \frac{9}{16}(v^2 - 1)^2$ allows $v \notin [-1, 1]$. In numerical applications, this fact is not relevant as long as the outliers only form a low dimensional (0-dimensional) subset, which is true in most applications.

3. Stochastic dominance constraints in shape optimization

In this chapter, we will pick up concepts of risk aversion from finite dimensional stochastic optimization. There are two lines of research that have been pursued in this context: Risk aversion in the objective functional and risk aversion using constraints. Risk aversion via risk measures (statistical parameters) was described in [PR07], practically meaningful risk measures have been identified enabling multi-period decision making. In this context, there have been mean-risk models in a two-stage linear setting [Ahm06, Kri05], a two-stage mixed-integer linear setting [ST06, RV08] and in a multistage setting [AR15, Sha12].

The other line of research focuses on risk aversion using constraints and concepts of stochastic dominance. Instead of risk minimization, this approach bounds the risk using partial orders on random variables, defining acceptable sets by comparison with a benchmark. Orders on families of random variables have been considered in [MS02]. The incorporation of dominance constraints into stochastic programs was done by Dentcheva and Ruszczyński [DHR07, DR03, DR04, DR08] in several settings, concerning finite and infinite Banach spaces for the decision variables.

Stochastic dominance in optimization under uncertainty has been considered on the topics of basic analysis of models [DR03, DHR07, Lue08, GNS08, GGS11, DR13, DR14], algorithm development [RR08, DR10, DS10], and industrial applications e.g. [CGS09, FMRZ11, DGG⁺11].

In the context of shape optimization, uncertainty has attracted considerable attention. Multi-load approaches take into account a fixed (usually small) number of load configurations, cf. [AJ05, GRB03]. There are applications of robust worst-case shape optimization in [BTN02]. In the context of beam models [Mel01] and aerodynamic design [SS15, SS09] there have been discussions of shape optimization with stochastic loading. In [CHP⁺09] an efficient optimization approach of the expected value of compliance and tracking type cost functionals under stochastic loads has been developed. This approach makes use of representations of cost and stochastic loads as linear combinations of basic modes and has also been used for the optimization of risk-averse cost measures [CHP⁺11].

Allaire and Dapogny used adapted duality techniques to derive an efficient algorithm for a linearization of the cost functional in a worst case optimization scenario [AD14] and investigated different types of uncertainties in [AD15]. In the latter, they investigate minimized stochastic cost functionals and risk measures, such as the expected cost of the failure probabilities. Their approach is based on the Taylor expansion of the risk measure and implies a deterministic algorithm with a cost depending on the number of realizations

of the random configuration.

Dambrine, Dapogny and Harbrecht researched elastic shape optimization with stochastic surface loads and developed a deterministic algorithm that minimized the expected cost [DDH15]. This algorithm relies on the fact, that the objective functional and its gradient are determined by the first-order moments of the surface load and on an efficient optimization of the integrals in question in six dimensions.

Furthermore, Pach described the concept of stochastic dominance in the context of parametric shape optimization in [Pac14].

The model and results described in this chapter have been published in [CRST17]. To the best knowledge of the authors of that publication, there is no further work on numerical techniques for risk-averse shape optimization handling general, nonanticipative domains as variables.

In this context, a benchmark is introduced that defines the set of admissible shapes as the shapes that are smaller than the benchmark in a certain order, where there are multiple options to chose that order. In this thesis, the stochastic orders are defined by considering a given set of scenarios defined by certain probabilities and loads. Contrary to the models of shape optimization, that enforce risk aversion through the objective functional and find a shape minimizing that objective functional, this approach allows us to compare shapes and find the most suitable one out of the set of admissible shapes.

In this chapter, we will first define the basic concepts of stochastic orders and stochastic dominance. Then, we will define stochastic energies that can be used as constraints for an optimization problem. Here, several scenarios are introduced as realizations of a stochastic variable. The stochastic functionals will be rewritten so that they can be evaluated using only finitely many evaluations of the underlying elastic energies. Finally, some modifications have to be made to allow a numerical evaluation of all terms appearing in any of the functionals.

3.1. Basic concepts of stochastic dominance

This section gives a short introduction to stochastic orderings and stochastic dominance. The motivation for this field arises from the need to classify general stochastic quantities, e. g. bets, investments or risks of failure. Pointwise or *statewise* comparison of stochastic quantities is — in general — not of interest and comparing basic properties like the mean does not yield sufficient insight into which scenarios might fail and whether those scenarios are of high or low risk. Thus, more meaningful *stochastic orders* are needed, some of which will be introduced below. For a deeper insight, we refer to [BMRM16] and [MS02].

First, let us define some basic concepts of probability theory. For these definitions, we follow along the lines of [BMRM16].

Definition 19. Let X be a real-valued stochastic variable. Define the *cumulative distribution function* by

$$F_X(t) := \mathbb{P}_X((-\infty, t])$$

3. Stochastic dominance constraints in shape optimization

and the *survival function* by

$$\bar{F}_X(t) := 1 - F_X(t).$$

Furthermore, the *integrated survival function* is given as

$$\Pi_X(t) := \int_t^\infty \bar{F}(z) \, dz.$$

For some representations, we will also need the *quantile function*

$$q_X(t) := \inf\{x \mid F(x) \geq t\}.$$

All functions defined in Definition 19 can be used to classify random variables. This idea will be used in the next section to create orderings that sort random variables by “risk”, in an appropriate sense.

3.1.1. Stochastic orderings

An order on random variables is denoted as a stochastic order. These orders compare random variables in different ways to enable more useful measures than e. g. comparing the mean.

In the following, we define two well known stochastic orders and discuss some of their properties. The first order we will consider is the “usual stochastic order”, which compares the survival function (and thus the cumulative distribution function) of two random variables.

Definition 20. Let X and Y be random variables. Then the *usual stochastic order* \preceq_{st} is defined as

$$X \preceq_{\text{st}} Y \quad \Leftrightarrow \quad \bar{F}_X(t) \leq \bar{F}_Y(t) \text{ for all } t.$$

Additionally, the notation $X =_{\text{st}} Y$ iff $X \preceq_{\text{st}} Y$ and $Y \preceq_{\text{st}} X$ is used occasionally.

To rephrase, for every value t , the order \preceq_{st} compares the probability of stochastic variables exceeding that given value t . The usual stochastic order can also be defined using quantile functions, which will be useful to prove other equivalent formulations further below.

Lemma 21. *Let X and Y be random variables.*

$$X \preceq_{\text{st}} Y \quad \Leftrightarrow \quad q_X(t) \leq q_Y(t)$$

for all $t \in (0, 1)$.

Proof. This proof has been adapted from [BMRM16, Theorem 2.2.3].

Let $t \in (0, 1)$ and $X \preceq_{\text{st}} Y$. Then

$$[q_X(t), \infty) = \inf\{x : F_X(x) \geq t\} \supseteq \inf\{x : F_Y(x) \geq t\} = [q_Y(t), \infty)$$

3.1. Basic concepts of stochastic dominance

and thus $q_X(p) \leq q_Y(p)$.

Now let $q_X(t) \leq q_Y(t)$ for all $t \in (0, 1)$ and let U be uniformly distributed on $(0, 1)$. Then $\{q_X(U(\omega)) \leq t\} \supseteq \{q_Y(U(\omega)) \leq t\}$ for all $t \in \mathbb{R}$ and

$$F_X(t) = \mathbb{P}[q_X(U) \leq t] \geq \mathbb{P}[q_Y(U) \leq t] = F_Y(x)$$

for all $t \in \mathbb{R}$. Thus $X \preceq_{st} Y$. □

Another common way of defining stochastic orders is by verifying $\mathbb{E}[f(X)] \leq \mathbb{E}[f(Y)]$ for a suitable class of functions f , where the expected values exist. Which class is chosen determines the stochastic order defined and allows for an easy insight into the relationships between those orders. For the usual stochastic order, the definition using expected values is achieved using increasing functions.

Lemma 22. *Let X and Y be random variables. Then the following statements are equivalent:*

1. $X \preceq_{st} Y$,
2. There exist two random variables \hat{X} and \hat{Y} on the same probability space with $\hat{X} =_{st} X$ and $\hat{Y} =_{st} Y$ and $\mathbb{P}[\hat{X} \leq \hat{Y}] = 1$,
3. $f(X) \preceq_{st} f(Y)$ for all increasing functions f .
4. $\mathbb{E}[f(X)] \leq \mathbb{E}[f(Y)]$ for all increasing functions f .

Proof. This proof has been adapted from [BMRM16, Theorem 2.2.5].

We prove:

1 \Leftrightarrow 2 Let U be a uniformly distributed random variable on $(0, 1)$. Then $F_X^{-1}(U) =_{st} X$ and $F_Y^{-1}(U) =_{st} Y$ and by Lemma 21 we can conclude that $\mathbb{P}[F_X^{-1}(U) \leq F_Y^{-1}(U)] = 1$.

To prove the inverse statement, suppose that \hat{X} and \hat{Y} are two random variables on the same probability space and $\mathbb{P}[\hat{X} \leq \hat{Y}] = 1$. From the definition of the cumulative distribution function, for every $t \in \mathbb{R}$ the relation

$$\{\omega \in \Omega | \hat{X}(\omega) > t\} \subseteq \{\omega \in \Omega | \hat{Y}(\omega) > t\}$$

holds. Thus, $F_X(t) \geq F_Y(t)$ for all t .

1 \Leftrightarrow 3 Consider \hat{X} and \hat{Y} as above. Then $\mathbb{P}[f(\hat{X}) \leq f(\hat{Y})] = 1$ and thus $f(X) \preceq_{st} f(Y)$.

Statement 1 immediately from statement 3 with $f(x) = x$.

3. Stochastic dominance constraints in shape optimization

1 \Leftrightarrow 4 As above, $\mathbb{E}[X] = \mathbb{E}[\hat{X}] \leq \mathbb{E}[\hat{Y}] = \mathbb{E}[Y]$ and with statement 2 $\mathbb{E}[f(X)] \leq \mathbb{E}[f(Y)]$ for all increasing functions f for which both values exist.

Finally, observe that the indicator function $\chi_{(x,\infty)}$ is increasing. Thus $F_X(x) = \mathbb{E}[\chi_{(x,\infty)}(X)] \leq \mathbb{E}[\chi_{(x,\infty)}(Y)] = F_Y(x)$.

□

The class of functions considered in condition 4 characterizes the stochastic order and is a common way to define it. Considering a second important example of stochastic orders will clarify, why this formulation is convenient:

Definition 23. The *increasing convex order* is defined by

$$X \preceq_{\text{icx}} Y \quad \Leftrightarrow \quad \Pi_X[t] \leq \Pi_Y[t] \text{ for all } t \in \mathbb{R}.$$

Π denotes the integrated survival function, as given in Definition 19. Again, the notation $X =_{\text{icx}} Y$ iff $X \preceq_{\text{icx}} Y$ and $Y \preceq_{\text{icx}} X$ is defined.

This order — like the usual stochastic order — can be defined by several equivalent statements, which reveal different properties of \preceq_{icx} .

Lemma 24. *The following properties are equivalent*

1. $X \preceq_{\text{icx}} Y$,
2. $\mathbb{E}[(X - t)_+] \leq \mathbb{E}[(Y - t)_+]$ for all $t \in \mathbb{R}$,
3. $\mathbb{E}[f(X)] \leq \mathbb{E}[f(Y)]$ for all increasing convex functions f .

Proof. This proof has been adapted from [BMRM16, Theorem 2.3.2].

We prove the following equivalences:

2 \Leftrightarrow 3 $(X - t)_+$ is increasing and convex for all $t \in \mathbb{R}$ and every increasing convex function f can be written as the limit of positive linear combinations of functions $f_a(x) = (x - a)_+$.

1 \Leftrightarrow 2 The equation $\mathbb{E}[X] = \int_0^\infty \bar{F}_X(x) dx$ holds for any X non-negative with finite mean. Accordingly, $\mathbb{E}[(X - t)_+] = \int_t^\infty \bar{F}_X(x) dx = \Pi_X(t)$ for any such X . We conclude, that $\Pi_X[t] \leq \Pi_Y[t] \Leftrightarrow \mathbb{E}[(X - t)_+] \leq \mathbb{E}[(Y - t)_+]$.

□

Condition 3 illustrates the importance of defining stochastic orders using the expected value and a given class of functions, as it makes \preceq_{st} and \preceq_{icx} easily comparable. We can immediately deduce as a consequence of Lemma 24 and Lemma 22, that $X \preceq_{\text{st}} Y$ implies $X \preceq_{\text{icx}} Y$ and that the opposite implication does not hold.

3.1.2. Stochastic dominance

The definition of stochastic dominance arises out of the desire to avoid risks: In our context, lower values corresponding to lower risk of failure are preferred. Thus, X being stochastically dominant to Y implies that X has a lower risk of failure than Y (contrary to the notion used in financial models, where high values are often preferred). All methods described in this chapter can be applied in such a context, too, in almost all cases by small and straightforward changes to the inequalities.

This *risk aversion* can be defined in various ways, one of which is first and second order stochastic dominance.

Definition 25. Let X and Y be random variables.

1. X first-order dominates Y if and only if

$$\bar{F}_X(t) \leq \bar{F}_Y(t) \text{ for all } t.$$

2. X second-order dominates Y if and only if

$$\Pi_x(t) \leq \Pi_Y(t) \text{ for all } t.$$

3. Consistent with the definitions above, zeroth-order stochastic dominance can be defined as a statewise comparison.

We say “ X is n -th-order dominant over Y ” if X n -th-order dominates Y . Note, that first-order dominance can be equivalently defined by $X \preceq_1 Y \Leftrightarrow F_x(t) \geq F_Y(t)$ for all t . In the following, we will denote first-order dominance as \preceq_1 and second-order dominance as \preceq_2 . These will be the only orders of stochastic dominance that will be explored in more detail here. Lemmas 22 and 24 imply that $\preceq_1 = \preceq_{st}$ and $\preceq_2 = \preceq_{icx}$, which in turn implies that $X \preceq_1 Y \Rightarrow X \preceq_2 Y$. In more general terms every order of stochastic dominance (higher orders of stochastic dominance can be defined iteratively) defines a stochastic order and, as a consequence of definition 25, $X \preceq_k Y \Rightarrow X \preceq_l Y$ if and only if $k \leq l$. The opposite implication does not hold.

Example

To get a better understanding of what stochastic dominance means, we will consider an example: Suppose, there were three lotteries that would determine the price of a new car by a fair die roll ($\mathbb{P}[1] = \mathbb{P}[2] = \dots = \mathbb{P}[6] = \frac{1}{6}$). Based on the outcome between 1 and 6, the lotteries would require the player to pay a certain price. Table 3.1 lists the prices for each possible result.

Lottery A would let the player win the car for free if the result of the die roll was 1, for 1000\$ if it was a two etc. We can easily see, that lottery B does not give a better result than lottery A for each state (for the result 2, lottery B is worse). Still, lottery B is

3. Stochastic dominance constraints in shape optimization

	1	2	3	4	5	6
A	0	1000	1000	10000	20000	20000
B	0	5000	1000	0	20000	20000
C	0	1000	2000	10000	18000	20000

Table 3.1.: Prices for the three lotteries depending on the outcome of the die roll.

clearly better for any player, who prefers lower risk, as $\mathbb{P}[B \leq 5000] > \mathbb{P}[A \leq 5000]$. This fact is represented in the cumulative distribution functions of A and B (s. Figure 3.1) and results in $A \preceq_1 B$. In this sense, first-order dominance guarantees that lottery B is not more risky for the player than lottery A (and less risky, if $A \neq_1 B$ as it is for the A and B described here).

Now consider lottery C. As $F_C(1000) < F_A(1000)$, C does not first-order dominate A, but it does require the player to pay a lower price than lottery A when the die rolls a 5. In this sense, lottery C is suitable for players, who accept higher risks for some values, as long as they are compensated in the higher price regions. This trade-off is what second-order stochastic dominance guarantees. For the given variables, we can compute $\Pi_C(t) < \Pi_A(t)$ for all $t \in \mathbb{R}$ directly from Table 3.1 and thus conclude, that indeed $C \preceq_2 A$.

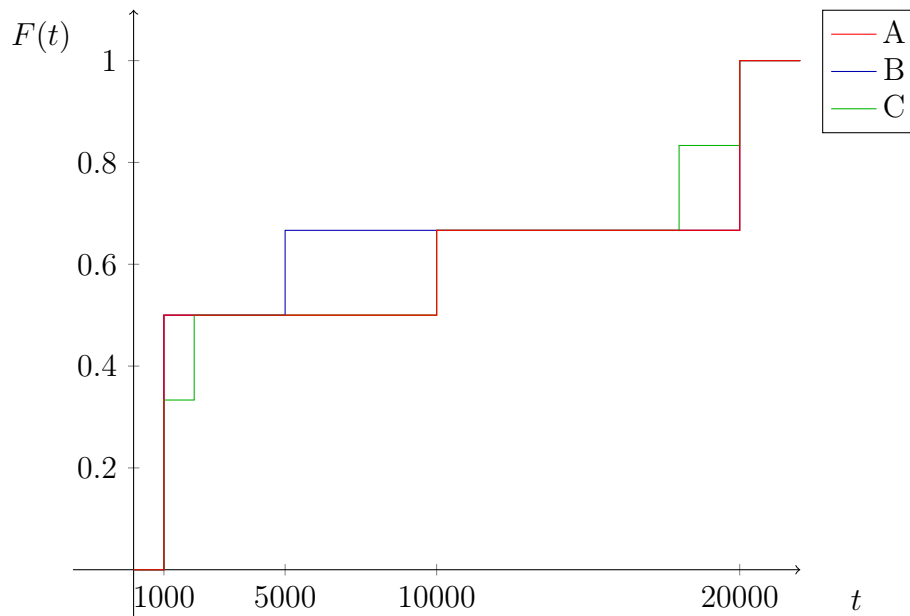


Figure 3.1.: Cumulative distribution functions of random variables A, B and C.

3.2. Application to discrete stochastic variables

The conditions described above have to be checked at an infinite number of points, even when using discrete stochastic variables, e. g. a finite number of scenarios for which an admissible shape is compared to a benchmark shape. To reduce the computational cost of the inequality constraints, a formulation which allows checking only a finite number of constraints is more practical. Such formulations can be derived using some properties of the underlying stochastic order (s. also [MS02, Subsection 8.1.2]). First, we will consider, where the first and second order dominance constraint have to be checked to ensure that they hold.

Theorem 26. *Let X and Y be random variables with discrete distributions and K the number of scenarios. Then*

1. $X \preceq_1 Y$ if and only if $\mathbb{P}[X \leq \eta] \geq \mathbb{P}[Y \leq \eta]$ for all $\eta \in \{Y(\omega_i) : 1 \leq i \leq K\}$
2. $X \preceq_2 Y$ if and only if $\mathbb{E}[X - \eta]_+ \leq \mathbb{E}[Y - \eta]_+$ for all $\eta \in \{Y(\omega_i) : 1 \leq i \leq K\}$

Proof. Following [MS02] and [Pac14], we prove several statements:

1 \Rightarrow follows immediately from the definitions. For \Leftarrow , we consider three cases

Let $\eta \in [y_{n-1}, y_n)$ for $2 \leq n \leq K$. The fact that Y is discrete (y_{n-1} and y_n are consecutive points) implies

$$\mathbb{P}[Y \leq \eta] = \mathbb{P}[Y \leq y_{n-1}] \leq \mathbb{P}[X \leq y_{n-1}] \leq \mathbb{P}[X \leq \eta].$$

Let $\eta < y_1$. In this case $\mathbb{P}[Y \leq \eta] = 0 \leq \mathbb{P}[X \leq \eta]$.

Let $\eta > y_K$. $\mathbb{P}[X \leq y_K] \leq \mathbb{P}[X \leq \eta]$ holds true due to the monotonicity of the distribution function. Together with the assumption, this implies $\mathbb{P}[Y \leq y_K] = 1$ and with $\mathbb{P}[Y \leq y_K] \leq \mathbb{P}[X \leq y_K]$ the inequation $\mathbb{P}[X \leq \eta] = 1 \leq \mathbb{P}[Y \leq \eta]$.

To prove 2, let $X \preceq_2 Y$ and deduce the required statement from the definitions. To prove \Leftarrow , define

$$A_C[\eta] := \mathbb{E}[C - \eta]_+ = \sum_{n=1}^K \pi_n^C [c_n - \eta]_+$$

for $C = X$ or $C = Y$ and $c_n = x_n$ if $C = X$ and $c_n = y_n$ if $C = Y$. From the assumption, we get $A_X(y_n) \leq A_Y(y_n)$ for all $n \in \{1, \dots, K\}$. A_Y is convex and piecewise linear on each of the intervals $(-\infty, y_1]$, $(y_n, y_{n+1}]$ for $n \in \{2, \dots, K\}$ and (y_K, ∞) .

Again, consider three cases:

3. Stochastic dominance constraints in shape optimization

Let $\eta \leq y_1$. Choose a $\eta_0 \leq \eta$ with $\eta_0 \leq x_1$ and define the set

$$K' := \{n \in \{1, \dots, K\} : x_n \leq y_1\}.$$

Then

$$\begin{aligned} A_X[\eta_0] - A_X[y_1] &= \sum_{n=1}^K \pi_n^X x_n - \eta_0 - \sum_{n \notin K'} \pi_n^X x_n + \sum_{n \notin K'} \pi_n^X y_1 \\ &= \sum_{n \notin K'} \pi_n^X y_1 - \eta_0 + \sum_{n \in K'} \pi_n^X x_n \\ &\leq \sum_{n \notin K'} \pi_n^X y_1 - \eta_0 + \sum_{n \in K'} x_n^X y_1 \\ &= y_1 - \eta_0. \end{aligned} \tag{3.1}$$

Additionally,

$$A_Y(\eta_0) - A_Y(y_1) = \sum_{n=1}^K \pi_n^Y y_n - \eta_0 - \sum_{n=1}^K \pi_n^Y y_n + y_1 = y_1 - \eta_0 \tag{3.2}$$

using that for $\eta \leq y_1$, the statement $A_Y(\eta) = \sum_{n=1}^K \pi_n^Y y_n - \eta$ holds.

Now let $\lambda \in [0, 1]$, such that $\eta = \lambda\eta_0 + (1 - \lambda)y_1$. As A_X is convex, we derive using (3.1), (3.2) and the assumption

$$\begin{aligned} A_X(\eta) &= \lambda A_X(\eta_0) + (1 - \lambda)A_X(y_1) \\ &= A_X(y_1) + \lambda(A_X(\eta_0) - A_X(y_1)) \\ &\leq A_X(y_1) + \lambda(y_1 - \eta_0) \\ &\leq A_Y(y_1) + \lambda(y_1 - \eta_0) \\ &= A_Y(y_1) + \lambda(A_Y(\eta_0) - A_Y(y_1)) \\ &= A_Y(\lambda\eta_0 + (1 - \lambda)y_1) = A_Y(\eta). \end{aligned}$$

Let $y_{n-1} \leq \eta \leq y_n$. Consider

$$\begin{aligned} A_X(\eta) &= \lambda A_X(y_{n-1}) + (1 - \lambda)A_X(y_n) \\ &\leq \lambda A_Y(y_{n-1}) + (1 - \lambda)A_Y(y_n) \\ &= A_Y(\lambda y_{n-1} + (1 - \lambda)y_n) = A_Y(\eta). \end{aligned}$$

Let $\eta \geq y_K$. A_X and A_Y are non-negative and non-decreasing. Then the assumption implicates

$$0 \leq A_X(\eta) \leq A_X(y_K) \leq A_Y(y_K) = 0$$

which shows $A_X(\eta) = A_Y(\eta) = 0$.

This concludes the proof. □

Theorem 26 implies that it is sufficient to check random variables against a finite number of realizations.

3.3. The stochastic dominance problem

Stochastic dominance optimization uses the stochastic orders that were introduced in the previous sections to compare admissible shapes against a given benchmark shape while minimizing another property, in our case the volume (and an additional regularization term). As the benchmark shape defines a lower limit to the stability of the admissible shapes, the optimal shape will be a shape of minimal volume, that is “at least as stable” as the benchmark shape in the sense of first or second-order stochastic dominance.

To begin, let us formulate the target functional for the stochastic dominance problem: We use a phase field with pure phases $a = -1$ and $b = 1$ as design variable and the target functional introduced in Section 2.4, which is again defined in this one-scale, strain-based context as

$$\mathcal{W}[v, u] = \int_{\mathcal{D}} C(v)\epsilon[u] : \epsilon[u] \, dx, \quad (3.3)$$

$$\mathcal{V}^\varepsilon[v] = \int_{\mathcal{D}} \chi(v) \, dx, \quad (3.4)$$

$$\mathcal{L}^\varepsilon[v] = \frac{1}{2} \int_{\mathcal{D}} \varepsilon |\nabla v|^2 + \frac{1}{\varepsilon} \psi(v) \, dx. \quad (3.5)$$

Note, that $\mathcal{V}^\varepsilon[v]$ and $\mathcal{L}^\varepsilon[v]$ have been introduced in Section 2.5 together with $\chi(v) = \frac{1}{4}(v+1)^2$.

The total free energy is defined as

$$\mathcal{E}[v, u] = \mathcal{W}[v, u] - \ell[v]$$

where $\ell[v] = \int_{\Gamma_N} g \cdot u \, da$ is the boundary term incorporating the boundary forces g on Γ_N .

The stochastic dominance optimization problem is formulated using a benchmark object described by a design variable v_b and a random variable describing displacements, which is denoted as ω . We define for a $\gamma > 0$

$$\mathcal{G}[v] = \mathcal{V}^\varepsilon[v] + \gamma \mathcal{L}^\varepsilon[v]$$

as the functional to minimize and formulate a stochastic constraint optimization problem

$$\begin{aligned} & \min_v \mathcal{G}[v] \\ \text{s. t. } & \mathcal{W}[v][\omega] \preceq \mathcal{W}[v_b][\omega_b]. \end{aligned}$$

For the order \preceq , either \preceq_1 or \preceq_2 is used. The regularization term $\mathcal{L}^\varepsilon[v]$ is applied to the target functional \mathcal{G} instead of the constraint, such that the constraint only measures stochastic orders of deformations resulting from stochastic forces acting on the shape given by the phase field v . The regularization just serves as a measure to prevent arbitrarily fine structures and is not directly dependent on the stochastic variables used here. Thus, it is advisable to not apply it in terms used in stochastic orders.

3. Stochastic dominance constraints in shape optimization

We use the methodology described above to consider $\mathcal{W}[v]$ in the target functional, utilizing the equation $\mathbb{P}[\mathcal{W}[v, u[v]] \leq \eta] = \sum_{k=1}^K \pi_k \mathcal{W}[v, u[v](\omega_k)]$. First-order dominance can be rewritten as an inequality that has to hold for all j :

$$\begin{aligned} \mathcal{W}[v, u[v]] &\preceq_1 \mathcal{W}[v_b, u[v]] & (3.6) \\ \Leftrightarrow \sum_{k=1}^K \pi_k \mathcal{H}(\mathcal{W}[v_b, \omega_j] - \mathcal{W}[v, \omega_k]) &\geq \sum_{k=1}^K \pi_k \mathcal{H}(\mathcal{W}[v_b, \omega_j] - \mathcal{W}[v_b, \omega_k]). \end{aligned}$$

Similarly, second-order dominance turns into

$$\begin{aligned} \mathcal{W}[v, u[v]] &\preceq_2 \mathcal{W}[v_b, u[v]] & (3.7) \\ \Leftrightarrow \sum_{k=1}^K \pi_k \max\{\mathcal{W}[v_b, \omega_j] - \mathcal{W}[v, \omega_k], 0\} &\leq \sum_{k=1}^K \pi_k \max\{\mathcal{W}[v_b, \omega_j] - \mathcal{W}[v_b, \omega_k], 0\}. \end{aligned}$$

These formulas are not suitable to be used in numerical optimization because they are not differentiable. Thus, we have to use smooth approximations of $\mathcal{H}(x)$ and $\max\{x, 0\}$, which will be discussed when needed in the next section.

3.4. Discretization

The domain will be discretized using multi-linear finite elements on an adaptive mesh composed of quadratic finite elements discretizing $[0, 1]^2$. The mesh is structured using a quad-tree as underlying hierarchical data structure. Here, we prescribe that the difference in levels along element faces is at most one level, i. e. there is at most one hanging node on each edge that is shared by two elements. We denote the space of continuous, piecewise bilinear finite elements by $Q_h^1(\mathcal{D}_h)$, where h is a piecewise constant mesh size function. Values at the hanging nodes are obtained by interpolation from the nodes that are sharing the same edge.

Consider a quad-tree T (also known as full four-ary tree), i. e. a tree in which every node has either zero or four children. This data structure can be used to hierarchically partition two-dimensional space, in our case the domain $\mathcal{D} = [0, 1]^2$. The root of T represents the whole domain \mathcal{D} and with every level, the domain is sectioned into four quadrants. Figure 3.2 shows an example of such a mesh and the associated quad-tree.

This mesh type implements an adaptive structured mesh with elements, that only differ by scale and translation. Thus, basis functions on the elements remain simple and can be evaluated in a computationally efficient manner. Finite element nodes can easily be identified and enumerated using hash keys and a hash map. The details will be described in the next section.

Refinement

When an element $T \in \tau$ is marked for refinement, the level-one transitions between elements have to be ensured. Thus, all neighbor elements $T_N \in \tau$ with $T_N \cap T \neq \emptyset$ have

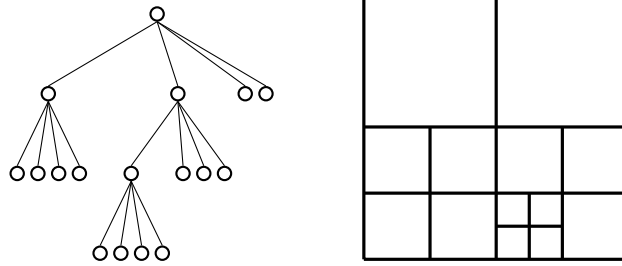


Figure 3.2.: Example of a quad-tree and the corresponding finite element mesh.

to be considered and recursively refined, if they are on a coarser level than T . Figure 3.3 shows an example for the refinement of a single element which requires a neighboring element to be refined first.

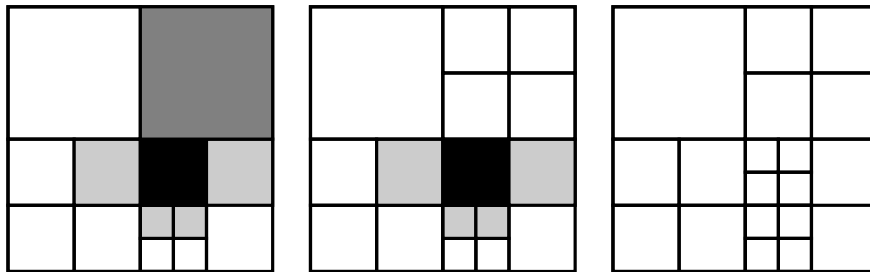


Figure 3.3.: *Left*: Example of element neighborhood (in gray) to be considered when refining an element (marked in black): light gray elements are considered, but no action is needed, gray elements need to be refined in order to limit the number of hanging nodes on edges to at most 1. *Middle*: Same mesh after the top right element has been refined. *Right*: Mesh after completed refinement.

The resulting algorithm can be implemented as lined out by the pseudo code in Algorithm 1: The function `refine(T)` checks the neighbors of T and recursively calls itself if necessary, then replaces an element T by its four child elements of the next finer level. The algorithm terminates, because each element has to be refined at most once, because refining every element refines all marked elements and transforms an admissible mesh into an admissible mesh.

The nodes of the *finite element mesh* are identified using a hash key: for a node $x \in Q_h^1(\mathcal{D}_h)$, the hash key is defined as $h = [\text{level}|x_1|x_2|x_3]$, where level is the level of the element containing the node, x_1 and x_2 are the cartesian coordinates in multiples of the local mesh width $2^{-\text{level}}$ and $x_3 = 0$ is reserved for a 3D version of this mesh, which is not used in this thesis but is implemented using oct-trees instead of quad-trees. With this structure, global node labelings can be implemented using hash-maps (`unordered_map` in C++) for good lookup performance.

When neighboring elements have different levels, *hanging nodes* are created on the shared edge (see Figure 3.2 for an example), which cannot be used as degrees of freedom

3. Stochastic dominance constraints in shape optimization

Algorithm 1: Mesh refinement with neighbor level checking.

Data: An admissible mesh with a set R of elements marked for refinement

Result: An admissible mesh where at least all elements in R have been refined

for $T \in R$ **do**

 | refine(T)

end

Function $refine(T)$

 | **for** $T_N \in \{\text{neighbors of } T\}$ **do**

 | **if** $level(T_N) < level(T) - 1$ **then**

 | refine(T_N)

 | **end**

 | **end**

 | $T \leftarrow 4$ elements of $level(T)+1$

(as that could lead to non-continuous functions). To avoid unusually complicated supports of basis functions, it is advisable to still assemble using standard hat basis functions for each element, i. e. including the hanging nodes, redistributing the associated values in a postprocessing step.

In the following, we consider the handling of hanging nodes via prolongation and restriction operators. Let u be a piecewise bilinear, globally continuous finite element function, which is uniquely defined by its values on all degrees of freedom. Let x be a hanging node and n_1^x and n_2^x the nodes that share the edge with x on the coarser of the two neighboring elements. As u is required to be globally continuous, the value at the hanging node is determined by the average of the adjacent nodes sharing the same edge. Thus, we can define the prolongation operator P as

$$Pu(x_i) = \begin{cases} \frac{1}{2}(u(n_1^x) + u(n_2^x)) & \text{if } x_i \text{ is a hanging node} \\ u(x_i) & \text{else} \end{cases}$$

and write $\hat{u} = Pu$.

To define the restriction operator R , consider a finite element operator L assembled on the full set of all nodes. The equation

$$L\hat{u} \cdot \hat{u} = LPu \cdot Pu = P^T LPu \cdot u.$$

has to hold true and we can deduce $R = P^T$.

It is important to note that neither P nor R is invertible and that $R \neq P^{-1}$, not even in the sense of a pseudo inverse! As an equivalent statement, in general, $RPu \neq u$.

The assembling of finite element operators and finite element functions can be executed on the full mesh, using the usual hat basis functions for $Q_h^1(\mathcal{D}_h)$ finite elements. All required quantities then have to be restricted or prolonged as necessary.

The mesh has been implemented using the `QuocMesh` library [QM].

3.4.1. Discretization of energies

Having defined a mesh for finite elements, we can now discretize the continuous energies discussed above. This will allow us to numerically solve the constraint optimization problem resulting from the continuous problem. We follow the usual path of discretizing all required quantities into functions in $Q_h^1(\mathcal{D}_h)$ using an interpolation operator \mathcal{I}_h and replacing all integrals by a suitable quadrature rule.

First, the phase field v and deformation u are approximated by $V \in Q_h^1(\mathcal{D})$ and $U \in Q_{h,\Gamma_D}^1(\mathcal{D}_h)$, respectively, defining the space $Q_{h,\Gamma_D}^1(\mathcal{D}_h)$ as the subset of $Q_h^1(\mathcal{D}_h)$ with vanishing trace on Γ_D . Furthermore, we require that $V|_{\Gamma_N} = 1$ for discrete phase field functions V . The volume and interface measuring terms (cf. (3.4) and (3.5)) are approximated by

$$\begin{aligned} \mathbf{V}^\varepsilon(V) &:= \sum_{T \in \mathcal{T}} |T| \sum_{k \in K_T} \omega_k \mathcal{I}_h(\chi(V(q_k))) \\ \mathbf{L}^\varepsilon[V] &:= \frac{1}{2} \sum_{T \in \mathcal{T}} |T| \sum_{k \in K_T} \omega_k \varepsilon |\nabla V(q_k)|^2 + \frac{1}{\varepsilon} \mathcal{I}_h(\Psi(V(q_k))), \end{aligned}$$

for any $V \in Q_h^1(\mathcal{D}_h)$. K_T denotes the index set of a quadrature rule and for $k \in K_T$, the quadrature weights are denoted by ω_k and the quadrature points by q_k . For the energies defined in this chapter, we use the center of mass quadrature rule ($k \in \{1\}$, $\omega_1 = 1$ and $\bar{q}_1 = (\frac{1}{2}, \frac{1}{2})^t$), as this rule is exact on bilinear functions on quadratic finite elements. As tensor we set $C(V) = ((1 - \delta)\chi(V) + V)C_{LN}$, where C_{LN} is a Lamé–Navier type tensor, as introduced in (2.4). The compliance term $\mathcal{W}[v, u[v]]$ (defined in (3.3)) is discretized as

$$\mathbf{W}[V, U[V]] := \frac{1}{2} \sum_{T \in \mathcal{T}} |T| \sum_{k \in K_T} \omega_k ((1 - \delta)\mathcal{I}_h(\chi(V(q_k))) + \delta) C_{LN} \epsilon[U(q_k)] : \epsilon[U(q_k)]$$

The Dirichlet boundary Γ_D and the inhomogeneous Neumann boundary Γ_N are resolved on the adaptive rectangular mesh.

Next, we discretize ℓ as

$$\mathbf{l}[U] := \sum_{\partial T \in \Gamma_N} \sum_{k \in K_{\partial T}} \omega_{\Gamma_N, k} \mathcal{I}_h(g(q_{\Gamma_N, k}) \cdot U(q_{\Gamma_N, k})).$$

For $k \in K_{\partial T}$, quadrature weights and quadrature points of a suitable quadrature rule on Γ_N are defined by $\omega_{\Gamma_N, k}$ and $q_{\Gamma_N, k}$. We obtain the discrete elastic energy

$$\mathbf{E}[V, U] := \mathbf{W}[V, U] - \mathbf{l}[U].$$

The discrete cost functional, which is used to define the stochastic constraints, is given by

$$\mathbf{J}[V, U] := 2\mathbf{W}[V, U] + \nu \mathbf{V}^\varepsilon[V] + \beta \mathbf{L}^\varepsilon[V]$$

for $\nu, \beta > 0$.

3. Stochastic dominance constraints in shape optimization

The stochastic constraints can again be reduced to checking a finite number of constraints. As mentioned above, approximated versions of the Heaviside and max function are used to discretize the dominance constraints. Let $\alpha > 0$ and

$$\mathcal{H}_\alpha(x) := \frac{1}{1 + \exp(-2\alpha x)},$$

$$\max_\alpha\{x, 0\} := \frac{\sqrt{x^2 + \alpha} + x}{2}$$

be approximations of $\mathcal{H}(x)$ and $\max\{x, 0\}$, respectively. These functions \mathcal{H}_α and \max_α are smooth and differentiable and allow to optimize first and second order dominance expressions numerically. To gain convergence to the exact expressions it is necessary to let $\alpha \rightarrow 0$.

The *first-order dominance* condition $\mathcal{W}[v, u[v][\omega]] \preceq_1 \mathcal{W}[v_b, u[v][\omega]]$ is approximated using the formulation given in (3.6) and the smoothed Heaviside function $\mathcal{H}_\alpha(x)$, which leads to

$$\sum_{k=1}^K \pi_k \mathcal{H}_\alpha \mathbf{W}[V_b, U[V_b][\omega_j]] - \mathbf{W}[V, U[V][\omega_k]]$$

$$\leq \sum_{k=1}^K \pi_k \mathcal{H}_\alpha \mathbf{W}[V_b, U[V_b][\omega_j]] - \mathbf{W}[V_b, U[V_b][\omega_k]] \quad \text{for all } j = 1, \dots, K.$$

Similarly, the *second-order dominance* condition $\mathcal{W}[v, u[v][\omega]] \preceq_2 \mathcal{W}[v_b, u[v_b][\omega]]$ is approximated using the smoothed max function $\max_\alpha\{x, 0\}$ and the formulation given in (3.7):

$$\max_\alpha\{\mathbf{W}[V, U[V][\omega_k]] - \mathbf{W}[V_b, U[V_b][\omega_j], 0]\}$$

$$\leq \max_\alpha\{\mathbf{W}[V_b, U[V_b][\omega_k]] - \mathbf{W}[V_b, U[V_b][\omega_j], 0]\} \quad \text{for all } j = 1, \dots, K.$$

The discretized optimization problem can now be written as

$$\min_v \mathbf{G}[V] \tag{3.8}$$

$$\text{s. t. } \mathbf{W}[V] \preceq \mathbf{W}[V_b],$$

where

$$\mathbf{G}[V] = \mathbf{V}^\varepsilon[V] + \gamma \mathbf{L}^\varepsilon[V].$$

for a $\gamma > 0$ and \preceq being \preceq_1 or \preceq_2 .

Problem (3.8) is optimized using the IPOPT package [WB06], which uses an interior point method to optimize the constrained problem. The optimizations are started with relatively large $\varepsilon > 0$ (phase field regularization) and $\alpha > 0$ (stochastic regularization) parameters. After an IPOPT optimization has converged (i. e. the interior point method

found an iterand satisfying the required thresholds given in [WB06, Section 2.5]), the mesh is adaptively refined where the phase field is steep and, ε and α are decreased by a factor the optimization is restarted. The optimization algorithm has converged once an optimization run of IPOPT has converged for values $\varepsilon < \text{tol}_\varepsilon$ and $\alpha < \text{tol}_\alpha$, where $\text{tol}_\varepsilon > 0$ and $\text{tol}_\alpha > 0$ are threshold values for the respective parameters.

To be able to calculate the derivatives of the constraints (which are required by IPOPT), we have to provide them using a formulation, that is suitable for numerical computation. Let δ denote the Gateaux-derivative. The derivative of $\mathbf{G}[V]$ can be computed directly as $\delta_V \mathbf{G}[V](\Theta) = \delta_V \mathbf{V}^\varepsilon[V](\Theta) + \beta \delta_V \mathbf{L}^\varepsilon[V](\Theta)$ with

$$\begin{aligned} \delta_V \mathbf{V}^\varepsilon[V](\Theta) &= \sum_{T \in \mathcal{T}} |T| \sum_{k \in K_T} \omega_k \partial_V \chi(V(q_k)) \Theta \, dx \quad \text{and} \\ \delta_V \mathbf{L}^\varepsilon[V](\Theta) &= \sum_{T \in \mathcal{T}} |T| \sum_{k \in K_T} \omega_k \varepsilon \nabla V(q_k) \cdot \nabla \Theta + \frac{1}{2\varepsilon} \mathcal{I}_h(\partial_V \Psi(V(q_k)) \Theta) \, dx, . \end{aligned}$$

For the derivative $\delta_V(\mathbf{W}[V, U[V]]) = \partial_V \mathbf{W}[V, U[V]] + \partial_U \mathbf{W}[V, U[V]](\partial_V U[V])$ it is advisable to use the dual formulation, as a direct approach is computationally expensive. We define

$$P := (\partial_{UU}^2 \mathbf{E}[V, U[V]]^{-1})(\partial_U \mathbf{W}[V, U[V]]) \quad (3.9)$$

(the *dual problem*) and consider

$$\begin{aligned} \delta_V \mathbf{W}[V, U[V]] \Theta &= \partial_V \mathbf{W}[V, U[V]] \Theta + \partial_{UU}^2 \mathbf{E}[V, U[V]](P)(\partial_V U[V] \Theta) \\ &= \partial_V \mathbf{W}[V, U[V]] \Theta - \partial_{UU}^2 \mathbf{E}[V, U[V]] P (\partial_{UU}^2 \mathbf{E}^{-1}[V, U[V]](\partial_{UV}^2 \mathbf{E}[V, U[V]] \Theta)) \\ &= \partial_V \mathbf{W}[V, U[V]] \Theta - \partial_{UV}^2 \mathbf{E}[V, U[V]] P \Theta. \end{aligned}$$

For the second equation, we use the implicit function theorem which states that

$$\partial_V U[V] = -(\partial_{UU}^2 \mathbf{E}^{-1}[V, U[V]])(\partial_{UV}^2 \mathbf{E}[V, U[V]])$$

in a neighborhood of V . Note, that we could use the same procedure to find $\delta_V \mathbf{J}[V, U[V]]$, if we incorporated $\mathbf{V}^\varepsilon[V]$ and $\mathbf{L}^\varepsilon[V]$ in the constraint.

For the energies $\mathbf{W}[V, U[V]]$ and $\mathbf{E}[V, U]$ described here, (3.9) is solved by $P = 2U$ and thus, the derivative of $\mathbf{W}[V, U[V]]$ can be written as

$$\delta_V \mathbf{W}[V, U[V]] = -\partial_V \mathbf{W}^\delta[V, U]$$

using $\delta_V \mathbf{W}[V, U](\Theta) = \frac{1}{2} \sum_{T \in \mathcal{T}} |T| \sum_{k \in K_T} \omega_k (1 - \delta) \mathcal{I}_h(\partial_V \chi(V)) \Theta C_{LN} \epsilon[U(q_k)] : \epsilon[U(q_k)]$ and $\delta_V \mathbf{V}^\varepsilon[V]$ and $\delta_V \mathbf{L}^\varepsilon[V]$.

3.5. Numerical Results

In this chapter, numerical result for two stochastic setups — a pressure plate and a cantilever — are presented. As domain we choose $\mathcal{D} = [0, 1]^2$, as parameters for the Lamé–Navier tensor $\lambda = \mu = 80$, for the soft material a factor $\delta = 10^{-4}$ and for \mathbf{G} a weight of $\gamma = 0.015625$.

3. Stochastic dominance constraints in shape optimization

Cantilever

The first application is the shape optimization of a 2D cantilever. The cantilever is fixed on the left-hand side, which implies that u obeys homogeneous Dirichlet boundary conditions. On three segments of the lower boundary, piecewise constant loads are applied. In each scenario, a single load is applied to one of the segments. Different directions, probabilities and absolute values of loads are compared using two different stochastic loading configurations as depicted in the first and second row of Figure 3.4, respectively.

The optimization was started with a regularization parameter of $\varepsilon = 0.025$, which was multiplied by 0.75 after each mesh refinement until $\varepsilon = 5.93 \cdot 10^{-3}$ was reached for the first-order dominance in the varying load and probability configuration and $\varepsilon = 7.91 \cdot 10^{-3}$ was reached in all other cantilever configurations. The regularization parameter of the smoothed Heaviside and max functions α was initialized with 1 and decreased until it reached $1.95 \cdot 10^{-3}$. The results of the optimization for first and second-order dominance are shown in Figure 3.4, the resulting stresses in the optimal shapes in Figure 3.5.

We compare two different setups of 15 scenarios: One with equal absolute value and equal probability of the loads and one with three different absolute values and probabilities for the loads on the three different bottom boundary parts (with ratios for probabilities $1, \frac{2}{3}$ and $\frac{1}{3}$ and for loads 1, 2 and 3, where the strongest and least likely loads are furthest to the right).

The resulting volumes are listed under the corresponding phase field of the optimal shapes and benchmark. In the plots of the cumulative distribution function and distributed survival functions, the values for the benchmark shapes are plotted in red, the values for the respective result in blue. The inequalities required for these functions are clearly fulfilled for all optimized shapes, i. e. the cumulative distribution function for the first-order dominance jumps earlier than the one of the benchmark and the integrated survival function of the second-order dominance results remains below the one of the benchmark. In terms of the cumulative distribution function this allows for later jumps for some scenarios, if these derivations are compensated for later in the appropriate integral sense.

Pressure plate

As a second application, we consider a 2D carrier plate. In this construction, the supporting construction between a floor slab and an upper plate is optimized, where the lower boundary is the Dirichlet boundary and the forces act on parts of the upper boundary. Here, the stochastic loads consist of 10 scenarios consisting of 10 single loads.

In this setup the absolute value and probability of the loads vary in between the different scenarios: High probability loads come with small absolute value (ratio 1 : 4 for both absolute value and probability). The phase field parameter ε was initialized with $3.13 \cdot 10^{-2}$ and multiplied by 0.75 after each mesh refinement until a value of $1.32 \cdot 10^{-2}$ was reached. α was decreased from 1 to $1.95 \cdot 10^{-3}$ and $7.81 \cdot 10^{-3}$ for the first- and second-order optimizations, respectively.

The load configurations, benchmark shape and results are displayed in Figure 3.6 (again, in the plots, the values corresponding to the benchmark shaped are drawn in red, the values of the results in blue). The cumulative distribution functions and integrated survival function show, that the dominance constraints are fulfilled for both first- and second-order dominance constraints. Figure 3.7 depicts the stresses resulting from the different loads on the optimal shape.

3.6. Conclusion

We formulated a model that considers risk aversion in the context of linear elasticity in the constraints of an optimization problem. The numerical optimization is done on an adaptive finite element mesh using quadratic $Q_h^1(\mathcal{D}_h)$ elements and an interior point method. The results show shapes that dominate the benchmark while still reducing the volume.

The model could easily be extended to 3D elasticity, where the adaptive mesh would allow for fine structures to form without making the optimization computationally infeasible. Furthermore, real-world benchmarks could be used to e.g. find cost-effective alternatives to machined parts in the context of engineering.

3. Stochastic dominance constraints in shape optimization

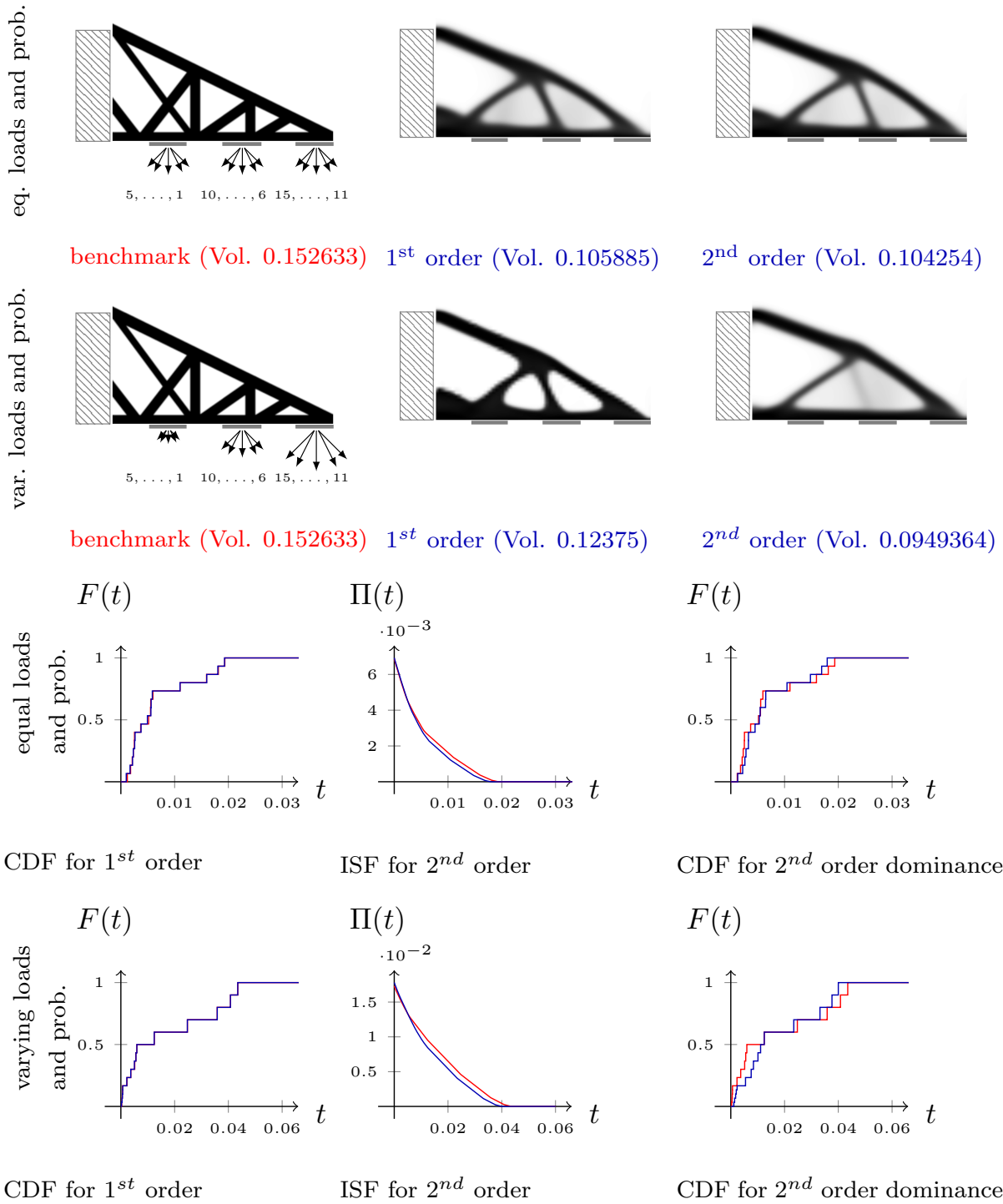


Figure 3.4.: Results for first- and second-order stochastic dominance in the cantilever scenario and corresponding cumulative distribution and survival functions

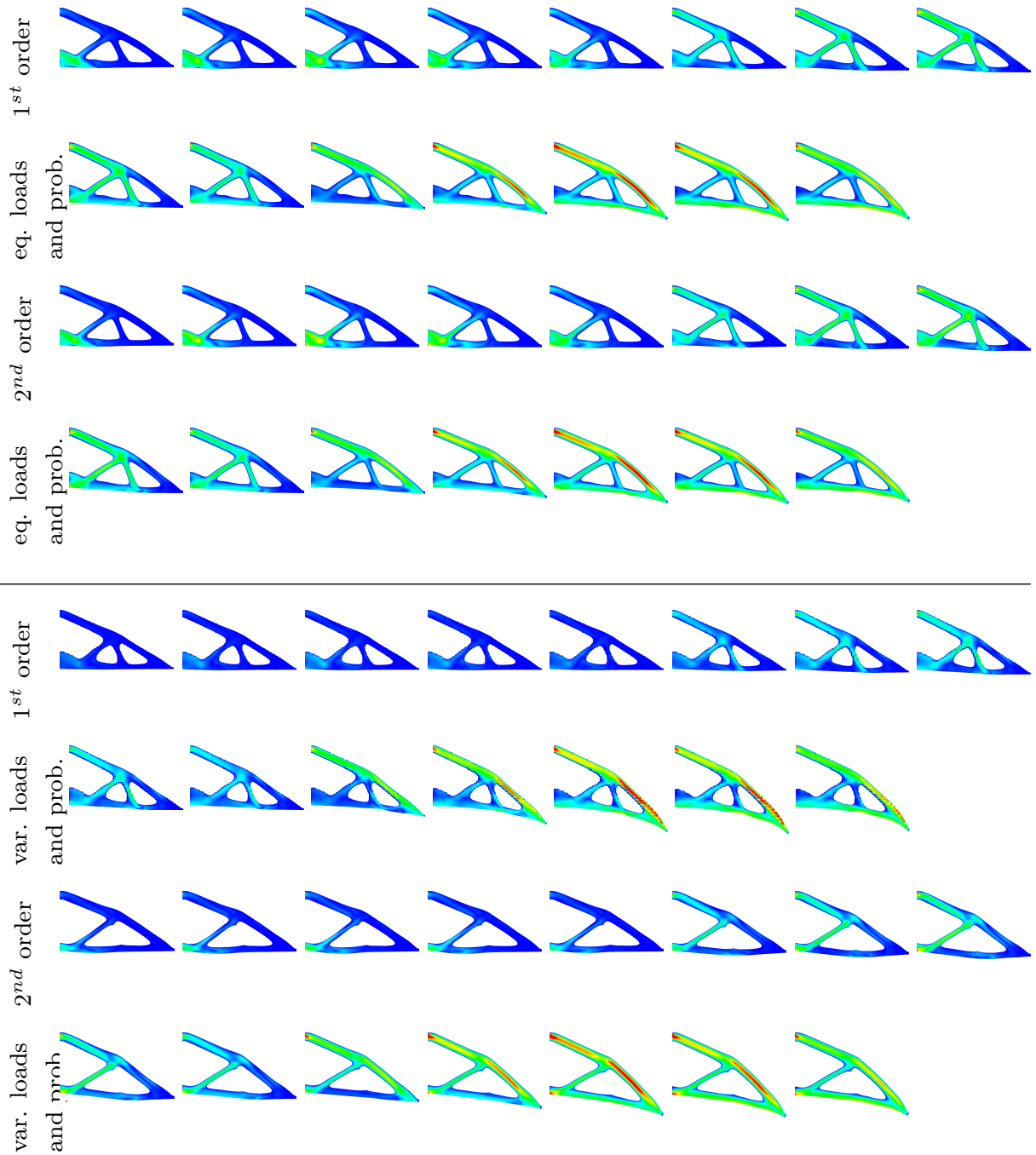



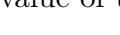


Figure 3.5.: Thresholded von Mises stresses for the scenario in the cantilever setup, first- and second-order dominance for the equal load and probability setup (row one and two, color-coded as 0  4.99 and 0  4.85) and the varying load and varying probability setup (row three and four, color-coded as 0  9.05 and 0  6.87). Stresses bigger than the maximum value of the scale are mapped to red.

3. Stochastic dominance constraints in shape optimization

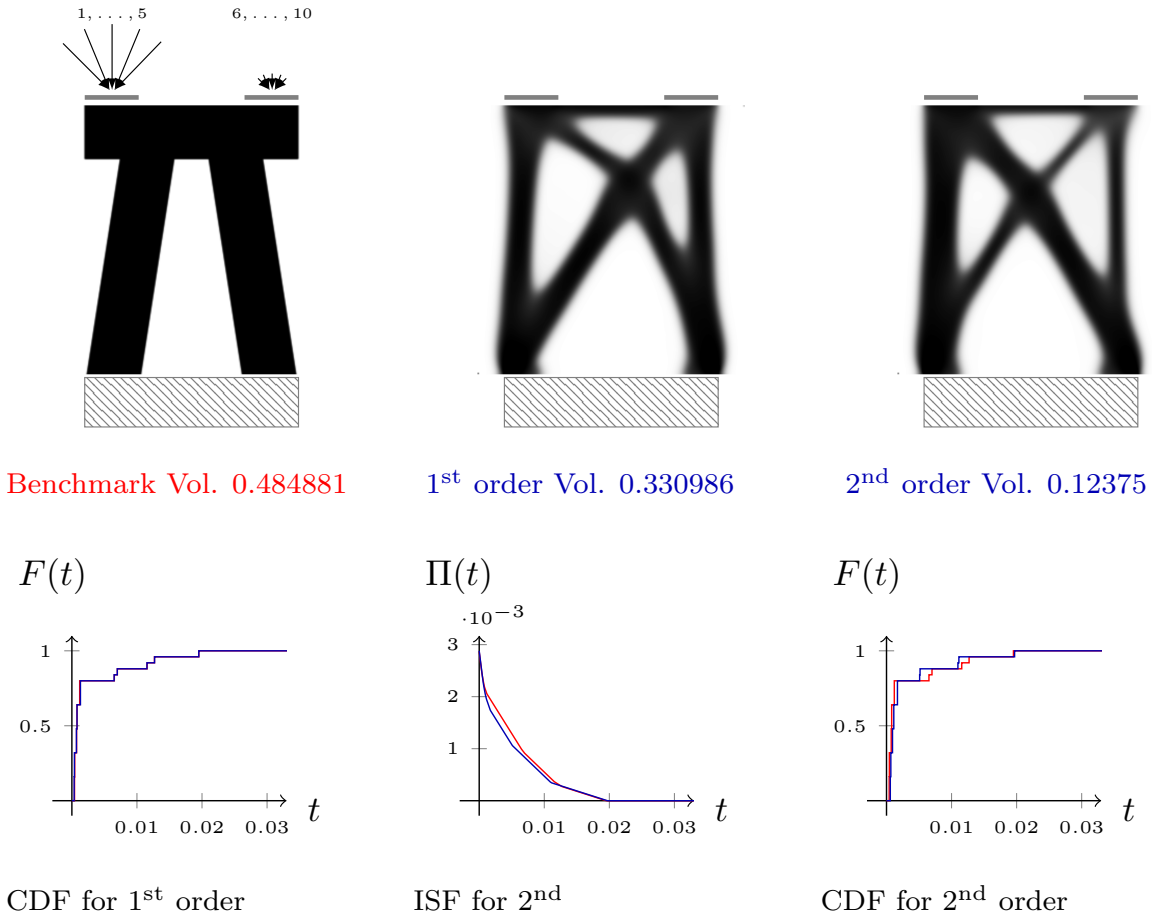


Figure 3.6.: Results for first- and second-order stochastic dominance in the carrier plate scenario and corresponding cumulative distribution as well as survival functions

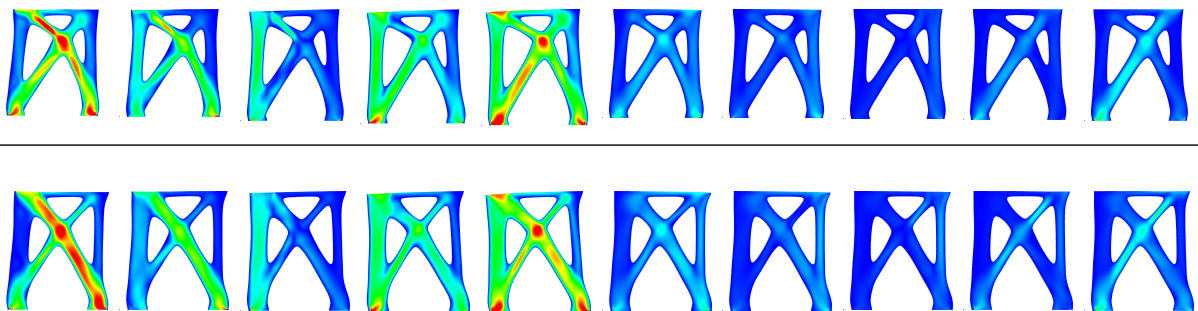


Figure 3.7.: Thresholded stresses for each scenario in the weighted carrier plate setup, first- and second-order dominance, color-coded as 0 3.21 and 0 3.24. Stresses bigger than the maximum value of the scale are mapped to red.

4. Composite materials and branching structures

The formation of microstructures is a common phenomenon in elastic shape optimization (we refer to [Ben95] and [All02] for an overview of these topics). Depending on the geometry of the computational domain and the loads applied to it, microstructures appear and can form periodic or branching-type structures. This phenomenon is supported by microstructures appearing in many different areas of nature, e. g. branching patterns in or near the compacta of bones. These microstructures usually form fine-scale structures of a particular size, i. e. a fixed ratio between the macroscopic object and the fine-scale structure exists.

In the context of multiscale materials, homogenization has emerged as an important concept to upscale the microscopic properties to the macroscale. This methodology has been described in [CD99, Mil02] and in detail in [All02]. The concept of homogenization also extends to many engineering applications (cf. [MBD⁺15] and [NNWSA11] for examples). This chapter can be seen as preliminary work to understand the formation of branching microstructures in elastic shape optimization and to develop a homogenization type approach to this kind of problem. Alternatively, true two-scale materials can be approached numerically by the Heterogeneous Multiscale Method (HMM) [EE05, EE03, EEH03, EMZ05], which explicitly simulates periodic microstructures at given points of the macroscopic domain.

In this chapter, we study domains that can be decomposed into several subdomains and compatibility conditions will be considered. Each subdomain will be a quadratic cell on which a shape will be optimized and can represent locally periodic or branching type structures. The model discussed in this chapter is an extension of models described by Vantzios [Van15] and Luethen [Lüt16]. In this chapter, domains that can be decomposed into several subdomains and compatibility conditions will be considered. Each subdomain will be a quadratic cell on which a shape will be optimized.

In contrast to the two other models discussed in this thesis, the shapes in this chapter will be modeled using a stress-based formulation of linear elasticity and will be optimized using an alternating algorithm.

4. Composite materials and branching structures

4.1. Problem formulation

Let $\mathcal{D}_{\text{comp}} \subset \mathbb{R}^2$ be a domain composed of several open subdomains \mathcal{D}_i , $i \in \mathcal{I}$ for an index set \mathcal{I} , s. t. $\cup_{i \in \mathcal{I}} \bar{\mathcal{D}}_i = \bar{\mathcal{D}}_{\text{comp}}$ and $\mathcal{D}_i \cap \mathcal{D}_j = \emptyset$ for all $i, j \in \mathcal{I}$. Each subdomain is a rectangle $[a_1, a_2] \times [b_1, b_2]$ and

1. is either a facet of an adjacent subdomain (e.g. there is a subdomain $(a_2, a_3) \times (b_1, b_2)$ sharing that facet $\{a_2\} \times (b_1, b_2)$ with the subdomain $(a_1, a_2) \times (b_1, b_2)$),
2. or splits into two facets (of equal length) of two adjacent subdomains (e.g. there are subdomains $(a_2, a_3) \times (b_1, \frac{b_1+b_2}{2})$ and $(a_2, a_3) \times (\frac{b_1+b_2}{2}, b_2)$ whose facets $\{a_2\} \times (b_1, \frac{b_1+b_2}{2})$ and $\{a_2\} \times (\frac{b_1+b_2}{2}, b_2)$ result from a splitting of the facet $\{a_2\} \times (b_1, b_2)$),
3. or is on the facets resulting from a splitting of a facet of an adjacent subdomain (as described in item 2),
4. or is a boundary facet.

See Figure 4.1 for a sketch of these domain types. The four facets of each subdomain can be of different types.

We assume, that $\mathcal{D}_{\text{comp}}$ and \mathcal{D}_i for all i are Lipschitz-domains and that each subdomain \mathcal{D}_i contains a certain part of the elastic object — the shape which will be optimized. Denote the associated characteristic function of the elastic object as χ_i and consider the continuous extension to $\bar{\mathcal{D}}_i$ in BV (cf. [AFP00, Remark 3.22]). Considering the functions χ_i as functions on $\mathcal{D}_{\text{comp}}$, the shape we are investigating is defined via $\sum_{i=1}^M \chi_i$, where M is the number of subdomains.

Each subdomain D_i (also sometimes denoted as a *geometrical subdomain*) has a *reference domain* assigned. Several geometric subdomains can have the same reference domain. This reference domain is mapped onto the geometric subdomains by a combination of a translation, a rotation by a multiple of $\frac{\pi}{2}$ and a reflection along symmetry axes. Shapes and forces are updated on reference domains and then transferred onto geometric subdomains. Neighboring geometrical subdomains using the same reference domain build periodical structures. An example is depicted in Figure 4.2.

The resulting domain consists of periodic subdomains, branching subdomains, that have branching boundary conditions in one direction (perpendicular to the boundary of the domain) and periodic boundary conditions in the other, corner subdomains that have branching periodic boundary conditions in both coordinate directions and coupling subdomains, that have branching boundary conditions perpendicular to the domain boundary and couple the corner and branching cells parallel to the boundary.

Only one reference domain of each type is simulated, as all subdomains of the same type are identical (up to translations, rotations and reflections). As a consequence, the domain sketched in Figure 4.2 can later be numerically optimized by simulating the thirteen reference domains only.

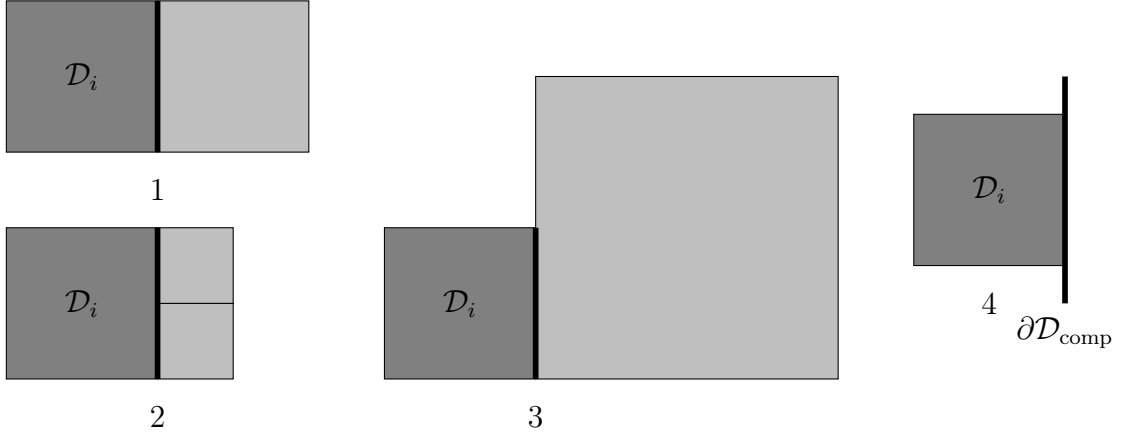


Figure 4.1.: The different local subdomain configurations of a single facet.

4.1.1. Elastic energy and compliance

To optimize the shape, we again use an elastic energy to solve the linear elastic equation. This elastic energy is (again) defined as $\mathcal{E}[v, u] : L^2(\mathcal{D}, [-1, 1]) \times W^{1,2}(\mathcal{D}, \mathbb{R}^d) \rightarrow \mathbb{R}$,

$$\mathcal{E}[v, u] = \frac{1}{2} \int_{\mathcal{D}} C \epsilon[u] : \epsilon[u] \, dx - \int_{\Gamma_N} f \cdot u \, da. \quad (4.1)$$

We recall, that in Chapter 2 the symmetrized gradient $\epsilon[u] = \frac{Du^t + Du}{2}$ and a fourth order tensor C have been introduced. Using the relation

$$\sigma = C \epsilon[u]$$

the displacements can be connected to the *stress*, which describes the internal forces associated with the displacements u . As the equilibrium displacement is a uniquely determined minimizer of (4.1) (up to rigid body motions), it is possible to equivalently use the stress in the formulation of the elastic shape optimization problem. This formulation is used here, as it allows for a simpler and more elegant formulation of branching type problems (compared to the rather involved formulations of this kind of problems using displacements and strains).

Following the ideas of [Van15, Lüt16] we now derive the minimization problem for stresses by rewriting the compliance $\int_{\mathcal{D}} C \epsilon[u] : \epsilon[u] \, dx$ in terms of stresses

$$\mathcal{W}[v] = \frac{1}{2} \int_{\mathcal{D}} C^{-1} \sigma : \sigma \, dx = \frac{1}{2} \min_{\tau \in \Sigma_{\text{ad}}} \int_{\mathcal{D}} C \tau : \tau \, dx =: \mathcal{W}[\tau, v], \quad (4.2)$$

where τ is minimized over the admissible set of

$$\Sigma_{\text{ad}} = \{\sigma = \sigma^t, \operatorname{div} \sigma = 0, \sigma \text{ is compatible with boundary conditions}\} \quad (4.3)$$

4. Composite materials and branching structures

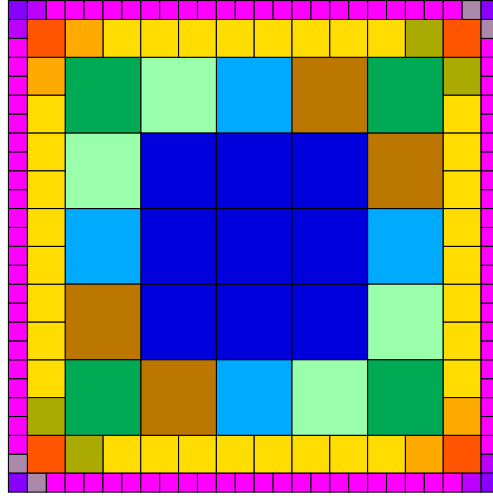


Figure 4.2.: Sketch of a composite domain consisting of periodic cells (■), branching periodic cells (■ ■ ■), double branching periodic corner cells (■ ■ ■) and coupling cells (■ ■ ■ ■ ■ ■).

of symmetric, divergence-free stress tensors that are compatible with the prescribed boundary conditions. The general term “boundary conditions” refers to the conditions imposed by the respective types of facets (as described above). In this chapter, the phase field v will be chosen to have the pure phases $a = \delta$ and $b = 1$ as a regularized version of $a = 0$ and $b = 1$. This leads to a regularization that is slightly different from the one used in the other chapters. Instead of forcing it towards the pure phases and adding a regularization parameter δ in the tensor, we directly force the phase field towards a regularized version of the pure phases. Note, that the results presented in Section 2.5 still hold true, requiring only minor modifications in the statements and proofs.

When Kohn and Wirth analyzed the expected branching periodic structures in [KW14, KW15], they chose the Poisson ratio $\nu = 0$ to simplify the analysis. This assumption is not expected to have a strong influence on the results, as optimal structures (and structures close to the optimum) consist of truss-like structures, for which lateral contractions are not of major importance. To achieve compatible results, let $C(v) = \nu C_{LN}$, where C_{LN} is the elastic tensor of the linearized Lamé–Navier model (s. (2.4)), setting the *Poisson ratio* $\nu = 0$ in this chapter. We define this tensor by its inverse using *Young’s modulus* E and ν . These values can be converted from and to λ and μ by

$$E = \frac{\mu(3\lambda + 2\mu)}{\lambda + \mu}, \quad \nu = \frac{\lambda}{2(\lambda + \mu)},$$

$$\lambda = \frac{E\nu}{(1 + \nu)(1 - 2\nu)}, \quad \mu = \frac{E}{2(1 + \nu)}.$$

For a motivation of these constants and their physical meaning, we refer to [Cia88, Chap-

ter 3.8]. The Lamé–Navier tensor can now be given in Voigt notation as

$$C_{LN}^{-1} = \frac{1}{E} \begin{pmatrix} 1 & -\nu & 0 \\ -\nu & 1 & 0 \\ 0 & 0 & 2 + 2\nu \end{pmatrix}.$$

With this choice we obtain

$$C_{LN}^{-1} = \frac{1}{E} \begin{pmatrix} 1 & 0 & 0 \\ 0 & 1 & 0 \\ 0 & 0 & 2 \end{pmatrix}.$$

and we can rewrite the application of the tensor to stresses as

$$C^{-1}\tau : \tau = \frac{1}{2\mu\nu} (\tau_{11}^2 + \tau_{22}^2) + \frac{1}{\mu\nu} \tau_{12}^2 = \frac{1}{2\mu\nu} |\tau|^2.$$

The compliance energy (4.2) then simplifies to

$$\mathcal{W}[v, \tau] = \int_{\mathcal{D}_i} \frac{1}{2\mu\nu} |\tau|^2 dx.$$

In addition to measuring deformations in terms of stresses, the shape has to be associated with a cost as well. The stresses σ have no direct influence on these terms, as they measure quantities of the shape only. Thus, the simplifications made in $\mathcal{W}[v]$ remain true. We measure the volume of a shape by integrating an approximated characteristic function

$$\mathcal{V}^\varepsilon[v] = \int_{\mathcal{D}_i} \chi[v] dx$$

where $\chi[v] = v$ ($v \in [\delta, 1]$ as noted above) and the perimeter by

$$\mathcal{L}^\varepsilon[v] = \int_{\mathcal{D}_i} \frac{1}{\varepsilon} \psi(v) + \frac{\varepsilon}{2} |\nabla v|^2 dx.$$

The function

$$\psi(v) = \begin{cases} \frac{32}{\pi^2} (1-v)(v-\delta) & v \in [\delta, 1] \\ \infty & \text{else} \end{cases}$$

denotes a double-well potential suitable for the phase field that is used here. Its minima are $v = \delta$ and $v = 1$.

The target functional $\mathcal{J}[v]$ can then be (as in the other chapters) written as

$$\mathcal{J}[v] = \mathcal{W}[v] + \nu \mathcal{V}^\varepsilon[v] + \beta \mathcal{L}^\varepsilon[v] \quad (4.4)$$

for $\nu, \beta > 0$. Note, that the structure of $\mathcal{J}[v, \tau]$ does not differ from the strain based formulation. The only differences are the usage of σ instead of $\epsilon[u]$ and the change in phase field values representing the pure phases. As neither of these changes has a fundamental influence on the solution of the linear elastic equation, we expect that the resulting optimal shapes are similar to the ones, that would result from a suitable strain based formulation of the same problem.

4.2. Discretization

In this section, the question how to computationally minimize over the set of admissible stresses will be discussed. The conditions to σ prescribed by Σ_{ad} in (4.3) have to be transcribed into equations using quantities of a suitable discretization. This discretization is constructed using a *finite volume* method.

Again, let $\mathcal{D}_{\text{comp}} \subset [0, 1]^2$ and $\mathcal{D}_i \subset \mathcal{D}_{\text{comp}}$ a subdomain as described above, $\mathcal{D}_{h,i}$ a finite decomposition of \mathcal{D}_i into $N \times N$ rectangular elements of equal size and denote the cell at position i, j by T_{ij} . Let X_h be the set of nodes and

$$E_h := \{\bar{T}_{ij} \cap \bar{T}_{kl} : 0 \leq i, k < M, 0 \leq j, l < N, i \neq k \vee j \neq l\} \\ \cup \{\bar{T}_{ij} \cap \partial\mathcal{D} : 0 \leq i < M, 0 \leq j < N\}$$

the set of edges in $\mathcal{D}_{h,i}$. For each cell, a local indexing is introduced by numbering the edges counterclockwise, starting at the top (s. Figure 4.3 for an example).

To discretize admissible stresses, we again consider the definition of Σ_{ad} of (4.3). The symmetry of the stress tensor then transforms into a balance of torques: If $r = (x_1, x_2)^T$, let $r^\perp = (-x_2, x_1)^T$. Then

$$0 = \int_T \sigma_{21} - \sigma_{12} \, dx \tag{4.5} \\ = \int_T \operatorname{div} \sigma r^\perp + \sigma^t : \nabla r^\perp \, dx = \int_T \operatorname{div}(\sigma r^\perp) \, dx \\ = \int_{\partial T} n \cdot (\sigma r^\perp) \, da = \int_{\partial T} r \times (\nu \cdot \sigma) \, da.$$

The first equality holds since $\operatorname{div} \sigma = 0$ and $\nabla r^\perp = \begin{pmatrix} 0 & 1 \\ -1 & 0 \end{pmatrix}$, the third holds due to Gauss' theorem and the fourth because $r \times x = r^\perp \cdot x$. Equation (4.5) constitutes a conservation law along the edges of an element. Similarly, the divergence-free stress transforms into a balance of forces, which are defined as average forces across edges e_j of an element T as

$$f_j = \frac{\int_{e_j} n_j \cdot \sigma \, dl}{\int_{e_j} dl}.$$

Figure 4.3 gives two examples of force discretizations on finite volume elements. Denoting as \mathbf{f}_i the force vector on edge i and as $\mathbf{f}_{i,j}$ its j -th component, we can conclude that

$$0 = \int_T \operatorname{div} \sigma \, dx = \int_{\partial T} \nu \cdot \sigma \, ds = \sum_{j=1}^4 \int_{e_j} \nu \cdot \sigma \, ds \\ = (\mathbf{f}_{1,1} + \mathbf{f}_{4,1}) - (\mathbf{f}_{2,2} + \mathbf{f}_{3,2}).$$

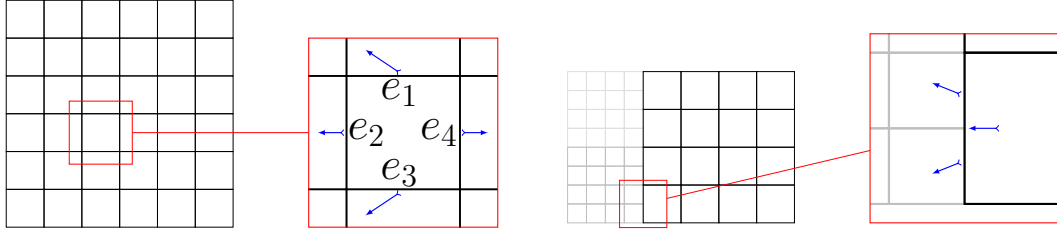


Figure 4.3.: Discretization of forces as vector-valued degrees of freedom on the interior cells of the finite volume mesh (left) and on a facet with prescribed branching-type boundary conditions (right). The numbering of the edges is displayed on the left.

The conservation laws can easily be enforced by the finite volume method by adding the respective equations for each cell to a constraint matrix \mathbf{A} . This matrix is part of a linear system $\mathbf{A}\mathbf{f} = \mathbf{b}$ and has a block structure, that is induced by the three different types of conditions on the forces.

$$\mathbf{A} = \begin{bmatrix} \mathbf{A}_f \\ \mathbf{A}_t \\ \mathbf{A}_{bc} \end{bmatrix}, \quad \mathbf{b} = \begin{bmatrix} 0 \\ 0 \\ \mathbf{b}_{bc} \end{bmatrix}.$$

The index f refers to the block prescribing the force balance, the index t to the conservation of torque and the index bc to the blocks defining the boundary conditions. The equations leading to all blocks have been described above.

To discretize the required energy functionals, a discretization of $|\sigma|^2$ is needed. From the definition of the discretized forces, we conclude for each cell

$$\begin{aligned} \int_{e_1} \sigma_{21} &= h\mathbf{f}_{1,1} dl, & \int_{e_1} \sigma_{22} &= h\mathbf{f}_{1,2} dl, & \int_{e_2} \sigma_{11} &= h\mathbf{f}_{2,1} dl, & \int_{e_2} \sigma_{12} &= h\mathbf{f}_{2,2} dl, \\ \int_{e_3} \sigma_{21} &= h\mathbf{f}_{3,1} dl, & \int_{e_3} \sigma_{22} &= h\mathbf{f}_{3,2} dl, & \int_{e_4} \sigma_{11} &= h\mathbf{f}_{4,1} dl, & \int_{e_4} \sigma_{12} &= h\mathbf{f}_{4,2} dl. \end{aligned}$$

With these equations at hand, we rewrite (using the notation e_1 and e_2 for the unit vectors)

$$\begin{aligned} |\sigma|^2 &= |e_1\sigma|^2 + |e_2\sigma|^2 \\ &= \frac{1}{2} (|n_2 \cdot \sigma|^2 + |n_4 \cdot \sigma|^2) + \frac{1}{2} (|n_1 \cdot \sigma|^2 + |n_3 \cdot \sigma|^2) \\ &\approx \frac{1}{2} \sum_{i=1}^4 \sum_{j=1}^2 |\mathbf{f}_{i,j}|^2. \end{aligned}$$

Using this approximation, we can discretize the stored elastic energy using the formula

$$\mathbf{E}[V] = \frac{1}{2} \sum_T h^2 \sum_{i=1}^4 \sum_{j=1}^2 \frac{(\mathbf{f}_{i,j}(T))^2}{VE},$$

4. Composite materials and branching structures

with $\mathbf{f}_i(T)$ denoting the force vectors on the edges of the cell T , subject to the constraint $\mathbf{A}\mathbf{f} = \mathbf{b}$.

Optimizing the forces

The main difference between algorithms optimizing a single branching or periodic cell [Van15, Lüt16] and the algorithm optimizing a domain consisting of several cells described here is in the constraints to the forces, which in the multi-cell case also contain coupling conditions between cells. Finding the energetically optimal deformation is achieved by solving

$$\begin{aligned} \min \quad & \frac{1}{2} \mathbf{f}^t \mathbf{M} \mathbf{f}, \\ \text{s. t.} \quad & \mathbf{A} \mathbf{f} = \mathbf{b}. \end{aligned}$$

Using a Lagrangian, this problem can be rewritten into a single system of equations [Lüt16]. First consider

$$\mathbf{L} = \frac{1}{2} \mathbf{f}^t \mathbf{M} \mathbf{f} + \boldsymbol{\lambda}^t (\mathbf{b} - \mathbf{A} \mathbf{f}).$$

A solution of the constraint optimization is given by a saddle point of \mathbf{L} . There $\partial_f \mathbf{L} = 0$ and — because \mathbf{M} is invertible — we can conclude

$$\begin{aligned} \mathbf{f} &= \mathbf{M}^{-1} \mathbf{A}^t \boldsymbol{\lambda} \quad \text{and} \\ \mathbf{A} \mathbf{f} &= \mathbf{A} \mathbf{M}^{-1} \mathbf{A}^t \boldsymbol{\lambda} = \mathbf{b}. \end{aligned} \tag{4.6}$$

These equations define forces \mathbf{f} and a dual solution $\boldsymbol{\lambda}$. If \mathbf{A} is regular, $\mathbf{Z} = \mathbf{A} \mathbf{M}^{-1} \mathbf{A}^t$ is regular, too. Finding the optimal deformation has now reduced to solving $\mathbf{Z} \boldsymbol{\lambda} = \mathbf{b}$, which can be achieved by a number of efficient numerical methods depending on the actual dimensions of the matrix. Note that $\ker \mathbf{A}^t = \{0\}$ implies that \mathbf{Z} is positive definite (which implies invertibility).

Rank considerations

In general $\ker \mathbf{A}^t \neq \{0\}$, but equality can be achieved by removing certain rows of \mathbf{A} , i. e. conditions to the forces. Which rows can be removed depends on the number of different cell types set up of cells of these cell types.

For domains consisting of a single subdomain \mathcal{D}_i with either periodic, branching periodic or non-periodic boundary conditions, the linear dependencies can be reduced to a small number of cases (cf. [Lüt16]). For composite domains consisting of several subdomains with different coupling and boundary conditions on the other hand, the number, type and complexity of linear dependencies increases. An algorithm to analyze the rank of the constraint matrix resulting of such domains can be designed by considering the structure of the corresponding system of equations:

Each row in \mathbf{A} represents a constraint on admissible forces and for all but the boundary conditions, the corresponding right-hand side entries equal 0. A set of linear dependent rows of \mathbf{A} represents a number of equations, of which one can be replaced by a combination of the others if the corresponding right-hand side entries are compatible. To define the correct meaning of “compatible”, consider the corresponding right-hand side entries \mathbf{b}_i and the weights of the linear dependency equation which solves $\sum_{i \in I} \mathbf{a}_i \mathbf{A}_i = 0$ for certain rows $(\mathbf{a}_i)_{i \in I} =: \mathbf{A}_i$ of \mathbf{A} and a suitable index set I . An equation F_i can be replaced by $\mathbf{A}_j, j \in I \setminus \{i\}$, iff $\sum_{j \in I} \mathbf{a}_j \mathbf{b}_j = 0$, as in that case $\sum_{j \in I \setminus \{i\}} \mathbf{a}_j \mathbf{A}_j$ already solves the equation \mathbf{A}_i with right-hand side \mathbf{b}_i . This check can be numerically implemented using e.g. a QR-decomposition to find a basis of the kernel of \mathbf{A} . The matrix can then be regularized by iteratively removing redundant equations until \mathbf{A} has full (column-)rank.

Usually, the basis vectors of the kernel of \mathbf{A} consist of a medium to large number entries of several cell types. Especially when increasing the number of different cells in a domain $\mathcal{D}_{\text{comp}}$, this reduces the precision of the numerical solution, i.e. the admissibility of the forces. Thus, this method is only suitable up to a certain number of cell types and a certain numerical precision (s. below).

The alternative of using the unmodified version of \mathbf{A} and finding admissible forces via a pseudo-inverse or least-square type optimization is computationally much more expensive and in practice not feasible for larger instances of the optimization problem. Thus, we only use the full-rank (i.e. modified) version of \mathbf{A} for computing the results shown below.

Discretized periodicity conditions

For finding optimal forces for a given shape and domain, the boundary conditions on facets of subdomain $\mathcal{D}_{h,i}$ have to be discretized. As we use a finite volume discretization scheme, the conditions on the values on $\partial\mathcal{D}_h$ can be discretized in a straightforward manner.

Definition 27. Let $\mathcal{D}_{h,i}$ be a finite volume subdomain. As described in section 4.1, each facet of F the subdomain $\mathcal{D}_{h,i}$ is of one four types. Let $\{e_i\}_i$ be the set of edges in F . Then, those types can be discretized as follows:

1. F is a facet \bar{F} of an adjacent subdomain $\mathcal{D}_{h,j}$. Let $\{\bar{e}_i\}_i$ be the set of edges in \bar{F} , numbered s.t. $e_k = \bar{e}_k$ for all $k \in \{0, \dots, |\{e_i\}_i|\}$. Then this type of boundary condition is discretized by identifying the edges e_k and \bar{e}_k , i.e. prescribing $\mathbf{f}(e_k) = \mathbf{f}(\bar{e}_k)$ for all k in the given index set.
2. F splits into two facets \bar{F}_1 and \bar{F}_2 (of equal length) of two adjacent subdomains \mathcal{D}_{h,j_1} and \mathcal{D}_{h,j_2} . Let $\{\bar{e}_i^1\}_i$ and $\{\bar{e}_i^2\}_i$ be the sets of edges in \mathcal{D}_{h,j_1} and \mathcal{D}_{h,j_2} , respectively, numbered s.t. $e_k = \bar{e}_k^1 \cup \bar{e}_k^2$ for all $k \in \{0, \dots, |\{e_i\}_i|\}$. Then this type of boundary condition is discretized by setting $\mathbf{f}(e_k) = \frac{1}{2}(\mathbf{f}(\bar{e}_k^1) + \mathbf{f}(\bar{e}_k^2))$.
3. F is the result of a splitting as given in 2. Then the forces on that facet are discretized as described above.

4. Composite materials and branching structures

4. F is a boundary facet. Then the forces are given by a force density

$$\frac{\int_F v \, dl}{\int_F dl} f.$$

These conditions have to be combined with the equations on stresses given in Chapter 4.2 to create the linear system $\mathbf{A}\mathbf{f} = \mathbf{b}$.

Phase field optimization

Given optimal forces across the domain \mathcal{D} and a non-optimal phase field v , an algorithm can be designed to successively improve the phase field towards a (local) minimum. In the method described here, an algorithm of Gauss-Seidel type is used, i.e. an algorithm that improves the phase field values on the discrete elements $T \in \mathcal{D}_{h,i}$ one by one for all subdomains $\mathcal{D}_{h,i}$, finding $\min_v \mathcal{J}[v]$.

4.2.1. The alternating algorithm

To solve the optimization problem, i.e. to find a (local) minimum of the energy an alternating algorithm is employed.

Algorithm 2: Alternating optimization algorithm

Data: Boundary data, initial values v_0 and f_0 , $\varepsilon > 0$

Result: A phase field v approximating the optimal shape for the given boundary data.

$f = f_0;$

$v = v_0;$

do

$v_l = v;$
 optimizeForces(v , f);
 optimizePhasefield(f , v);

while $\|v - v_l\| > \varepsilon;$

This algorithm alternates between optimizing the phase forces f and the phase field v , leaving the non-optimized quantity fixed. Based on the assumption that close to the optimum both forces and phase field change only very little in each iteration (because the current iterand only has a close-to-optimal energy), the change of the phase field is used as a measure of convergence.

Optimizing the deformations

To find the optimal forces (i.e. `optimizeForces(v, f)`) for an existing phase field, we solve the system of equations defined in (4.6) using a Cholesky solver. For the results

presented here the `CHOLMOD` [CDHR08] solver (which is part of the `Suitesparse` package), which provides an efficient parallel implementation of this type of solver, was used.

In this step, the rank deficiency of the force constraint matrix A has to be addressed. For a given set up, the set of constraints that have to be removed is fixed, so finding these constraints can be a pre-processing step and the respective constraints are then not added to the matrix \mathbf{A} when it is built. Thus, this step only requires a negligible amount of computing performance.

Optimizing the phase field

The implementation of the function `optimizePhasefield(f, v)`, i. e. the function finding the optimal phase field for existing forces is realized by a Gauss-Seidel type iteration that optimizes the values of single cells one by one and iterates that procedure.

Let us consider the discretized version of the energy $\mathcal{J}[v]$, that was given in (4.4)

$$\begin{aligned} \mathbf{J}[V] &:= \min_{\tau \in \Sigma_{\text{ad}}} \sum_T \mathbf{J}_T[V] \text{ with} \\ \mathbf{J}_T[V] &= \frac{|\sigma(T)|^2}{V(T)} + \nu V(T) + \frac{\beta}{\varepsilon} \frac{32}{\pi^2} (V(T) - \delta)(1 - V(T)) \\ &\quad + \frac{\beta \varepsilon}{4} \sum_{i=1}^4 \frac{(V(T) - V(T^{(i)}))^2}{h^2}. \end{aligned}$$

$T^{(i)}$ denotes the cell adjacent to T across the edge e_i and h the mesh width (the length of an edge in the uniform mesh). To find a minimum of $\mathbf{J}[V]$ for the phase field $V(T)$ on an element T for a fixed phase field $V(T^{(i)})$ on the neighbor cells, we apply Newton's method. A rescaling is used to overcome difficulties due to the singularity at $v(T) = 0$, namely, we compute the minimum of the rescaled function using $V(T) \mapsto \mathbf{J}_T(e^{-V})$.

To ensure a good performance of Newton's method, it is important to choose a suitable initialization of χ . Consider the local terms of the cost functional (dropping the non-local last perimeter term):

$$\mathbf{J}_T^{\text{loc}}[V] = \frac{|\sigma|^2}{V} + \nu V + \frac{\beta}{\varepsilon} \frac{32}{\pi^2} (V - \delta)(1 - V). \quad (4.7)$$

We note that the function can have no more than two minima: For $|\sigma| \ll 1$, $|\sigma|/\chi$ is the dominant term only close to 0, creating a minimum at $\chi \ll 1$. For other values of σ , the only minimum is at $\chi = 1$.

To find the location of the second potential minimum, we compute the derivative of (4.7):

$$\partial_V \mathbf{J}_T^{\text{loc}}[V] = \nu - \frac{|\sigma|^2}{V^2} + \frac{\beta}{\varepsilon} \frac{32}{\pi^2} (1 - 2V + \delta).$$

Assuming the minimum is not located at $V = 1$, we compute

$$V^2 = \frac{|\sigma|^2}{\nu} + \frac{\beta}{\varepsilon} \frac{32}{\pi^2} (1 + \delta) =: V_c.$$

4. Composite materials and branching structures

To initialize the phase field, we can compare the two minima and choose a value depending on which one is the global minimum.

$$V_{\text{initial}} = \begin{cases} \mathbf{J}_T^{\text{loc}}[V_c] & \text{if } \mathbf{J}_T^{\text{loc}}[V_c] \leq \mathbf{J}_T^{\text{loc}}[1] \\ 1 & \text{else.} \end{cases}$$

Assuming $v \leq 1$ and $\delta \ll 1$, we can then approximate the positions of the minima of $\mathbf{J}_C(v)$ with 1 and $V_c := |\sigma| \sqrt{\frac{\pi^2 \epsilon}{32 \beta}}$. We note, that $\mathbf{J}_C(V_c) \leq \mathbf{J}_C(1)$ if $|\sigma| \lesssim \frac{\beta}{2} \sqrt{\frac{\pi^2 \epsilon}{32 \beta}} =: \hat{\sigma}$. Thus, we initialize the phase field using

$$V_{\text{initial}} = \begin{cases} V_c & \text{if } |\sigma| \leq \hat{\sigma} \\ 1 & \text{else.} \end{cases} \quad (4.8)$$

In the approximations used above, we neglected some (presumably small) terms of $\mathbf{J}_C(v)$. As V_{initial} is used only as an initialization for Newton's method, the introduced inaccuracies have no influence on the resulting optimized phase field.

Starting from the second iteration of the alternating descent algorithm, the phase field can also be initialized using the result of the last phase field optimization. However, this approach is prone to becoming stuck in local minima. On the other hand, reinitializing the phase field between iterations of the alternating descent algorithm introduces the possibility of increasing energies in the phase field optimization step, but — in the applications discussed here — did not lead to a non-convergent algorithm overall. For all results presented in this chapter, the simplified initialization (4.8) was used to initialize Newton's method in every phase field optimization step.

Algorithm 3 summarizes the complete algorithm, that was used to optimize the phase field V for given forces \mathbf{f} . This completes the set of algorithms necessary to implement Algorithm 2.

Parallelization

Each step of Algorithm 2 can be computed in parallel over all subdomains: The phase field optimization does (by definition of the model) not depend on neighboring subdomains and can thus be started concurrently on all subdomains. The solution of the system of equations in `optimizeForces` is parallelized by the implementation of Cholesky's method in `Suitesparse`. The straightforward distribution of subdomains to processes yields a close-to-optimal speedup factor.

4.3. Results

The results in this section are computed on a quadratic domain $\mathcal{D} \subseteq [0, 1]^2$, composed of several quadratic subdomains with different periodicity conditions. The center of the domain was always filled with periodic subdomains, around which a varying number of branching periodic and coupling subdomains were placed.

Algorithm 3: Gauss-Seidel algorithm to optimize the phase field

Data: Initial values V_{init} , forces \mathbf{f} , desired tolerance tol

Result: An approximation of the required tolerance tol of an optimal structure given as a discrete phase field V

```

 $V_{\text{diff}} = \infty;$ 
while  $V_{\text{diff}} > \text{tol}$  do
   $V_{\text{last}} = V;$ 
  for  $T \in \tau$  do
     $V|_T = 1;$ 
    if  $\partial_v \mathbf{J}_T[1] \geq 0$  then
      Find  $\arg \min_x \mathbf{J}_T[x]$  using Newton's method;
      if  $x \in [\delta, 1]$  then
         $V|_T = x;$ 
      else
        if  $x < \delta$  then
           $V|_T = \delta;$ 
        else
           $V|_T = 1;$ 
        end
      end
    end
  end
   $V_{\text{diff}} = \|V - V_{\text{last}}\|;$ 
end

```

4. Composite materials and branching structures

4.3.1. A simple example

First, a simple example for a decomposition of a rectangular domain into quadratic subdomains is considered. Figure 4.4 illustrates this kind of domain. All subdomains are of equal size, the colors indicate the different reference subdomains: The blue subdomains in the middle are top-bottom and left-right periodic, the light blue subdomains are periodic parallel to the boundary and have a branching condition in the perpendicular direction, the green subdomains at the corners have branching boundary conditions regarding their left-right and top-bottom boundaries and the light green subdomains couple the light blue and green subdomains to allow force transfer from the edge to the center of the domain. These subdomains are required, as diagonal forces could only be transmitted through the single point that is in the cut of blue and green subdomains, which is impossible in our model. Forces are applied to all boundaries at certain parts which model an incoming load that may be derived from a branching type structure.

4.3.2. Symmetry assumptions

The “simple example” assumes symmetries along axes through the middle of the domain parallel to its coordinate axes. This assumption is not true for optimal structures with respect to general loads. Optimizing shapes for a load for which the optimal shape does not show these symmetries (e. g. shear loads), leads to a shape that shows some clearly non-optimal structure. This is not a problem of the algorithm (which finds the best shape possible in a given model), but an indication that the wrong domain decomposition, i. e. the wrong model was chosen for this particular set up.

To find a more plausible shape, the types of subdomains used have to be adapted: Instead of assuming the “coupling subdomains” on each side of the periodic subdomains on the outer strips are symmetric, two different coupling subdomains per layer can be used (s. Figure 4.4). This composition of subdomains allows for a break of symmetry and thus a larger set of admissible shapes, in which the optimum no longer shows implausible structures like mechanically useless kinks or edges.

This observation leads to the challenge of finding the minimal number of different subdomains for a given scenario, for which the optimal structure is “plausible”. A larger number of subdomains can always be utilized, but two different reference subdomains admitting the same optimal structure is proof of wasted computational resources as a model using the same reference subdomain instead would have been more efficient and would have yielded the same result.

4.3.3. Additional layers

The next logical step is to add more layers of subdomains towards the boundary to the model described in Section 4.3.1, thus creating domains that consist of a central periodic region and two or three boundary layers. On these domains, the forces above

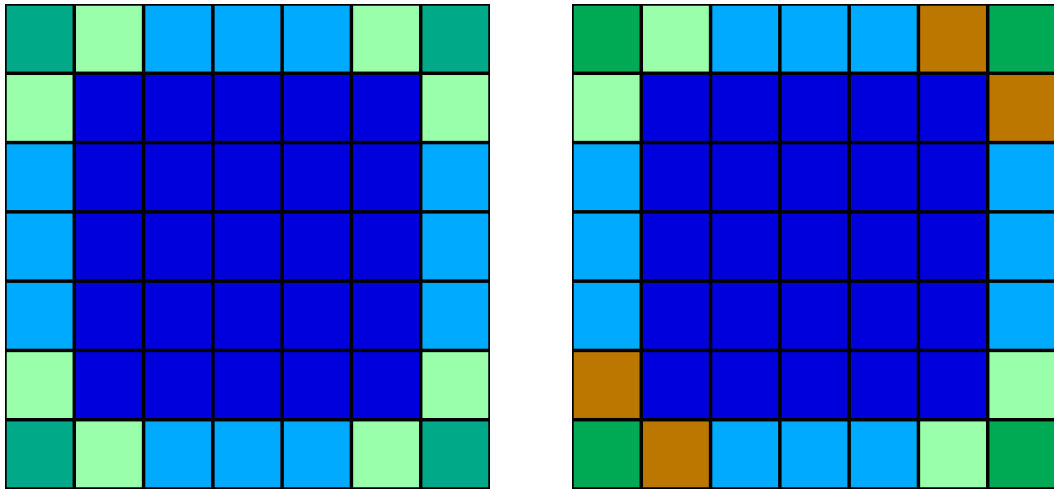


Figure 4.4.: Decomposition of a quadratic domain into quadratic reference subdomains of four (left) and five (right) different types.

are applied. Figure 4.5 depicts these domains. Again, different colors indicate different reference subdomains.

To allow non-symmetric structures, there are two types of coupling (reference) subdomains in each layer. For the layers with more than one coupling subdomain per edge and corner, only one of these reference subdomains is allowed to be non-symmetric, as numerical experiments showed, that optimizations using more non-symmetric subdomains did not produce meaningfully different results.

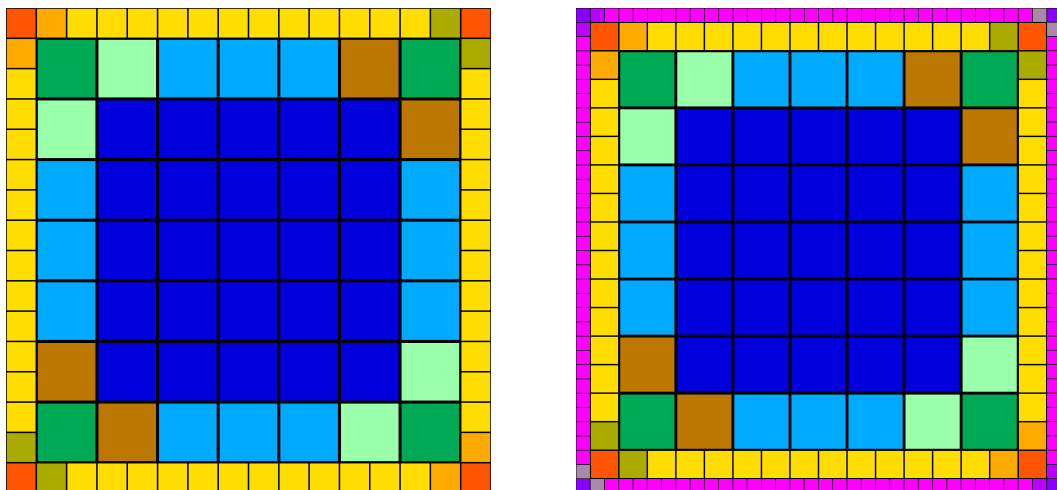


Figure 4.5.: Decomposition of a quadratic domain into nine and thirteen different types

4. Composite materials and branching structures

4.3.4. Results

To test the model, compression and shear loads were applied to the domain types discussed above.

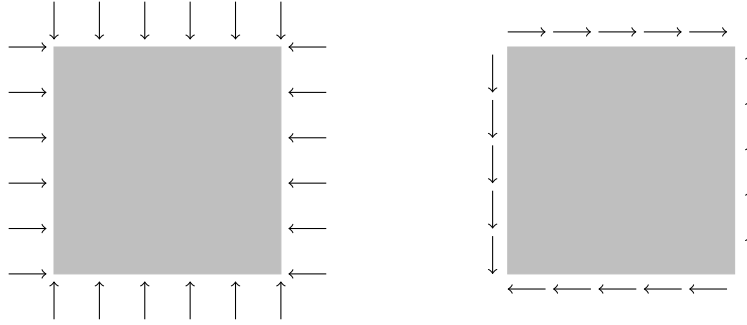


Figure 4.6.: Types of applied loads: Compression (left) and shear (right)

For all domain types, the subdomains were discretized using $M \times N$ cells using values $M = 200$ and $N = 200$. On each cell of the outer layer, forces were applied on the intervals $[\frac{2}{6}M, \frac{3}{6}M] \times \{l_2\}$, $[\frac{4}{6}M, \frac{5}{6}M] \times \{l_2\}$ and $\{l_1\} \times [\frac{2}{6}N, \frac{3}{6}N]$, $\{l_1\} \times [\frac{4}{6}N, \frac{5}{6}N]$ on horizontal and vertical boundaries ($l_1, l_2 \in \{0, 1\}$), respectively, to simulate a setup that promotes the creation of branching type structures in the computational domain $\mathcal{D}_{h,\text{comp}}$. The directions of these forces are depicted in Figure 4.6 for the compression and shear scenario.

Compression loads

For the pressure load given in Figure 4.6, optimal shapes were computed on the domains consisting of five, nine and thirteen different reference subdomains. Trying to optimize shapes for the compression load setup on a four-subdomain setup already results in implausible structures: The enforced symmetry prevents the algorithm from allowing a slight difference in the coupling subdomains to compensate for the non-symmetrical structures in the branching subdomains — especially when the algorithm has not reached the optimal shape yet. A comparison of the optimal shape for four and five reference subdomains can be found in Figure 4.7. In all setups, pillar-like structures support the load on the boundary through branching structures and transfer this load to a mesh-like structure in the center of the domain. The corner and coupling subdomains connect the branching periodic pillars and minimize the loads appearing in parallel to the boundary. The nine and thirteen subdomain setups (s. Figure 4.8 and Figure 4.9, respectively), extend the structures visible in the five reference subdomain setup without introducing fundamental changes, which indicates that the model used is suitable for approximate branching structures that support the applied loads.

When using higher numbers of reference subdomains, the limits of the optimization algorithm become apparent: At certain points in the domain — the points where the top

left coupling subdomain and the inner corner subdomain connect — structural artifacts (s. magnification) appear that can be explained by a difference in thickness between the two coupling structures. While these structures clearly are non-optimal, the algorithm fails to optimize the structure any further, oscillating at changes of order 10^{-10} for the nine subdomain setup and 10^{-9} for the thirteen subdomain setup. More exact solution cannot be expected for the thirteen subdomain type setup, as the system of equations defining the forces can only be solved with an accuracy of order 10^{-8} for some of the forces that are only implicitly defined by linear dependencies (cf. Section 4.2).

Shear loads

Shear loads (as given in Fig. 4.6) were applied on the domains consisting of five, nine and thirteen reference subdomains. A symmetry break again already occurred on the four-subdomain setup (s. Fig. 4.10) and had to be circumvented by introducing an additional reference subdomain. This necessity can be explained by noting that the structures in the center and branching periodic subdomains are not symmetric (contrary to the compression scenario), making a non-symmetric coupling subdomain optimal, which cannot be modeled by a single, mirrored reference subdomain.

Again, the forces are transferred to the center of the domain by branching type structures. The corner and coupling subdomains show a larger tendency towards minimizing deformations by forces in parallel to the boundary. As there are no forces in the perpendicular direction, no structures to support them are present.

The results for nine (Figure 4.11) and thirteen reference subdomains (Figure 4.12) extend the result for five reference subdomains in a compatible manner. The coupling subdomains on both ends of the branching boundary become more similar but using the same reference subdomain for both still results in an implausible structure due to inadmissible symmetry assumptions.

Contrary to the compression scenario, the alternating algorithm optimizes the shear scenario more accurately (most likely because the forces can be determined with higher accuracy).

4.4. Conclusion

We developed a shape optimization model for domains composed of subdomains of various types and extended an alternating descent algorithm to optimize shapes on that domain under different load configurations. The algorithm is capable of optimizing shapes on domains composed of an arbitrary number of reference subdomains, however numerical stability suffers when the proposed method of regularizing the force constraint matrix is applied. Therefore another method of finding the optimal forces could be developed, to allow for a more reliable energy minimization in some scenarios.

Furthermore, the ratio of width and height of the subdomains in each layer could be optimized as well, to allow for a larger set of different structures to be considered. This has

4. *Composite materials and branching structures*

been described for one subdomain in [Lüt16], but would be computationally challenging if applied on the scenario described in this thesis without modification.

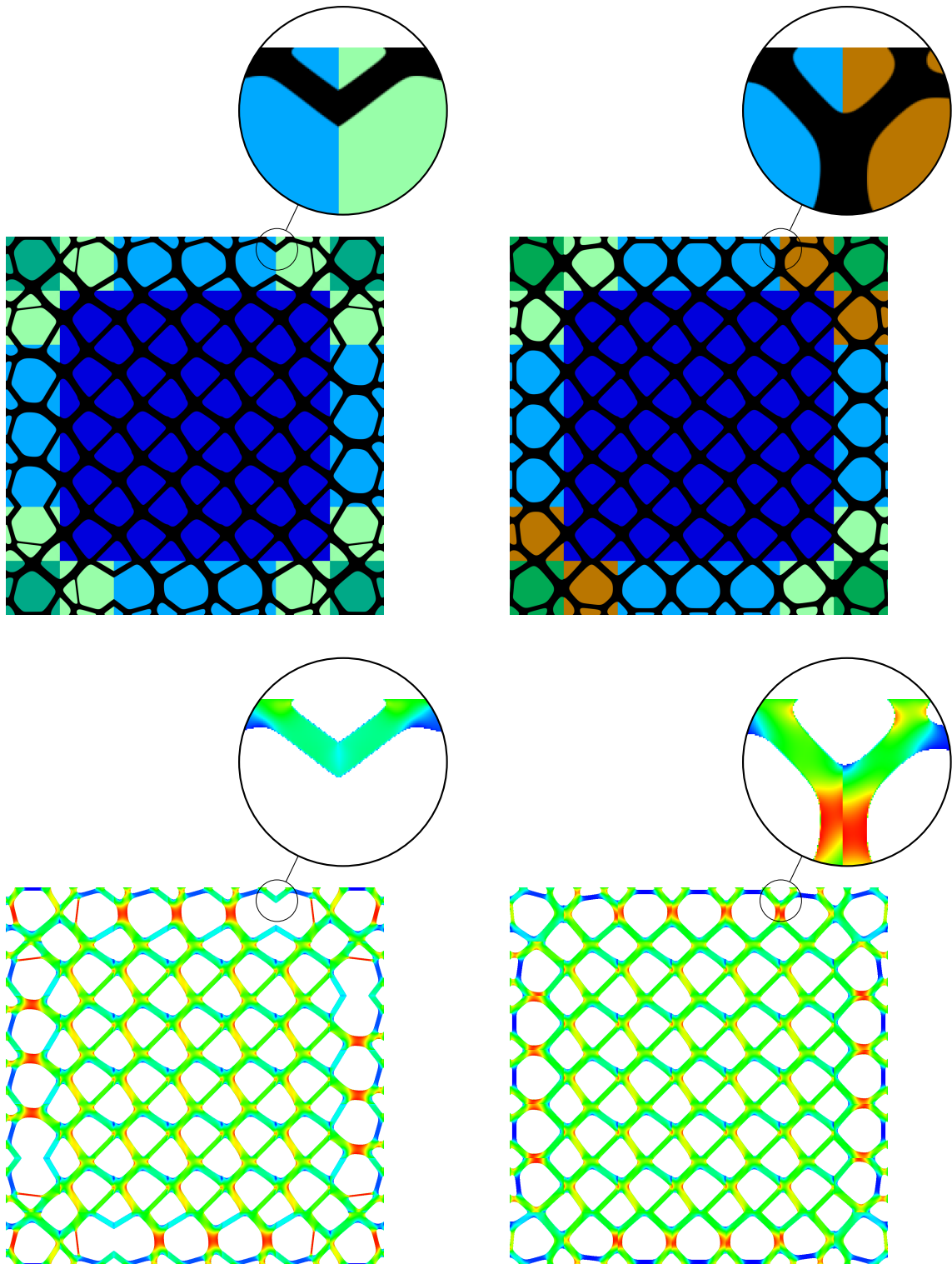



Figure 4.7.: Optimal shape (top) and von Mises stresses (bottom) for compression loads using four reference subdomains and non-optimal structure caused by inadmissibly assumed symmetry (left) compared to the optimal shape for shear loads using five reference subdomains (right). The von Mises stresses are color-coded using the colorbar  on the set $[V > 0.5]$.

4. Composite materials and branching structures

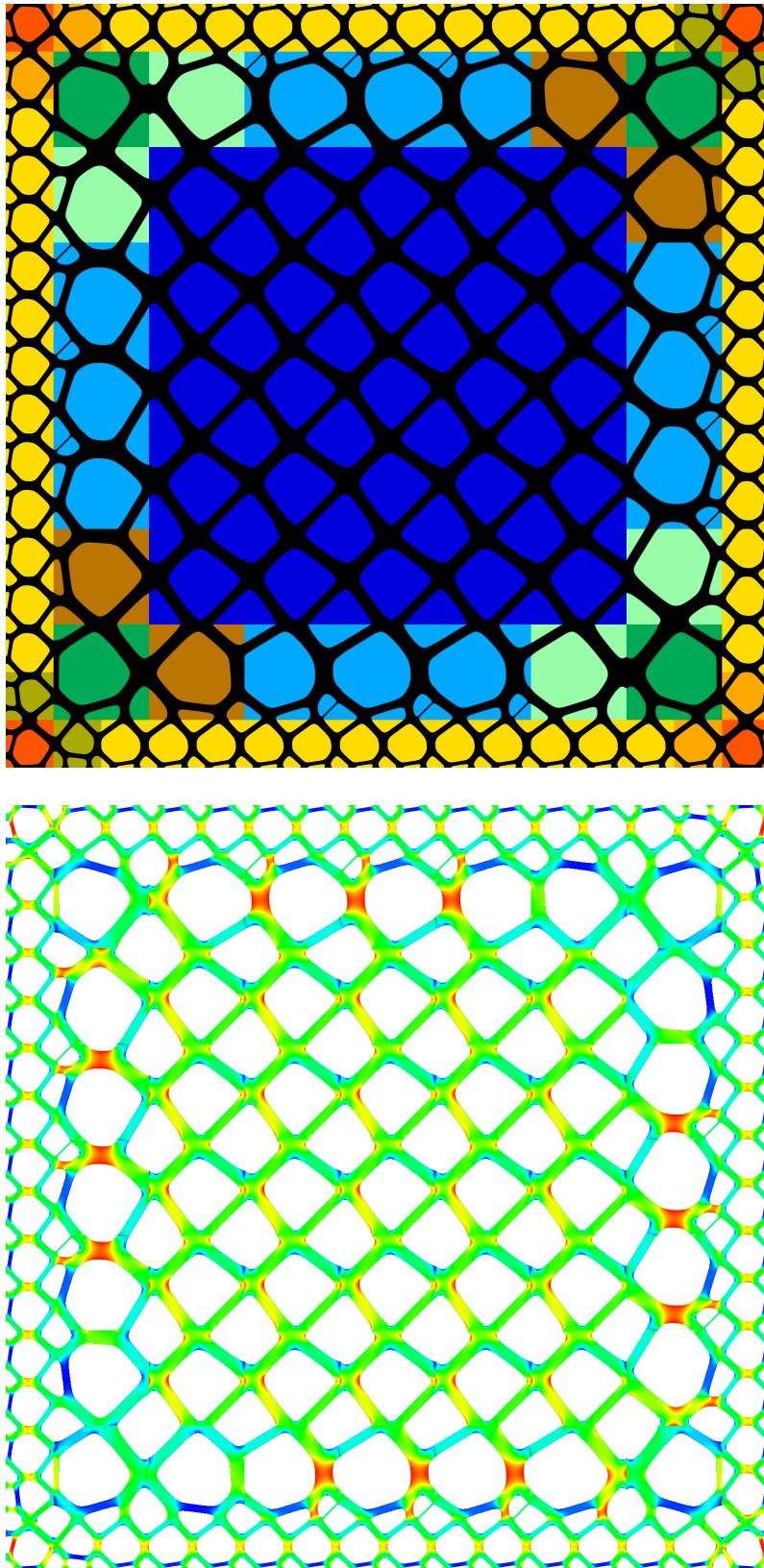


Figure 4.8.: Compression result for nine reference subdomains (top) and von Mises stresses color-coded using the colorbar  on the set $[V > 0.5]$ (bottom).

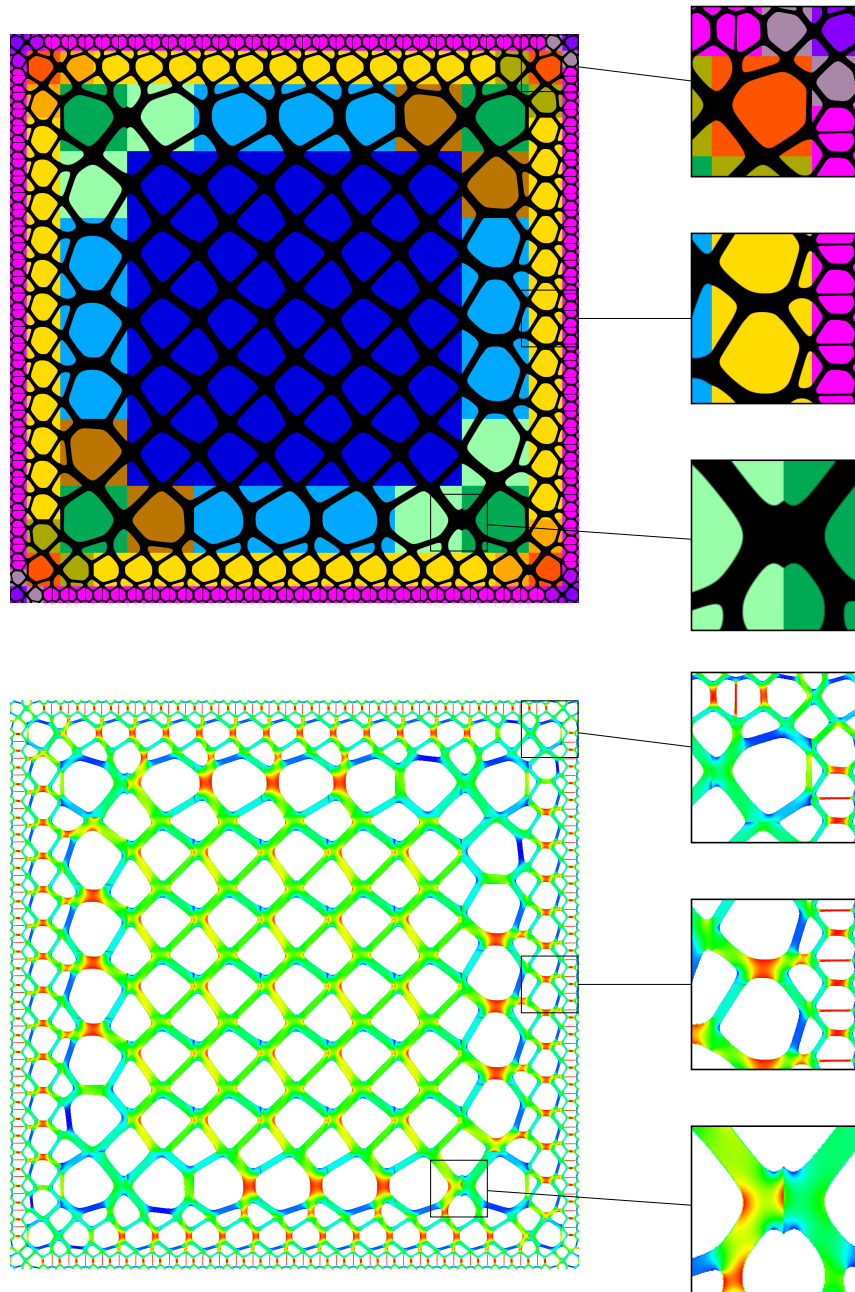



Figure 4.9.: The optimal shape for the compression load case and a setup using thirteen reference subdomains is depicted (top) and von Mises stresses using the colorbar  on the set $[V > 0.5]$ (bottom).

4. Composite materials and branching structures

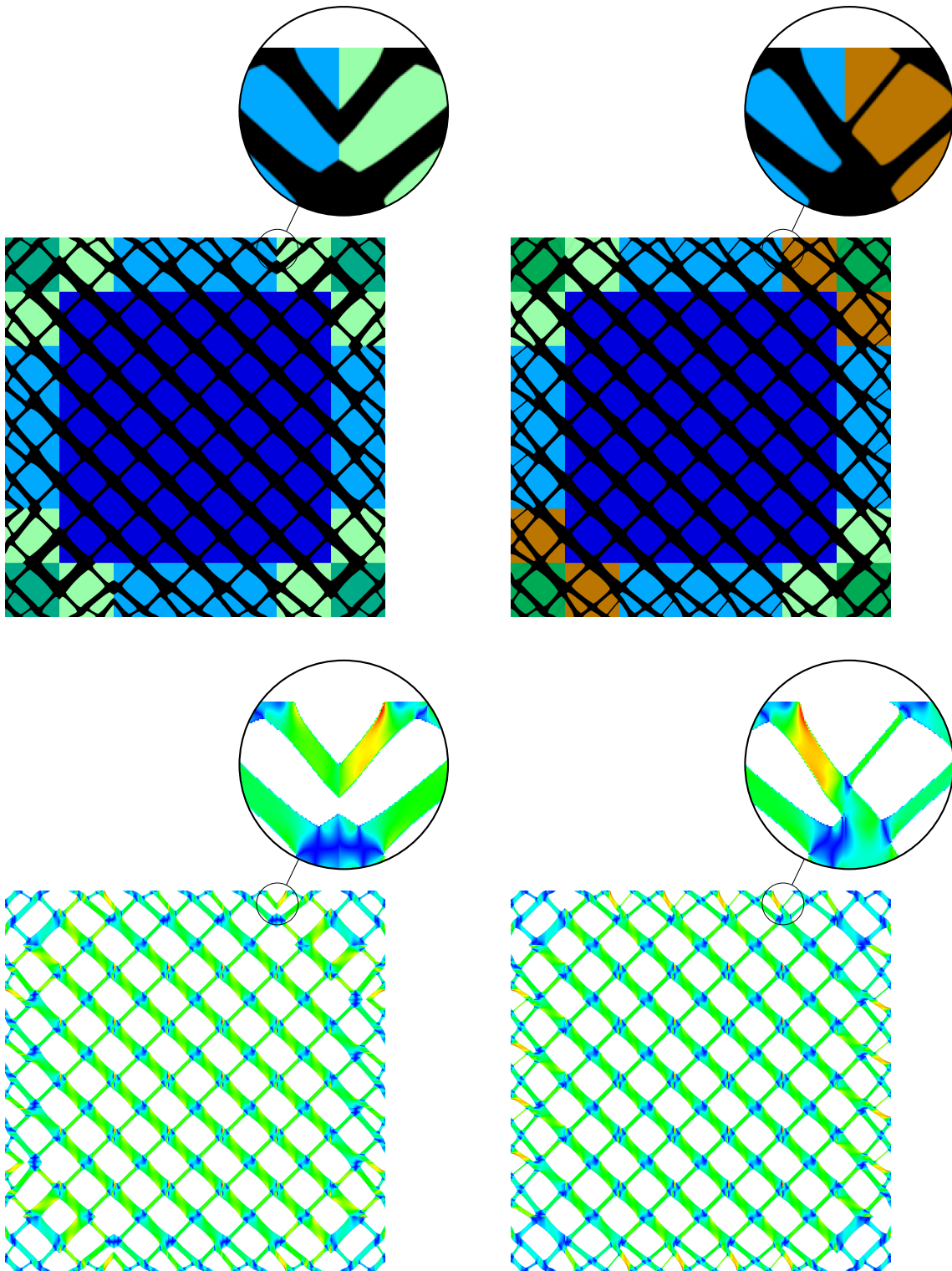
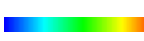


Figure 4.10.: Optimal shape for shear loads using four reference subdomains and non-optimal structure caused by inadmissibly assumed symmetry (left) compared to the optimal shape for shear loads using five reference subdomains (right). Top row: optimal structures, bottom row: von Mises stresses encoded using the colorbar  on the sets where $[V > 0.5]$.

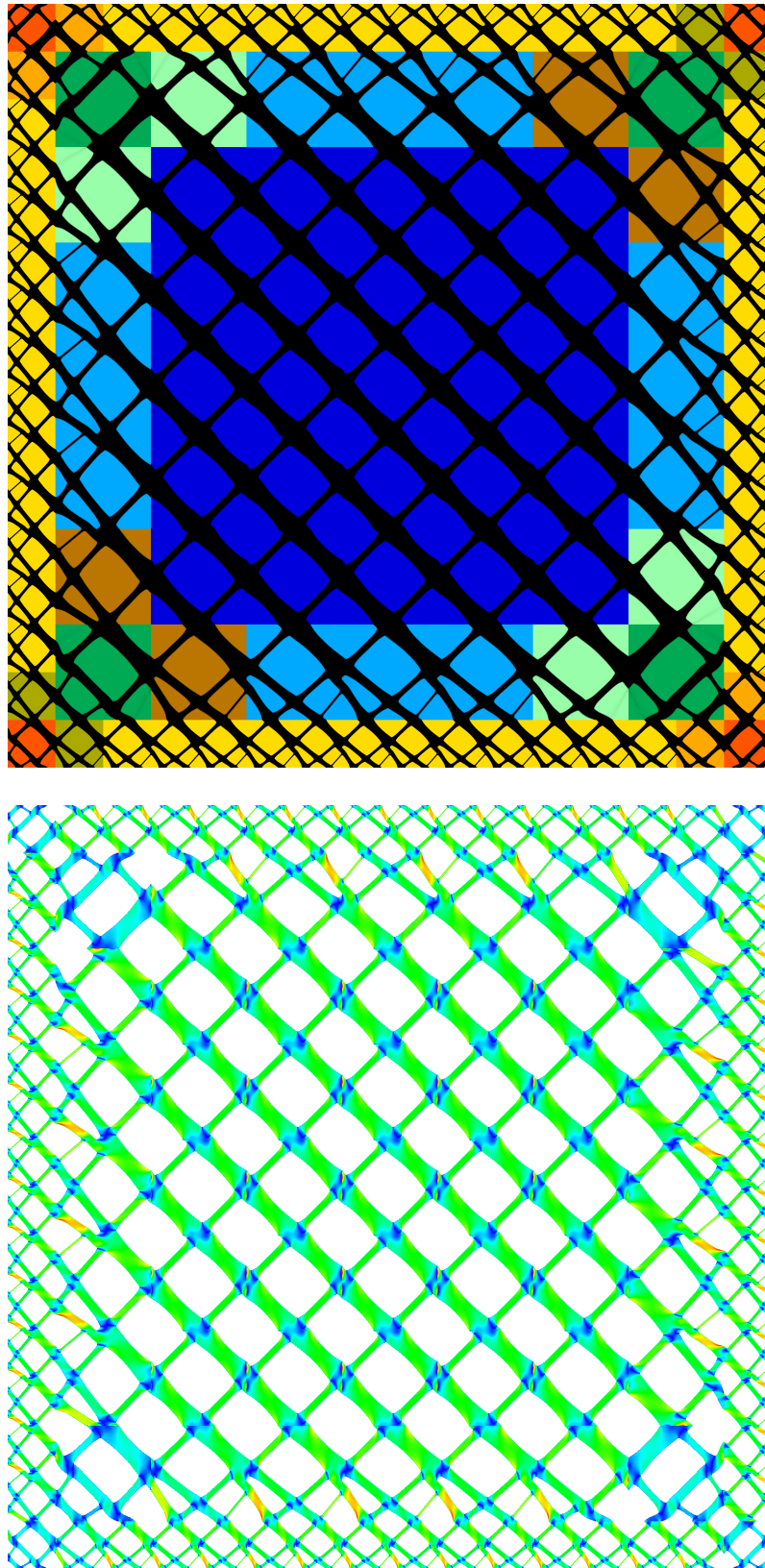


Figure 4.11.: Optimal structure for shear loads using nine reference subdomains (top) and von Mises stresses color-coded using the colorbar $[V > 0.5]$ (bottom).

4. Composite materials and branching structures

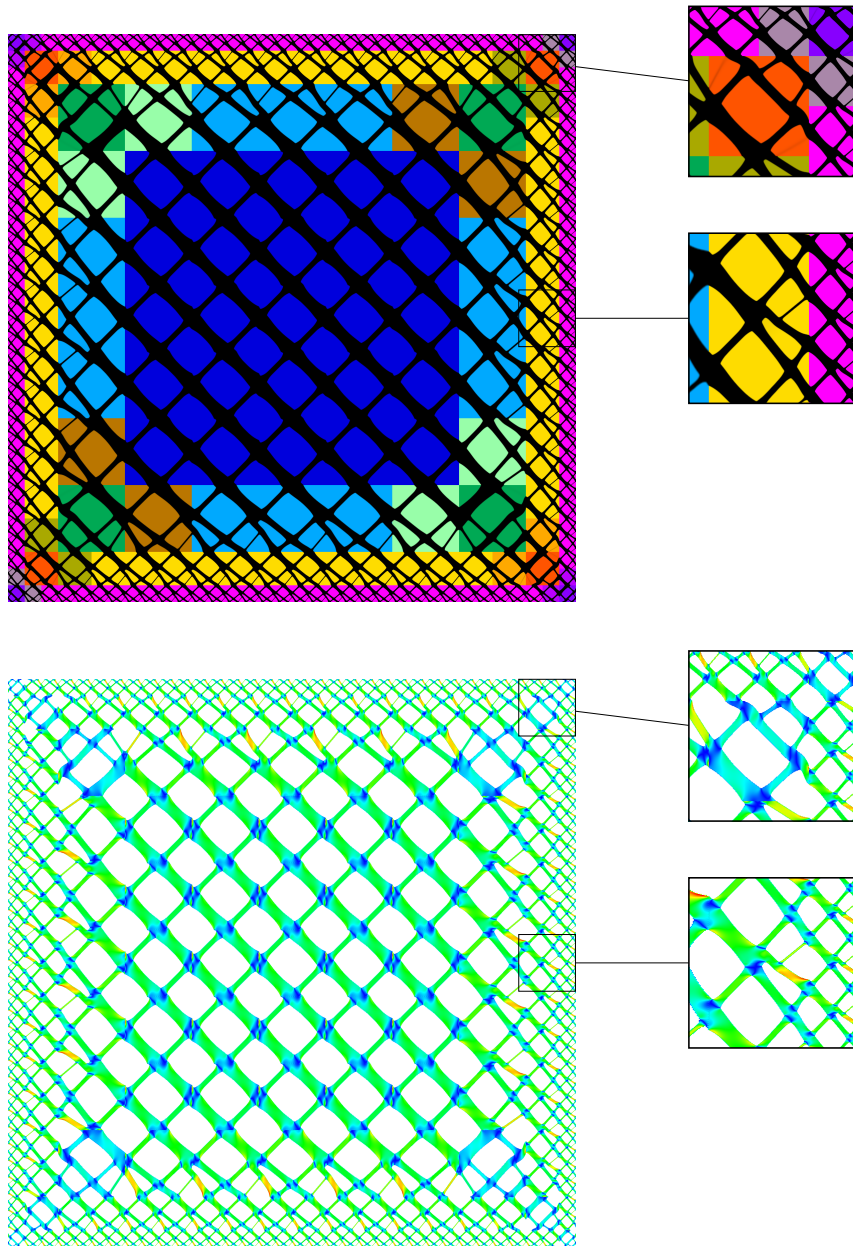



Figure 4.12.: The optimal shape (top) and von Mises stresses (bottom) for the shear load case and the same setup as in Fig. 4.9 is displayed with two regions being magnified on the right. Again together with the optimal shape (top) the associated von Mises stresses are rendered (bottom) and colorcoded using the colorbar  on the set $[V > 0.5]$.

5. Fine-scale elastic shape optimization

In this chapter, we will explore a model that does not avoid the formation of microstructure in the optimization by using regularization, but uses a *fine-scale* approach to explicitly model the microstructure on a separate *micro-scale*. It has a defined and fixed factor of length and volume between this micro-scale and the macroscopic domain \mathcal{D} , also denoted as the *macro-scale*. For this reason, we call this model fine-scale, as opposed to *two-scale* models, where the scaling factor tends to infinity (and thus the micro-scale is arbitrarily small in comparison to the macro-scale).

From [All02] we know that for a two-scale elastic shape optimization problem, solutions admit an arbitrarily fine *laminate* of at most rank d , where d is the spatial dimension, on the micro-scale. In the model described there, the factor between macro and micro-scale is not fixed, but the micro-scale is arbitrarily smaller in an appropriate sense.

Multiscale materials have been studied in many contexts, analytically and numerically. Starting with Hashin [Has62] in 1962, notable contributions include Grabovsky and Kohn [GK95], Tartar et. al. [Tar85, MT85] and Allaire et. al. [All02, AJ05, AD14, AD15]. Numerical methods for optimizing this kind of material have been described in [BT10a, BT10b, BT14, CGRS14, CGLR17]. A useful method for numerical simulation of such materials is the method of Heterogeneous Multiscale Elements (HMM) [EE03, EE05, EEH03, EMZ05]. This method models fine-scale materials by inserting a micro-scale cell at each quadrature point. It has found applications for a variety of numerical problem, not just fine-scale elasticity. It has been used e. g. in [Ohl05] in the context of an advection-diffusion problem, in [AG11] for the wave equation and in [HOV16] for the time-harmonic Maxwell's equation.

As mentioned in previous chapters, in the context described here, *homogenization* is an often used concept: The micro-scale properties are transformed into an effective macroscopic behavior, i. e. a locally homogeneous macroscopic material, that behaves like the multiscale material on the macro-scale, transforming a tensor $C(y)$, that depends on the fine-scale, into an effective one-scale tensor C^* . For a more formal introduction to that concept cf. [All02, Chapter 1].

In the context of elastic shape optimization, design parameters on the micro-scale have usually been restricted to low dimensional representations of certain sets of structures, e. g. ellipsoidal holes [CGRS14]. To the best of our knowledge, there is no prior work on a full dimensional modeling of possible shapes on the micro-scale, neither using phase fields nor similar methods.

5.1. Elasticity of a fine-scale material

In this section, we will define the elastic fine-scale material and describe, how it will be used to find a solution for a fine-scale elastic shape optimization problem.

Consider an elastic body composed of a material which properties are defined by a microstructure. This microstructure consists of two materials: One hard (full) material and a second much softer material. These two materials can be combined to form arbitrary structures.

Let $\mathcal{D} \subset \mathbb{R}^d$ denote the object domain with Dirichlet boundary conditions on a set $\Gamma_D \subset \partial\mathcal{D}$ and Neumann boundary conditions on a set $\Gamma_N \subset \partial\mathcal{D}$. On Γ_D the object is fixed and on Γ_N boundary forces are applied. Elastic deformations will be described by $\phi = \text{id} + u$, where $u = u(x)$ is called the displacement of each point $x \in \mathcal{D}$, as introduced in Chapter 2. Furthermore, define the *microscopic cell* $\mathcal{C} = [0, 1]^2$, which will be used to model periodic microscopic structures at each point of the macroscopic domain \mathcal{D} .

Let C be an elasticity tensor (that will be defined in more detail below) and define boundary forces $g \in L^2(\Gamma_N, \mathbb{R}^d)$ on $\Gamma_N \subset \partial\mathcal{D}$. As mentioned, let $\Gamma_D \subset \partial\mathcal{D}$ denote the part of the boundary where Dirichlet boundary conditions enforce $\bar{u}(x) = 0$, define the space enforcing these boundary conditions as $W_{\Gamma_D}^{1,2}(\mathcal{D}) := \{u \in W^{1,2} : u|_{\Gamma_D}(\mathcal{D}) = 0 \text{ in the sense of traces}\}$ and define the fine-scale elastic displacement as $u(x, y) = \bar{u}(x) + \tilde{u}(x, y)$, where $\bar{u} \in W_{\Gamma_D}^{1,2}(\mathcal{D})$ denotes the macroscopic component and $\tilde{u}(x, \cdot) \in W_{\text{per}}^{1,2}(\mathcal{C})$ for $x \in \mathcal{D}$ and denotes the microscopic periodic part. The space

$$W_{\text{per}}^{1,2}(\mathcal{C}) =: \{\tilde{u} \in W^{1,2} : \tilde{u} \text{ periodic on } \mathcal{C}\}$$

consists of all functions on \mathcal{C} that are suitable to model an infinitely repeating periodic mesh of shapes.

The microscopic component is coupled to the macroscopic component via the displacements — or equivalently stresses — at every macroscopic point x , which are transformed to an affine displacement on the microscale, which induces these stresses uniformly on the microscopic cell. Figure 5.1 sketches this coupling and these affine displacements inducing the three pure stresses in two dimensions. For the fine-scale model, we obtain an affine-periodic setting in which the affine component is represented by the macroscale while the periodic component represents the microscopic structures.

Using the fine-scale displacement, we can define fine-scale energies

$$\begin{aligned} \mathcal{W}[v, u] &:= \frac{1}{2} \int_{\mathcal{D}} \int_{\mathcal{C}} C(x, y) \epsilon[\bar{u}(x) + \tilde{u}(x, y)] : \epsilon[\bar{u}(x) + \tilde{u}(x, y)] \, dy \, dx, \\ \ell[u] &:= \int_{\Gamma_N} g(x) \cdot \bar{u}(x) \, da. \end{aligned}$$

The energy $\mathcal{W}[v, u]$ is the fine-scale equivalent of the bilinear form introduced in Theorem 12. The *strain tensor* is defined as $\epsilon[u] = \frac{Du + Du^t}{2}$. The corresponding elastic energy as is defined as

$$\mathcal{E}[v, u] = \mathcal{W}[v, u] - \ell[u],$$

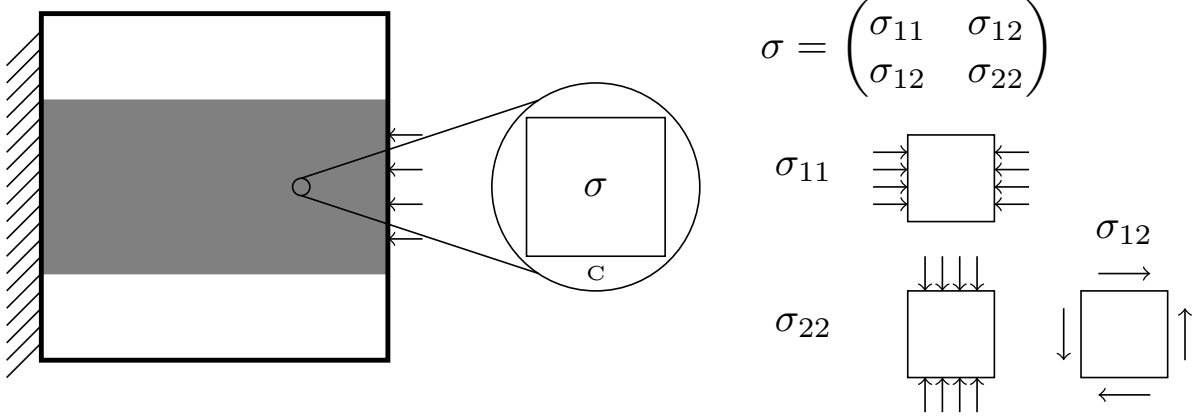


Figure 5.1.: Displacements on the macroscale are translated into affine displacements on the microscale. Sample fine-scale configuration (left) and displacements resulting in the pure stresses on a periodic cell for the three degrees of freedom in a two-dimensional elasticity tensor.

The micro-scale is here again defined via an elastic problem. The material parameters (and thus the elastic tensor C on the micro-scale) are given by a phase field $v : \mathcal{D} \rightarrow \mathbb{R}$ using -1 and 1 as the pure phases. Let C_{LN} be a Lamé–Navier type elastic tensor (as introduced in (2.4)), $\chi(v) = \frac{1}{4}(v+1)^2$ and $\delta \ll 1$. Then for fixed x

$$C(x, y) := ((1 - \delta)\chi(v(y)) + \delta)C_{LN}$$

defines the elastic tensor C at position y and a smooth transition between a hard and a soft material.

As mentioned above, homogenization is a technique that transfers the properties of multiscale material onto a macroscopic property, in this case, an elasticity tensor. The fine-scale formulation of the limit problem is

$$\int_{\mathcal{D}} \int_{\mathcal{C}} \frac{1}{2} C(x, y) (\epsilon[\bar{u}](x) + \epsilon[\tilde{u}](x, y)) : (\epsilon[\phi](x) + \epsilon[\psi](x, y)) \, dy \, dx = \int_{\Gamma_N} g(x) \cdot \phi(x) \, da.$$

Note, that there is now a microscopic test function ψ alongside with the macroscopic test function ϕ .

Let $R[u] := \bar{u}(x) + \tilde{u}(x, y)$ for $u \in W_{\Gamma_D}^{1,2}$ and \tilde{u} solving the correction problem

$$\int_{\mathcal{C}} \frac{1}{2} C(x, y) (\epsilon[\bar{u}](x) + \epsilon[\tilde{u}](x, y)) : \epsilon[\psi](x, y) = 0$$

for all $\psi \in W_{\text{per}}^{1,2}(\mathcal{C})$. Then, an effective tensor C^* can also be defined variationally as

$$\frac{1}{2} C^*(x) \epsilon[\bar{u}](x) : \epsilon[\bar{u}](x) = \int_{\mathcal{C}} \frac{1}{2} C(x, y) \epsilon[R[u]](x, y) : \epsilon[R[u]](x, y) \, dy. \quad (5.1)$$

5. Fine-scale elastic shape optimization

Symmetry assumptions on C^* lead to the equations

$$C_{ijkl}^* = C^* \epsilon_{ij} : \epsilon_{kl} = C^* \epsilon_{ij+kl} : \epsilon_{ij+kl} - C^* \epsilon_{ij-kl} : \epsilon_{ij-kl}, \quad (5.2)$$

where $\epsilon_{ij} = \frac{1}{2}(e_i \otimes e_j + e_j \otimes e_i)$ and $\epsilon_{ij+kl} = \frac{1}{2}(\epsilon_{ij} + \epsilon_{kl})$, $\epsilon_{ij-kl} = \frac{1}{2}(\epsilon_{ij} - \epsilon_{kl})$.

5.2. Shape optimization

With the methods described in Chapter 5.1 it is possible to compute the macroscopic (equilibrium) displacement $\bar{u}[v]$ from the microscopic shape parameters v . Let $\mathcal{J}[v, u[v]]$ be a cost functional, that can depend on the fine-scale displacement u as well as the microscopic parameters v . As introduced in Chapter 2, shape optimization asks for an optimal shape w. r. t. $\mathcal{J}[v, u[v]]$, i. e. a shape that minimizes $\mathcal{J}[v, u[v]]$, described via a macroscopic parametrization of the microscopic parameter v .

5.2.1. Deterministic fine-scale shape optimization

The optimization of the fine-scale energies follows the same principles as optimization of a one-scale elastic shape optimization problem. There are two methods to find such an optimal shape: The first is minimizing $\mathcal{J}[v, u[v]]$ — where $u[v]$ is the equilibrium displacement induced by v — and making use of a dual problem to introduce the relation between u and the elastic minimization problem and evaluating the micro-scale when needed in the energies $\mathcal{J}[v, u[v]]$ and $\mathcal{E}[v, u[v]]$. The second method is minimizing the Lagrangian

$$\mathcal{L}[v, u, p] = \mathcal{J} - \partial_u \mathcal{E}(p),$$

calculating the optimal shape and equilibrium displacement in parallel.

Let us first consider the approach of minimizing $\mathcal{J}[v, u[v]]$ using a dual problem. We need to define a deterministic target functional, that will be minimized in order to find the optimal shape. In analogy to the one-scale functional, define volume and interface terms as

$$\begin{aligned} \mathcal{V}^\varepsilon[v] &:= \int_{\mathcal{D}} \int_{\mathcal{C}} \chi(v(x, y)) \, dy \, dx, \\ \mathcal{L}^\varepsilon[v] &:= \int_{\mathcal{D}} \int_{\mathcal{C}} \frac{1}{2} \varepsilon |\nabla v(x, y)|^2 + \frac{1}{\varepsilon} \psi(v(x, y)) \, dx. \end{aligned}$$

The fine-scale target functional takes the form

$$\begin{aligned}
 \mathcal{J}[v, u[v]] &= 2\mathcal{W}[v, u[v]] + \nu\mathcal{V}^\varepsilon[v] + \beta\mathcal{L}^\varepsilon[v] \\
 &= \int_{\mathcal{D}} \int_{\mathcal{C}} C(x, y) \epsilon[\bar{u}[v](x) + \tilde{u}[v](x, y)] : \epsilon[\bar{u}[v](x) + \tilde{u}[v](x, y)] \, dy \, dx \\
 &\quad + \nu \int_{\mathcal{D}} \int_{\mathcal{C}} \chi(v(x, y))(x, y) \, dy \, dx \\
 &\quad + \beta \frac{1}{2} \int_{\mathcal{D}} \int_{\mathcal{C}} \varepsilon |\nabla v(x, y)|^2 + \frac{1}{\varepsilon} \psi(v(x, y)) \, dy \, dx.
 \end{aligned}$$

for $\nu, \beta > 0$. All terms of $\mathcal{J}[v, u[v]]$ are fine-scale equivalents of the one-scale compliance energy terms: The target energy again is composed of weighted terms measuring the deformation, the volume and the interface length, where the latter two are defined using the micro-scale phase field. For the optimization, the derivative

$$\mathcal{J}'[v] = \partial_v \mathcal{J}[v, u[v]] + \partial_u \mathcal{J}[v, \hat{u}[v]](\partial_v u[v])$$

is required. To avoid the computationally very expensive derivative $\partial_v \hat{u}[v]$, we employ a dual problem: Find the dual solution $p = (\bar{p}[v], \tilde{p}[v]) \in W_{\Gamma_D}^{1,2}$ as weak solution of the problem

$$\partial_{uu} \mathcal{E}[v, u[v]](p) = \partial_u \mathcal{J}[v, u[v]]$$

with $\mathcal{E}[v, u[v]] = \frac{1}{2} \int_{\mathcal{D}} \int_{\mathcal{C}} C \epsilon[u] : \epsilon[u] \, dy \, dx$ for all $\phi \in W_{\Gamma_D}^{1,2}$. In the case described here, the dual solution is $p[v] = 2u[v]$.

Corollary 28. *For $\mathcal{E}[v, u[v]]$ and $\mathcal{J}[v, u[v]]$ as defined above, the solution of the dual problem is given by $p = 2u$. Thus, the derivative can be written as*

$$\delta_v \mathcal{J}[v] = \int_{\mathcal{D}} \int_{\mathcal{C}} (\partial_v C)(y) \epsilon[u[v]](x, y) : \epsilon[u[v]](x, y) \, dy \, dx.$$

Proof. The condition on p given by the dual problem is

$$\partial_{uu} \mathcal{E}[v, u[v]](p) = \partial_u \mathcal{J}[v, u[v]].$$

Calculating the derivatives, this equation can be rewritten as

$$\int_{\mathcal{D}} \int_{\mathcal{C}} C \epsilon[p] : \epsilon[\theta] \, dy \, dx = 2 \int_{\mathcal{D}} \int_{\mathcal{C}} \epsilon[u] : \epsilon[\theta] \, dy \, dx$$

and is solved by $p = 2u$.

Now, we can rewrite the derivative

$$\begin{aligned}
 \delta_v \mathcal{J}[v, u[v]](\theta) &= \partial_v \mathcal{J}[v, u[v]](\theta) + \partial_{uu}^2 \mathcal{E}[v, u[v]](p)(\partial_v u[v])(\theta) \\
 &= \partial_v \mathcal{J}[v, u[v]](\theta) - \partial_{uu}^2 \mathcal{E}[v, u[v]](p)(\partial_{uu}^2 \mathcal{E}^{-1}[v, u[v]](\partial_{uv}^2 \mathcal{E}[v, u[v]])(\theta)) \\
 &= \partial_v \mathcal{J}[v, u[v]](\theta) - \partial_{uv}^2 \mathcal{E}[v, u[v]](p)(\theta)
 \end{aligned} \tag{5.3}$$

5. Fine-scale elastic shape optimization

and inserting the formulas given above we conclude

$$\begin{aligned}\delta_v \mathcal{J}[v] &= \partial_v \mathcal{J}[v, u[v]] - \int_{\mathcal{D}} \int_{\mathcal{C}} (\partial_v C)(v)(y) \epsilon[u[v]](x) : \epsilon[p[v]](x) \, dy \, dx \\ &= \int_{\mathcal{D}} \int_{\mathcal{C}} (\partial_v C)(v)(y) \epsilon[u[v]](x) : \epsilon[u[v]](x) \, dy \, dx.\end{aligned}$$

The second equation of (5.3) makes use of the implicit function theorem, which – applied to this case – states, that

$$\partial_v u[v] = -(\partial_{uu}^2 \mathcal{E}^{-1}[v, u[v]])(\partial_{uv}^2 \mathcal{E}[v, u[v]])$$

in a neighborhood of v . This concludes the proof. \square

Now we have to compute $\partial_v C^*(x)$. First, recall that the entries of C^* can be calculated using ϵ_{ij} as described in (5.2). In analogy to (5.1), define the local cost functional for fixed i, j, k, l as

$$\mathcal{J}_C[v, w] := \int_{\mathcal{C}} C(v)(y) (\epsilon_{ij\pm kl} + \epsilon[w[v]](x, y)) : (\epsilon_{ij\pm kl} + \epsilon[w[v]](x, y)) \, dy,$$

and let $w_{ij\pm kl}^*$ solve the local correction problem

$$\int_{\mathcal{C}} C(v)(y) (\epsilon_{ij\pm kl} + \epsilon[w](x, y)) : \epsilon[\psi](x, y) \, dy = 0$$

for all $\psi \in W_{\text{per}}^{1,2}(\mathcal{C})$ and fixed x . This implies $\partial_w \mathcal{J}_C[v, w_{ij\pm kl}[v]] = 0$.

Define $\mathcal{J}_c[v] = \mathcal{J}_C[v, w_{ij\pm kl}^*[v]]$ and conclude $\partial_v \mathcal{J}_C[v] = \partial_v \mathcal{J}_c[v, w_{ij\pm kl}^*[v]]$. This enables us to calculate the variation of the local cost $\mathcal{J}_C[V]$ in direction w .

Recall, that $C(x, y) := ((1 - \delta)\chi(v(y)) + \delta)C_{LN}$ and consider

$$\begin{aligned}\partial_v J_C[v](\theta) &= \partial_\varepsilon J_C[v + \varepsilon\theta]|_{\varepsilon=0} = \partial_\varepsilon J_C[v + \varepsilon\theta, w_{ij\pm kl}]|_{\varepsilon=0} \\ &= \partial_\varepsilon \int_{\mathcal{C}} C(v + \varepsilon\theta)(y) (\epsilon_{ij\pm kl} + \epsilon[w_{ij\pm kl}^*[v]](x, y)) \\ &\quad : (\epsilon_{ij\pm kl} + \epsilon[w_{ij\pm kl}^*[v]](x, y)) \, dy|_{\varepsilon=0} \\ &= \partial_\varepsilon \int_{\mathcal{C}} ((1 - \delta)\chi(v + \varepsilon\theta) + \delta)C_{LN} (\epsilon_{ij\pm kl} + \epsilon[w_{ij\pm kl}^*[v]](x, y)) \\ &\quad : (\epsilon_{ij\pm kl} + \epsilon[w_{ij\pm kl}^*[v]](x, y)) \, dy|_{\varepsilon=0} \\ &= \int_{\mathcal{C}} (1 - \delta)\chi(v)\theta C_{LN} (\epsilon_{ij\pm kl} + \epsilon[w_{ij\pm kl}^*[v]](x, y)) \\ &\quad : (\epsilon_{ij\pm kl} + \epsilon[w_{ij\pm kl}^*[v]](x, y)) \, dy.\end{aligned}$$

Then, the variation of the effective elasticity tensor in a direction w is

$$\begin{aligned} \partial_v C_{ijkl}^*[v](\theta) = & \int_{\mathcal{C}} (1 - \delta) \frac{\partial}{\partial v} \chi(v) \theta \left((\epsilon_{ij+kl} + \epsilon[w_{ij+kl}^*](x, y)) : (\epsilon_{ij+kl} + \epsilon[w_{ij+kl}^*](x, y)) \right. \\ & \left. - (\epsilon_{ij-kl} + \epsilon[w_{ij-kl}^*](x, y)) : (\epsilon_{ij-kl} + \epsilon[w_{ij-kl}^*](x, y)) \right) dy. \end{aligned}$$

With this formula it is possible to evaluate the variation of C_{ijkl}^* in every single component of C^* . Thus, it is of course also possible to evaluate the variation of $C^* \epsilon[u](x) : \epsilon[u](x) dx$ (as in (5.1)) directly by writing u as a linear combination of basis functions.

As all energies and derivatives are now easily computable, basic shape optimization problems reduce to an energy descent algorithm. Alternatively, instead of introducing a dual problem, we can use a Lagrangian formulation and optimize all variables in parallel. For most cases discussed in this thesis, we chose the formulation using a dual problem, as this formulation tends to be more stable than the Lagrangian formulation and reduces the size of the matrices, that are used in numerical applications.

Lagrangian approach

Another approach for optimizing the fine-scale optimization problem is to find a saddle-point of the Lagrangian directly. This method is less stable than the method described above, but allows for easy computations of the Hessian and thus the optimization by Newton's method, which converges quadratically in a neighborhood around the solution.

We begin by defining a bilinear form that will help to simplify the notation of the Lagrangian functionals.

Definition 29. Let

$$\begin{aligned} a(v)(u, p) &= a(v)((\bar{u}, \tilde{u}), (\bar{p}, \tilde{p})) \\ &:= \frac{1}{2} C(v)(x, y) (\epsilon[\bar{u}](x) + \epsilon[\tilde{u}](x, y)) : (\epsilon[\bar{p}](x) + \epsilon[\tilde{p}](x, y)) \\ \partial_v a(v)(\theta)(u, p) &= \partial_v \frac{1}{2} C(v)(\theta) (\epsilon[\bar{u}](x) + \epsilon[\tilde{u}](x, y)) : (\epsilon[\bar{p}](x) + \epsilon[\tilde{p}](x, y)) \end{aligned}$$

and $\partial_{\bar{u}} a(v)((\bar{u}, \tilde{u}), (\bar{p}, \tilde{p}))$, $\partial_{\tilde{u}} a(v)((\bar{u}, \tilde{u}), (\bar{p}, \tilde{p}))$, $\partial_{\bar{p}} a(v)((\bar{u}, \tilde{u}), (\bar{p}, \tilde{p}))$, $\partial_{\tilde{p}} a(v)((\bar{u}, \tilde{u}), (\bar{p}, \tilde{p}))$ the partial derivatives of $a(v)$. The bilinear form $a(v)(u, p)(x, y)$ depends on x and y , but for the sake of clarity, the (x, y) dependency will be often omitted.

As in section 5.1, $C(v)(x, y)$ is defined as

$$C(v)(x, y) = ((1 - \delta)\chi(v(x, y)) + \delta)C_{LN}$$

for given $\delta > 0$ and C_{LN} .

5. Fine-scale elastic shape optimization

Consider the target functional

$$\begin{aligned}\mathcal{J}[v, u] &= 2 \int_{\mathcal{D}} \int_{\mathcal{C}} a(v)((\bar{u}, \tilde{u}), (\bar{u}, \tilde{u}))(x, y) \, dy \, dx \\ &+ \nu \int_{\mathcal{D}} \int_{\mathcal{C}} \chi(v(x, y))(x, y) \, dy \, dx \\ &+ \frac{\beta}{2} \int_{\mathcal{D}} \int_{\mathcal{C}} \varepsilon |\nabla v(x, y)|^2 + \frac{1}{\varepsilon} \psi(v(x, y)) \, dy \, dx,\end{aligned}$$

for $\nu, \beta > 0$.

The Lagrangian can be written as a combination of the target functional, the elasticity constraint, and a dual variable, encoding the constrained optimization problem. Let

$$\begin{aligned}\mathcal{L}[v, u, p] &= \mathcal{J} - \mathcal{E}_{,u}(p) \\ &= 2 \int_{\mathcal{D}} \int_{\mathcal{C}} a(v)((\bar{u}, \tilde{u}), (\bar{u}, \tilde{u}))(x, y) \, dy \, dx \\ &+ \nu \int_{\mathcal{D}} \int_{\mathcal{C}} \chi(v(x, y)) \, dy \, dx \\ &+ \beta \frac{1}{2} \int_{\mathcal{D}} \int_{\mathcal{C}} \varepsilon |\nabla v(x, y)|^2 + \frac{1}{\varepsilon} \psi(v(x, y)) \, dx \\ &- 2 \int_{\mathcal{D}} \int_{\mathcal{C}} a(v)((\bar{u}, \tilde{u}), (\bar{p}, \tilde{p}))(x, y) \, dy \, dx \\ &+ \int_{\Gamma_N} g(x) \cdot \bar{p}(x) \, da,\end{aligned}$$

where the dual variable $p = (\bar{p}(x), \tilde{p}(x, y))$ is defined to have compatible notation with $u = (\bar{u}(x), \tilde{u}(x, y))$ and $v = v(x, y)$.

Solutions to the optimization problem are critical points of the Lagrangian $\mathcal{L}[v, u, p]$, which solve

$$D\mathcal{L}[v, u, p] = \begin{bmatrix} \partial_v \mathcal{L}[v, u, p] \\ \partial_u \mathcal{L}[v, u, p] \\ \partial_p \mathcal{L}[v, u, p] \end{bmatrix} = 0.$$

Explicit formulas for the derivatives of $\mathcal{L}[v, u, p]$ can be found in Appendix A.1.

The variation $\partial_v \mathcal{L}[v, u, p]$ is defined on microscopic domains only, thus creating a fine-scale material. $\partial_u \mathcal{L}[v, u, p] = 0$ defines the *dual problem* that was already introduced in Chapter 5.2.1 and $\partial_p \mathcal{L}[v, u, p]$ is the variation in the control parameters, describing the change of energy that is induced by a change of displacement in a given direction.

Constraints to the micro-scale

Due to periodic boundary conditions, the micro-scale phase field is not unique to translations. As too many possibilities to build the same structure is detrimental to most

numerical algorithms, it is preferable to introduce a constraint that limits each possible configuration to a single translation. We choose to fix the center of mass at the center of the domain: Let

$$M_1 := \frac{1}{M} \int_{\mathcal{C}} \chi(v(y)) y \, dy$$

where $M = \int_{\mathcal{C}} \chi(v(y)) \, dy$ is the mass in the domain \mathcal{C} . Adding the constraint

$$M_1 = \left(\frac{1}{2}, \frac{1}{2} \right)$$

eliminates the ambiguities created by phase field translations. Note, that restricting the rotation of potentially rotationally symmetric structures is not required, as periodic boundary conditions already prevent rotations of the microscopic cell \mathcal{C} .

Rotational degrees of freedom

The alignment of periodic cells with certain axes restricts the number of possible structures to those, which are periodic in these exact cells. One approach that allows a larger set of different structures (e. g. rotated laminates) is the introduction of degrees of freedoms $\alpha \in [0, 2\pi)$ which represent the rotation of a cell \mathcal{C} . Let $R_\alpha(\tilde{u})$ be the matrix encoding a rotation by α . Then the Lagrangian takes the form

$$\begin{aligned} \mathcal{L}[v, u, p, \alpha] &= \mathcal{J}[v, u, \alpha] - \partial_u \mathcal{E}[v, u, \alpha](p) \\ &= 2 \int_{\mathcal{D}} \int_{\mathcal{C}} a(v)((\bar{u}, R_\alpha(\tilde{u})), (\bar{u}, R_\alpha(\tilde{u}))) (x, y) \, dy \, dx \\ &\quad + \nu \int_{\mathcal{D}} \int_{\mathcal{C}} \chi(v(x, y)) \, dy \, dx \\ &\quad + \beta \frac{1}{2} \int_{\mathcal{D}} \int_{\mathcal{C}} \varepsilon |\nabla v(x, y)|^2 + \frac{1}{\varepsilon} \psi(v(x, y)) \, dx \\ &\quad - 2 \int_{\mathcal{D}} \int_{\mathcal{C}} a(v)((\bar{u}, R_\alpha(\tilde{u})), (\bar{p}, R_\alpha(\tilde{p}))) (x, y) \, dy \, dx \\ &\quad + \int_{\Gamma_N} g(x) \cdot \bar{p}(x) \, da, \end{aligned}$$

It is important to note that the introduction of rotations to the degrees of freedom leads to most microstructures representing laminates, modeling their optimality (as described in [All02]), but also reducing the number of different microstructures observed in optimal shapes. Thus, this approach is not examined in depth in this thesis.

5.3. Finite element discretization

For the numerical treatment, the Heterogeneous Multiscale Method (HMM) (cf. [EE03, EE05, EEH03, EMZ05]) can be directly applied. This method models microscopic domains \mathcal{C} inside a macroscopic domain \mathcal{D} by inserting these microscopic domains at each

5. Fine-scale elastic shape optimization

quadrature point, associating a separate set of micro-scale parameters for all these microscopic cells. It was implemented using the finite element mesh introduced in Section 3.4 and the QuocMesh library [QM]. As illustrated in Figure 5.2, those microscopic cells again consist of a finite element mesh that uses the same finite element functions as the macroscopic mesh. Still, functions on the macroscopic domain \mathcal{D} and the microscopic cells \mathcal{C} should and will be clearly distinguished.

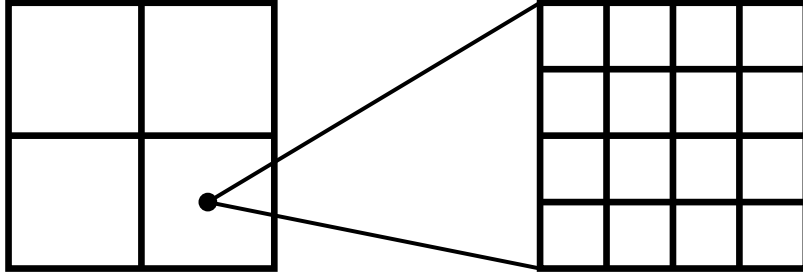


Figure 5.2.: HMM finite elements model the micro-scale explicitly by inserting a micro-scale finite element mesh at every quadrature point of the macroscopic finite element mesh.

Let $Q_h^1(\mathcal{D}_h)$ be a space of quadratic multilinear Finite Elements and let \mathcal{T} s. t. $\cup_{\bar{T} \in \mathcal{T}} \bar{T} = \mathcal{D}_h$. For evaluation of C , the micro-scale \mathcal{C} also has to be discretized. Therefore, introduce a multilinear Finite Element space $\mathcal{T}_{\text{micro}}$, s. t. $\cup_{\tilde{T} \in \mathcal{T}_{\text{micro}}} \tilde{T} = \mathcal{C}$. The quantities v , $u = (\bar{u}, \tilde{u})$ and $p = (\bar{p}, \tilde{p})$ are discretized as functions in $Q_h^1(\mathcal{D}_h)$ and $Q_h^1(\mathcal{D}_h) \times Q_h^1(\mathcal{C}_h)$, respectively and denoted as V , $U = (\bar{U}, \tilde{U})$ and $P = (\bar{P}, \tilde{P})$. For an easier notation, we introduce index sets I and J , s. t. $\mathcal{T} = \cup_{i \in I} \bar{T}_i$ and $\mathcal{T}_{\text{micro}} = \cup_{j \in J} \tilde{T}_j$.

Furthermore, we define the local mesh sizes $H_i = \text{diam } \bar{T}_i$ and $H = \max_{i \in I} H_i$ for the macro-scale mesh and, analogously, h_i and h for the micro-scale mesh.

5.3.1. The discrete problem

Optimizing a discretized version of

$$\begin{aligned} \min \mathcal{J}[v, u[v]], \\ u[v] = \arg \min_{\tilde{u}} \mathcal{E}[v, \tilde{u}] \end{aligned}$$

can be achieved by using the discretized energies of $\mathbf{J}[V, U]$ and $\mathbf{E}[V, U]$ as given above and introducing a discrete dual problem

$$\partial_{UU} \mathcal{E}[V, U[V]](P) = \partial_U \mathcal{J}[V, U[V]] \Theta,$$

where $P = (\bar{P}[V], \tilde{P}[V]) \in Q_h^1(\mathcal{D}_h) \times Q_h^1(\mathcal{C}_h)$. Then, in analogy to the continuous calculations above

$$\begin{aligned} \delta_V \mathbf{J}[V, U[V]]\Theta &= \partial_V \mathbf{J}[V, U[V]]\Theta + \partial_{UU}^2 \mathbf{E}[V, U[V]](P)(\partial_V U[v])\Theta \\ &= \partial_V \mathbf{J}[V, U[V]]\Theta - \partial_{UU}^2 \mathbf{E}[V, U[V]]P(\partial_{UU}^2 \mathbf{E}^{-1}[V, U[V]](\partial_{UV}^2 \mathbf{E}[V, U[V]]\Theta)) \\ &= \partial_V \mathbf{J}[V, U[V]]\Theta - \partial_{UV}^2 \mathbf{E}[V, U[V]]P\Theta. \end{aligned}$$

Note, that in our case, the solution to the dual problem is always given as $P = 2U$. Next, we discretize the local cost functional:

$$\mathbf{J}_C[v, w] := \sum_{\tilde{T} \in \mathcal{T}_{\text{micro}}} |\tilde{T}| \sum_{l \in \tilde{K}_{\tilde{T}}} \tilde{\omega}_l C(V)(\epsilon_{ij\pm kl} + \epsilon[W[V]](\bar{q}, \tilde{q}_l)) : (\epsilon_{ij\pm kl} + \epsilon[W[V]](\bar{q}, \tilde{q}_l)),$$

where \bar{q} is the macroscopic quadrature point at which this local cost is evaluated. The local correction problem transforms into

$$\sum_{\tilde{T} \in \mathcal{T}_{\text{micro}}} |\tilde{T}| \sum_{l \in \tilde{K}_{\tilde{T}}} \tilde{\omega}_l C(\tilde{q}_l)(\epsilon_{ij\pm kl} + \epsilon[W](\bar{q}, \tilde{q}_l)) : \epsilon[\psi](\bar{q}, \tilde{q}_l) = 0. \quad (5.4)$$

for all $\psi \in \mathcal{V}_h$. Denote the solution of problem given in (5.4) as $W_{ij\pm kl}^*$. This implies $\partial_W \mathbf{J}_C[V, W_{ij\pm kl}^*[V]] = 0$. Define $\mathbf{J}_C[V] = \mathbf{J}_C[V, W_{ij\pm kl}^*[V]]$ and conclude

$$\partial_V \mathbf{J}_C[V] = \partial_V \mathbf{J}_c[V, W_{ij\pm kl}^*[V]].$$

Now, we can minimize $\mathbf{J}[V, U[V]]$ by using Algorithm 4 or a similar method.

Algorithm 4: Sketch of gradient descent type algorithm using a dual problem.

Data: Initial values V_{init} , a macroscopic domain \mathcal{D} with given quadrature rule and a defined microscopic cell \mathcal{C} . Boundary values on \mathcal{D} .

Result: An approximation of an optimal structure given as a discrete phase field V .

1. Optimize microscopic cells \mathcal{C} for all quadrature points and all basis loads $\epsilon_{ij\pm kl}$;
 2. Find a combination of the load in terms of basis loads $\epsilon_{ij\pm kl}$ on \mathcal{D}_h ;
 3. Evaluate $\mathbf{J}[V, U[V]]$ and $\delta_V \mathbf{J}[V, U[V]]$ using the local solutions for $\epsilon_{ij\pm kl}$ and the expression of macroscopic loads in terms of these basis loads;
 4. Update V using a gradient descent step (or another suitable algorithm);
-

Remark 30. *The exact type of descent algorithm is not relevant, as long as the chosen algorithm is sufficiently stable. This can e.g. be achieved by using an appropriate step size control like the Armijo [Arm66] step size control for the gradient descent algorithm.*

Additionally, a constraint optimization can be used to introduce constraints to the volume. This can allow us to move the volume cost out of the energy $\mathbf{J}[V, U[V]]$ and into a constraint.

5. Fine-scale elastic shape optimization

We now discretize the energy functionals needed for the Lagrangian approach. As $\mathcal{D} = \mathcal{C} = [0, 1]^2$, we get $Q_h^1(\mathcal{D}_h) = Q_h^1(\mathcal{C}_h)$. Let $\bar{q}_k, \bar{\omega}_k$ be quadrature points and weights of a quadrature rule on \mathcal{T} and $\tilde{q}_k, \tilde{\omega}_k$ points and weights of a quadrature rule on $\mathcal{T}_{\text{micro}}$. The index sets for the quadrature points and weights on elements $\bar{T} \in I$ and $\tilde{T} \in J$ will be denoted as $\bar{K}_{\bar{T}}$ and $\tilde{K}_{\tilde{T}}$.

The target functional $\mathcal{J}[v, u]$ is discretized as

$$\begin{aligned} \mathbf{J}[V, U] &= \sum_{\bar{T} \in \mathcal{T}} |\bar{T}| \sum_{k \in \bar{K}_{\bar{T}}} \bar{\omega}_k C^*(v)(\bar{q}_k) \epsilon[\bar{U}](\bar{q}_k) : \epsilon[\bar{U}](\bar{q}_k) \\ &= \sum_{\bar{T} \in \mathcal{T}} |\bar{T}| \sum_{k \in \bar{K}_{\bar{T}}} \bar{\omega}_k \sum_{\tilde{T} \in \mathcal{T}_{\text{micro}}} |\tilde{T}| \sum_{l \in \tilde{K}_{\tilde{T}}} \tilde{\omega}_l a(V)((\bar{U}, \tilde{U}), (\bar{U}, \tilde{U}))(\bar{q}_k, \tilde{q}_l) \\ &\quad + \nu \sum_{\bar{T} \in \mathcal{T}} |\bar{T}| \sum_{k \in \bar{K}_{\bar{T}}} \bar{\omega}_k \sum_{\tilde{T} \in \mathcal{T}_{\text{micro}}} |\tilde{T}| \sum_{l \in \tilde{K}_{\tilde{T}}} \tilde{\omega}_l \chi(V(\bar{q}_k, \tilde{q}_l)) \\ &\quad + \beta \frac{1}{2} \sum_{\bar{T} \in \mathcal{T}} |\bar{T}| \sum_{k \in \bar{K}_{\bar{T}}} \bar{\omega}_k \sum_{\tilde{T} \in \mathcal{T}_{\text{micro}}} |\tilde{T}| \sum_{l \in \tilde{K}_{\tilde{T}}} \tilde{\omega}_l (\varepsilon |\nabla V(\bar{q}_k, \tilde{q}_l)|^2 + \frac{1}{\varepsilon} \psi(V(\bar{q}_k, \tilde{q}_l))) \end{aligned}$$

and similarly, the elastic energy $\mathcal{E}[v, u]$ as

$$\begin{aligned} \mathbf{E}[V, U] &= \sum_{\bar{T} \in \mathcal{T}} |\bar{T}| \sum_{k \in \bar{K}_{\bar{T}}} \bar{\omega}_k \frac{1}{2} C^*(v)(\bar{q}_k) \epsilon[\bar{U}](\bar{q}_k) : \epsilon[\bar{U}](\bar{q}_k) - \sum_{q_{\Gamma_N, k}} w_{\Gamma_N, k} g(q_{\Gamma_N, k}) \cdot U(q_{\Gamma_N, k}) \\ &= \sum_{\bar{T} \in \mathcal{T}} |\bar{T}| \sum_{k \in \bar{K}_{\bar{T}}} \bar{\omega}_k \sum_{\tilde{T} \in \mathcal{T}_{\text{micro}}} |\tilde{T}| \sum_{l \in \tilde{K}_{\tilde{T}}} \tilde{\omega}_l a(V)((\bar{U}, \tilde{U}), (\bar{U}, \tilde{U}))(\bar{q}_k, \tilde{q}_l) \\ &\quad - \sum_{\partial \bar{T} \in \Gamma_N} \sum_{k \in K_{\partial \bar{T}}} w_{\Gamma_N, k} g(q_{\Gamma_N, k}) \cdot \bar{U}(q_{\Gamma_N, k}), \end{aligned}$$

where $q_{\Gamma_N, k}, w_{\Gamma_N, k}$ are quadrature points and weights of a quadrature rule on Γ_N . Both energies are discretized in a straightforward manner, as all required quantities already exists on the finite element spaces. Furthermore, χ and ψ can be applied to the discretized quantities without modifications.

In a similar fashion, the Lagrangian $\mathcal{L}[v, u]$ is discretized using the energies $\mathbf{J}[V, U]$ and $\mathbf{E}[V, U]$. Again, all quantities are discretized in a straightforward manner and no not

require any non-canonical modification, which results in the formula

$$\begin{aligned}
 \mathbf{L}[V, U, P] &= \mathbf{J}[V, U] - \mathbf{E}_{,U}[V, U](P) \\
 &= 2 \sum_{\bar{T} \in \mathcal{T}} |\bar{T}| \sum_{k \in \bar{K}_{\bar{T}}} \bar{\omega}_k \sum_{\tilde{T} \in \mathcal{T}_{\text{micro}}} |\tilde{T}| \sum_{l \in \bar{K}_{\tilde{T}}} \tilde{\omega}_l a(V)((\bar{U}, \tilde{U}), (\bar{U}, \tilde{U})) \\
 &+ \nu \sum_{\bar{T} \in \mathcal{T}} |\bar{T}| \sum_{k \in \bar{K}_{\bar{T}}} \bar{\omega}_k \sum_{\tilde{T} \in \mathcal{T}_{\text{micro}}} |\tilde{T}| \sum_{l \in \bar{K}_{\tilde{T}}} \tilde{\omega}_l \chi(V(\bar{q}_k, \tilde{q}_l)) \\
 &+ \beta \frac{1}{2} \sum_{\bar{T} \in \mathcal{T}} |\bar{T}| \sum_{k \in \bar{K}_{\bar{T}}} \bar{\omega}_k \sum_{\tilde{T} \in \mathcal{T}_{\text{micro}}} |\tilde{T}| \sum_{l \in \bar{K}_{\tilde{T}}} \tilde{\omega}_l (\varepsilon |\nabla V(\bar{q}_k, \tilde{q}_l)|^2 + \frac{1}{\varepsilon} \psi(V(\bar{q}_k, \tilde{q}_l))) \\
 &- \sum_{\bar{T} \in \mathcal{T}} |\bar{T}| \sum_{k \in \bar{K}_{\bar{T}}} \bar{\omega}_k \sum_{\tilde{T} \in \mathcal{T}_{\text{micro}}} |\tilde{T}| \sum_{l \in \bar{K}_{\tilde{T}}} \tilde{\omega}_l a(V)((\bar{U}, \tilde{U}), (\bar{P}, \tilde{P})) \\
 &+ \sum_{\partial \bar{T} \in \Gamma_N} \sum_{k \in K_{\partial \bar{T}}} \omega_{\Gamma_n, k} g(q_{\Gamma_N, k}) \cdot P(q_{\Gamma_N, k}).
 \end{aligned}$$

Finally, we derive the discrete fine-scale elastic shape optimization problem, which demands for a critical point of $D\mathbf{L}[V, U, P]$, all of which fulfill

$$D\mathbf{L}[V, U, P] = \begin{bmatrix} \partial_V \mathbf{L}[V, U, P] \\ \partial_U \mathbf{L}[V, U, P] \\ \partial_P \mathbf{L}[V, U, P] \end{bmatrix} = 0.$$

Explicit formulas for first and second derivatives of the Lagrangian can be found in Appendix A.2.

For finding a saddle point of $\mathbf{L}[V, U, P]$, Newton's method can be used. This takes advantage of the easily computable second derivatives to improve convergence for starting points in a region around the solution and still yields convergence for other starting points, if a suitable step size control is used.

5.4. Specific patterns on the micro-scale

We are now able to numerically optimize a fine-scale elastic structure (both using a dual problem and using the Lagrangian formulation), but still need to answer the remaining question of how to determine the ratio between the macro and the micro-scale. To this end, we investigate the influence of the interface length term and the respective scaling parameter.

The parameter β determines the scale of the microstructure: A smaller β allows for more repetitions, thus "zooming out" of the periodic structure: When scaling \mathcal{C} — i. e. when the dimensions of \mathcal{C} change in comparison to the macro-scale — the interface term \mathcal{L}^ε scales linearly, while \mathcal{W} and \mathcal{V}^ε scale quadratically. Thus, $\mathcal{J}[v, \bar{u}[v]]$ is not scale-invariant and in turn β , the constant for \mathcal{L}^ε has an influence on the scale of optimal structures. To better

5. Fine-scale elastic shape optimization

understand that phenomenon, we will consider a cell in a periodic lattice, which in this section is described as a one-scale model (not a two-scale or even fine-scale model). We will apply a constant stress in x_2 direction, for which the optimal shape is an ideal rank-one laminate (as described in [All02]) and adapt pproaches described in [All02, Chapters 1.4 and 1.3] to model a displacement on one cell of a periodic lattice containing such a laminate.

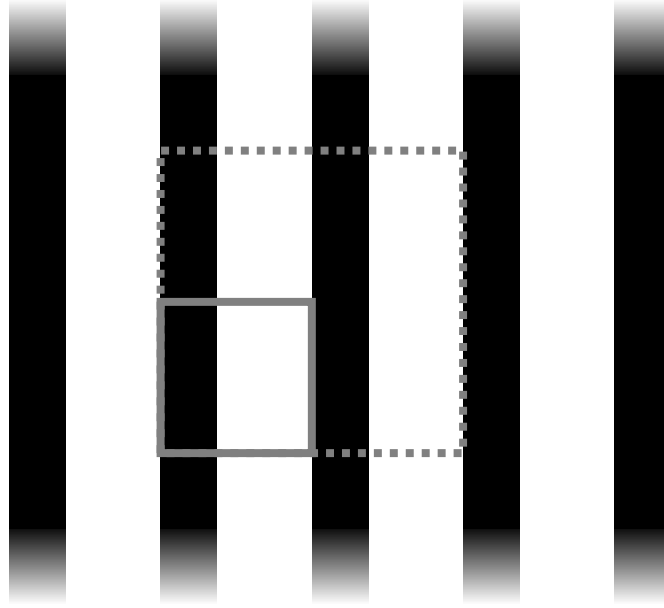


Figure 5.3.: Periodic structure and two periodic cell that result in that same periodic structure when extended.

Figure 5.3 depicts a periodic structure as it is used here and two cells, one containing one repetition of the laminate (gray line) and one that is “zoomed out” to contain two repetitions (dashed gray line). When periodically extended, both cells produce the same periodic lattice. Note, that translations of the laminate in directions perpendicular to its “layers” result in the same laminated structure as well, when the cell is periodically extended (s. Section 5.2.1, Constraints to the micro-scale). Thus, the structure is non-unique (as translations do not change the lattice).

We denote the elasticity tensors of the materials of the laminate as A (hard) and B (soft) and the cell as \mathcal{C} . On \mathcal{C} , we prescribe constant stresses $\sigma_{11} = \sigma_{12} = 0$ and $\sigma_{22} \neq 0$ and consider a displacement

$$\begin{pmatrix} \nu d(x) \\ d(x) \end{pmatrix}.$$

which main contribution exists in the x_2 direction. The displacement in x_1 direction is a result of the coupling by the Poisson ratio ν only. In the given scenario, it is admissible to assume, that the displacement is affine in each phase. Note, that the following computations use this idealized setup as well as some approximations in the computations.

5.4. Specific patterns on the micro-scale

Thus, it can only result in an estimate of the microscale frequency, from which actual (numerically) optimized results might differ to a certain extent. Thus, the function $d(x)$ is given as

$$d(x) := \chi(x_1)a \cdot x + (1 - \chi(x_1))b \cdot x + c(x_1). \quad (5.5)$$

for $a, b \in \mathbb{R}$ and $c(x_1)$ piecewise constant to ensure that $d(x)$ is continuous in \mathbb{R}^2 . The continuity of $d(x)$ over the cell \mathcal{C} implies further conditions on a and b : At the interface between two phases $c(x_1)$ is discontinuous. Consider two points x and y on that interface. We deduce

$$(a - b) \cdot x = (a - b) \cdot y$$

and that there exists a real number $t \in \mathbb{R}$ with

$$b - a = te_1,$$

Using this t , equation (5.5) can be rewritten as

$$d(x) = a \cdot x + (1 - \chi(x_1))tx_1 + c(x_1).$$

Assuming for the elasticity tensors $A = C$ and $B = \delta C$, we conclude from the jump condition at the interface $(Aa)e_1 = (Bb)e_1$, that

$$t = \frac{(A - B)_{i2k2}a_k \cdot e_1}{B_{i2k2}(e_1)_k \cdot e_1} = \frac{(A - B)_{12k2}a_k}{B_{1212}}.$$

Inserting the entries of the Lamé–Navier Tensor, this simplifies to

$$t = \frac{(A - B)_{12k2}a_k}{B_{1212}} = \frac{(A - B)_{1212}a_1 + (A - B)_{1222}a_2}{\frac{\delta E}{1-\nu^2} \frac{1-\nu}{2}} = \frac{\frac{(1-\delta)E}{1-\nu^2} \frac{1-\nu}{2} a_1}{\frac{\delta E}{1-\nu^2} \frac{1-\nu}{2}},$$

leading to the equations

$$t = \frac{(1 - \delta)}{\delta} a_1 \text{ and } b - a = \frac{(1 - \delta)a_1}{\delta} e_1.$$

Now b can be written as

$$\begin{pmatrix} b_1 \\ b_2 \end{pmatrix} = \begin{pmatrix} \frac{1}{\delta} a_1 \\ a_2 \end{pmatrix},$$

expressing b in terms of a and δ .

Following along the lines of [All02, Chapter 1.4], we can deduce a formula for the homogenized stress on a laminated material (we have $\sigma_{11} = \sigma_{12} = 0$ and $\sigma_{22} \neq 0$): Let σ^A and σ^B denote the elasticity tensors of two materials A and B . Then the homogenized stress

$$\sigma^* = \alpha \sigma^A + (1 - \alpha) \sigma^B,$$

where α is the local density (the limit of the characteristic functions).

5. Fine-scale elastic shape optimization

Recall, that for the Lamé–Navier tensor the equation

$$\begin{pmatrix} \sigma_{11} \\ \sigma_{22} \\ \sigma_{12} \end{pmatrix} = \frac{E}{1 - \nu^2} \begin{pmatrix} 1 & \nu & 0 \\ \nu & 1 & 0 \\ 0 & 0 & \frac{1-\nu}{2} \end{pmatrix} \begin{pmatrix} \epsilon_{11} \\ \epsilon_{22} \\ 2\epsilon_{12} \end{pmatrix}$$

holds (using Voigt notation). We can derive the equations

$$\begin{aligned} \epsilon_{22}^P &= \frac{1}{E^P} \sigma_{22}^P \\ \epsilon_{11}^P &= \frac{\nu}{E^P} \sigma_{22}^P, \end{aligned}$$

for $P = A$ or $P = B$ and $E^A = E$, $E^B = \delta E$. Together with the previous computations, these formulas implicate equations for

$$\begin{aligned} a_2 &= \frac{\sigma_{22}^*}{E(\alpha + (1 - \delta)\delta)} \\ a_1 &= -\frac{\sigma_{22}^*}{E} \end{aligned}$$

and thus for the deformation on both the hard and soft phase.

5.4.1. Low-dimension optimization problem

If the cell matches a perfectly integral repetition of the periodic structure, any greater integral number of repetitions of the microstructure in the unit cell would be equally well-suited, but for given a and b as well as given material parameters this is not a valid assumption. A general cell might contain a non-integral number of repetitions and thus conflict with the periodic boundary conditions. This leads to an increase in the deformation energy, which corrects the non-periodic displacements which in turn favors finer microstructures, i. e. a higher number of repetitions in the unit cell (or a higher microstructure frequency) because more repetitions lower the necessary correction. Let k be the number of repetitions of microstructures in the cell \mathcal{C} . (As an example, $k = 1$ corresponds to a laminate with one soft and one hard part per unit cell.)

We still assume that the optimal microstructure for prescribed stresses is a rank-one laminate (in accordance with [All02]).

Let us first investigate how a perfectly periodic structure would be composed. For now, assume $k = 1$. For the displacement $u(x)$ at x , denote $f(x) := u_2(x, 1)$ and let $x_1, x_2 \in [0, 1]$ and $c_1 \in \mathbb{R}$ s. t.

$$f(x) = \begin{cases} a_1 x + c_1 & x \in [0, x_1) \\ b_1(x - x_1) + a_1 x_1 + c_1 & x \in [x_1, x_2) \\ a_1(x - x_1) + b_1(x_2 - x_1) + a_1 x_1 + c_1 & x \in [x_1, 1]. \end{cases}$$

For a perfectly periodic function, $f(0) = f(1)$ holds. This is true, if $x_2 = x_1 + s$ for $s := \frac{a_1}{a_1 - b_1}$. Let $x_1 + s =: x_s$ from here on.

In general (precisely, if $x_2 \neq x_s$) there will be no exact periodicity, so additional deformation energy has to be invested to correct the displacement. If k is incremented by 1, s is halved i. e. $|x_2 - x_s| \rightarrow 0$ for $k \rightarrow \infty$. Accordingly, a bigger k is preferred if the given a , b and α do not result in a perfectly periodic structure.

Let us now model the deformation energy of the periodicity violation: Consider the $k = 1$ case and let x_1, x_2 maximal s. t. $[x_1, x_2]$ is a soft phase. Let s be the optimal width of a soft phase (s. t. perfect periodicity would be achieved). Then $x_2 = x_1 + \frac{1-\alpha}{k}$ for an $\alpha \in \mathbb{R}$. We can assume w. l. o. g., that $x_1 = 0$. The periodicity violation will be approximated by a linear deformation on the soft part only, at most of the size of a unit cell:

$$(a - b)(x_2 - x_s) = (a - b)\left(\frac{1 - \alpha}{k} - s\right) \bmod 1 \quad (5.6)$$

Note, that moving the periodicity violation to the soft material is admissible, as correcting the loss of periodicity in the hard material would result in a much higher deformation energy. The term of interest is the deformation energy of (5.6), which can be written as

$$\frac{(\alpha - 1) \left(\lambda \nu^2 + \nu \left(\nu^2 + \frac{1}{2} \right) \right) \left(\frac{(a-b)(1-k s - \alpha)}{k} \bmod 1 \right)^2}{k} =: \mathcal{W}_p.$$

Now we minimize

$$\min_{k, \alpha} 2\mathcal{W}[a, b] + \nu\alpha + 2\beta k + \mathcal{W}_p, \quad (5.7)$$

for k and α , for $\nu, \beta > 0$ under the constraint $\alpha \in \{0, 1\}$. As $\mathcal{W}[a, b]$ is independent of k , (5.7) simplifies to

$$\min_{k, \alpha} \nu\alpha + 2\beta k + \mathcal{W}_p. \quad (5.8)$$

which is a two-dimensional constraint optimization problem.

Solving (5.8) allows for an estimate on the influence of β on the number of repetitions of the microstructure in a single unit cell \mathcal{C} and in turn to find a suitable $\beta > 0$ for which the optimal shape shows a single representation of the microstructure per unit cell. That in turn later allows for the maximal resolution for a given depth.

5.5. Results

The fine-scale model was applied to a pressure and a shear scenario, that were designed to allow a comparison of the result with the laminates, as described by Allaire [All02]. The setup for both loads scenario $\mathcal{D} = [0, 1]^2$ compression or shear loads on two and all boundaries, respectively. We expect a uniform microstructure across the whole domain, which will model laminates on the scale determined by β .

5. Fine-scale elastic shape optimization

The macroscopic domain \mathcal{D} and the microscopic domain \mathcal{C} were discretized using Q^1 finite elements on $[0, 1]^2$. The macroscopic domain consisted of 16 elements, each containing one quadrature point at their center at which the microscopic domains were placed and evaluated. On the microscale, the center-of-mass quadrature is used.

5.5.1. Compression load

In this setup, compression loads of value $\|F\| = 1$ were applied on top and bottom of the macroscopic domain \mathcal{D} and periodic boundary conditions were prescribed on the left and right boundary, effectively modeling an infinite strip of periodically repeating structures.

For the Lamé–Navier tensor, parameters $\lambda = \mu = 80$ were chosen. The volume and interface terms of the target functional $\mathcal{J}[V, U[V]]$ were chosen as $\nu = 0.01$ and $\beta = 0.00256$, respectively, where β was optimized to enforce one repetition of the microscale per cell \mathcal{C}_h . The parameter relating the hard and soft material was set to $\delta = 10^{-4}$ and the phase field parameter was set to $\varepsilon = 0.05$. The optimization was initialized with a guess of the optimal structure. No constraints on the center of gravity were necessary for this setup.

For the compression load, an optimal microstructure is a rank-one laminate in the direction of loads. This is reflected by the result of the fine-scale optimization: All simulated cells show the same pillar-like structure, which is a suitable phase field representation of a laminate of a hard and a soft material.

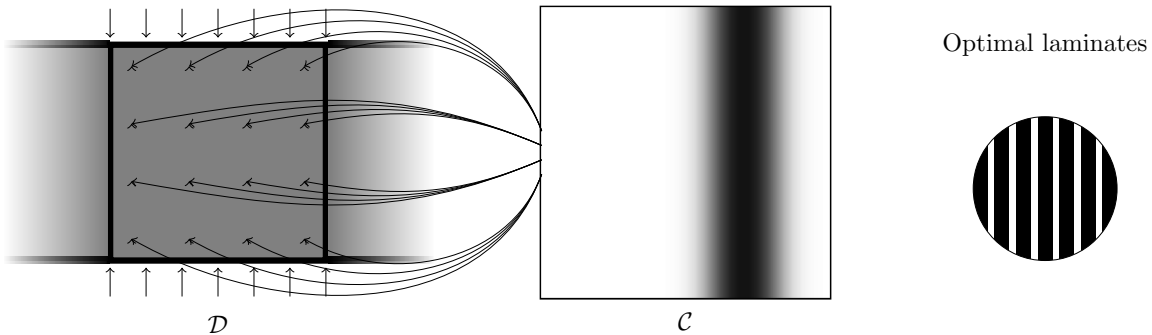


Figure 5.4.: Compression load scenario and optimized fine-scale structure (left), which models the optimal laminate (right).

As expected, there is no variation in microstructure over the macroscopic domain. Figure 5.4 shows one representation of the microstructure and the macroscopic quadrature point (bottom) as well as the expected microstructure (top).

5.5.2. Shear load

Here, shear loads of magnitude $\|F\| = 1$ were applied on top and bottom boundary, again modeling a strip of infinitely repeating elastic structures. The finite element setup is the

same as in the compression case, using 16 macroscopic elements containing on quadrature point (i. e. microscopic cell) each.

For the Lamé–Navier tensor, parameters again $\lambda = \mu = 80$ were chosen. The volume and interface terms of the target functional $\mathcal{J}[V, U[V]]$ were chosen as $\nu = 0.016$ and $\beta = 0.001$, respectively, where the choice of β should enforce one repetition of the microscale per cell \mathcal{C}_h . The parameter relating the hard and soft material was set to $\delta = 10^{-4}$ and the phase field parameter was set to $\varepsilon = 0.025$. The optimization was again initialized with a guess of the optimal structure.

The expected microstructure is a rank-two laminate. This can be modeled by the phase field as a cross-structure, which — if periodically extended — shows the same topological structure.

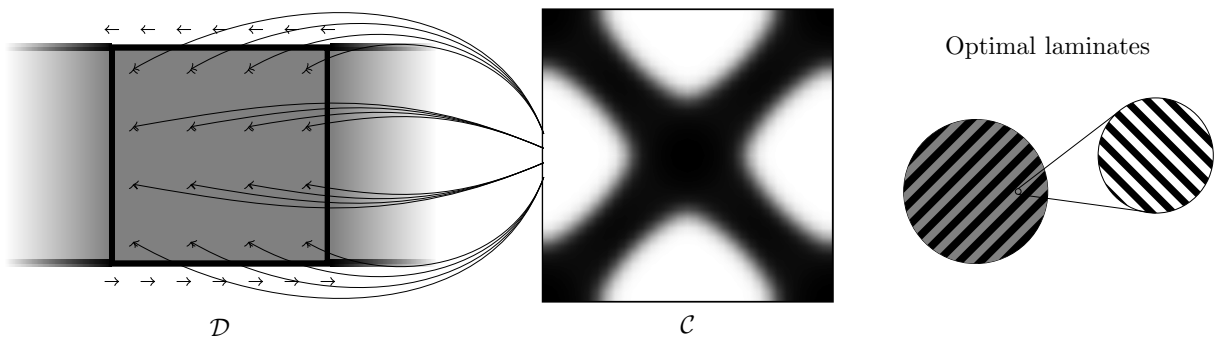


Figure 5.5.: Shear load scenario and optimized fine-scale structure (left), which approximates the optimal laminate (right).

In Figure 5.5 the optimal laminate is sketched (top) as well as the microstructure resulting from the numerical optimization. Again, the microstructure does not vary over the macroscopic domain.

5.6. Conclusion

We developed an algorithm to optimize fine-scale materials under a given set of boundary conditions. To make the algorithm more efficient, adaptive mesh refinement could be introduced to both the macro-scale and micro-scale. Here, a posteriori error estimates can be a useful tool to determine, which elements to refine. Some work on multiscale error estimates has been done by Liu et. al. in [LCYC15] for a priori estimates and Rumpf et. al. in [CGLR17] for a posteriori error estimates.

Furthermore, introducing model adaptivity we could only model those parts of the domain using the fine-scale model, where the optimal structure cannot be approximated by a one-scale approach. This can be useful to reduce the computational cost when optimizing more general domains and setups as the ones described above.

Appendices

A. Derivatives of two-scale functionals

A.1. Continuous quantities

Partial derivatives of the Lagrangian:

$$\begin{aligned}
\partial_\nu \mathcal{L}[v, u, p](\nu) &= 2 \int_{\mathcal{D}} \int_{\mathcal{C}} \partial_\nu a(v)(\nu)((\bar{u}, \tilde{u}), (\bar{u}, \tilde{u}))(x, y) \, dy \, dx \\
&\quad + \nu \int_{\mathcal{D}} \int_{\mathcal{C}} \partial_\nu \chi(v(x, y)) \nu(x, y) \, dy \, dx \\
&\quad + \beta \frac{1}{2} \int_{\mathcal{D}} \int_{\mathcal{C}} \varepsilon \nabla v(x, y) \nabla \nu + \frac{1}{\varepsilon} \partial_\nu \psi_{MM}(v(x, y)) \nu \, dy \, dx \\
&\quad - 2 \int_{\mathcal{D}} \int_{\mathcal{C}} \partial_\nu a(v)(\theta)((\bar{u}, \tilde{u}), (\bar{p}, \tilde{p}))(x, y) \, dy \, dx, \\
\partial_u \mathcal{L}[v, u, p](\theta, \nu) &= \left(2 \int_{\mathcal{D}} \int_{\mathcal{C}} \partial_{\bar{u}} a(v)((\bar{u}, \tilde{u}), (\bar{u}, \tilde{u}))(\theta)(x, y) \, dy \, dx \right. \\
&\quad - 2 \int_{\mathcal{D}} \int_{\mathcal{C}} \partial_{\bar{u}} a(v)((\bar{u}, \tilde{u}), (\bar{p}, \tilde{p}))(\theta)(x, y) \, dy \, dx, \\
&\quad 2 \int_{\mathcal{D}} \int_{\mathcal{C}} \partial_{\bar{u}} a(v)((\bar{u}, \tilde{u}), (\bar{u}, \tilde{u}))(\nu)(x, y) \, dy \, dx \\
&\quad \left. - 2 \int_{\mathcal{D}} \int_{\mathcal{C}} \partial_{\bar{u}} a(v)((\bar{u}, \tilde{u}), (\bar{p}, \tilde{p}))(\nu)(x, y) \, dy \, dx \right), \\
\partial_p \mathcal{L}[v, u, p](\theta, \nu) &= \left(-2 \int_{\mathcal{D}} \int_{\mathcal{C}} \partial_{\bar{p}} a(v)((\bar{u}, \tilde{u}), (\bar{p}, \tilde{p}))(\theta)(x, y) \, dy \, dx + \int_{\Gamma_N} g(x) \cdot \theta(x) \, da, \right. \\
&\quad \left. - 2 \int_{\mathcal{D}} \int_{\mathcal{C}} \partial_{\bar{p}} a(v)((\bar{u}, \tilde{u}), (\bar{p}, \tilde{p}))(\nu)(x, y) \, dy \, dx \right).
\end{aligned}$$

A. Derivatives of two-scale functionals

Second partial derivatives of the Lagrangian:

$$\begin{aligned}
\partial_{vv}^2 \mathcal{L}[v, u, p](\nu_1)(\nu_2) &= 2 \int_{\mathcal{D}} \int_{\mathcal{C}} \partial_{vv}^2 a(v)(\nu_1)(\nu_2)((\bar{u}, \tilde{u}), (\bar{u}, \tilde{u}))(x, y) \, dy \, dx \\
&\quad + \nu \int_{\mathcal{D}} \int_{\mathcal{C}} \partial_{vv}^2 \chi(v(x, y)) \nu_1 \nu_2(x, y) \, dy \, dx \\
&\quad + \beta \frac{1}{2} \int_{\mathcal{D}} \int_{\mathcal{C}} \varepsilon \nabla \nu_2 \nabla \nu_1 + \frac{1}{\varepsilon} \partial_{vv}^2 \psi_{MM}(v(x, y)) \nu_1 \nu_2 \, dx \\
&\quad - 2 \int_{\mathcal{D}} \int_{\mathcal{C}} \partial_{vv}^2 a(v)(\nu_1)(\nu_2)((\bar{u}, \tilde{u}), (\bar{p}, \tilde{p}))(x, y) \, dy \, dx, \\
\partial_{vu}^2 \mathcal{L}[v, u, p](\nu_1)(\theta_2, \nu_2) &= \left(2 \int_{\mathcal{D}} \int_{\mathcal{C}} \partial_{v\bar{u}}^2 a(v)(\nu_1)((\bar{u}, \tilde{u}), (\bar{u}, \tilde{u}))(\theta_2)(x, y) \, dy \, dx \right. \\
&\quad - 2 \int_{\mathcal{D}} \int_{\mathcal{C}} \partial_{v\bar{u}}^2 a(v)(\nu_1)((\bar{u}, \tilde{u}), (\bar{p}, \tilde{p}))(\theta_2) \, dy \, dx, \\
&\quad 2 \int_{\mathcal{D}} \int_{\mathcal{C}} \partial_{v\bar{u}}^2 a(v)(\nu_1)((\bar{u}, \tilde{u}), (\bar{u}, \tilde{u}))(\nu_2)(x, y) \, dy \, dx \\
&\quad \left. - 2 \int_{\mathcal{D}} \int_{\mathcal{C}} \partial_{v\bar{u}}^2 a(v)(\nu_1)((\bar{u}, \tilde{u}), (\bar{p}, \tilde{p}))(\nu_2) \, dy \, dx \right),
\end{aligned}$$

$$\begin{aligned}
\partial_{vp}^2 \mathcal{L}[v, u, p](\nu_1)(\theta_2, \nu_2) &= \left(- 2 \int_{\mathcal{D}} \int_{\mathcal{C}} \partial_{v\bar{p}}^2 a(v)(\nu_1)((\bar{u}, \tilde{u}), (\bar{p}, \tilde{p}))(\theta_2)(x, y) \, dy \, dx, \right. \\
&\quad \left. - 2 \int_{\mathcal{D}} \int_{\mathcal{C}} \partial_{v\bar{p}}^2 a(v)(\nu_1)((\bar{u}, \tilde{u}), (\bar{p}, \tilde{p}))(\nu_2)(x, y) \, dy \, dx \right),
\end{aligned}$$

$$\begin{aligned}
\partial_{uu}^2 \mathcal{L}[v, u, p](\theta_1, \nu_1)(\theta_2, \nu_2) &= \left(\left\{ 2 \int_{\mathcal{D}} \int_{\mathcal{C}} \partial_{\bar{u}\bar{u}}^2 a(v)((\bar{u}, \tilde{u}), (\bar{u}, \tilde{u}))(\theta_1)(\theta_2)(x, y) \, dy \, dx, \right. \right. \\
&\quad 2 \int_{\mathcal{D}} \int_{\mathcal{C}} \partial_{\bar{u}\bar{u}}^2 a(v)((\bar{u}, \tilde{u}), (\bar{u}, \tilde{u}))(\theta_1)(\nu_2)(x, y) \, dy \, dx \\
&\quad \left. - 2 \int_{\mathcal{D}} \int_{\mathcal{C}} \partial_{\bar{u}\bar{u}}^2 a(v)((\bar{u}, \tilde{u}), (\bar{p}, \tilde{p}))(\theta_1)(\nu_2)(x, y) \, dy \, dx \right\}, \\
&\quad \left\{ 2 \int_{\mathcal{D}} \int_{\mathcal{C}} \partial_{\bar{u}\bar{u}}^2 a(v)((\bar{u}, \tilde{u}), (\bar{u}, \tilde{u}))(\nu_1)(\theta_2)(x, y) \, dy \, dx \right. \\
&\quad - 2 \int_{\mathcal{D}} \int_{\mathcal{C}} \partial_{\bar{u}\bar{u}}^2 a(v)((\bar{u}, \tilde{u}), (\bar{p}, \tilde{p}))(\nu_1)(\theta_2)(x, y) \, dy \, dx, \\
&\quad \left. \left. 2 \int_{\mathcal{D}} \int_{\mathcal{C}} \partial_{\bar{u}\bar{u}}^2 a(v)((\bar{u}, \tilde{u}), (\bar{u}, \tilde{u}))(\nu_1)(\nu_2)(x, y) \, dy \, dx \right\} \right),
\end{aligned}$$

$$\begin{aligned} \partial_{up}^2 \mathcal{L}[v, u, p](\theta_1, \nu_1)(\theta_2, \nu_2) = & \left(\left\{ -2 \int_{\mathcal{D}} \int_{\mathcal{C}} \partial_{\bar{u}\bar{p}}^2 a(v)((\bar{u}, \tilde{u}), (\bar{p}, \tilde{p}))(\theta_1)(\theta_2)(x, y) \, dy \, dx, \right. \right. \\ & \left. \left. -2 \int_{\mathcal{D}} \int_{\mathcal{C}} \partial_{\bar{u}\bar{p}}^2 a(v)((\bar{u}, \tilde{u}), (\bar{p}, \tilde{p}))(\theta_1)(\nu_2)(x, y) \, dy \, dx \right\}, \right. \\ & \left. \left\{ -2 \int_{\mathcal{D}} \int_{\mathcal{C}} \partial_{\bar{u}\bar{p}}^2 a(v)((\bar{u}, \tilde{u}), (\bar{p}, \tilde{p}))(\nu_1)(\theta_2)(x, y) \, dy \, dx, \right. \right. \\ & \left. \left. -2 \int_{\mathcal{D}} \int_{\mathcal{C}} \partial_{\bar{u}\bar{p}}^2 a(v)((\bar{u}, \tilde{u}), (\bar{p}, \tilde{p}))(\nu_1)(\nu_2)(x, y) \, dy \, dx \right\} \right), \end{aligned}$$

$$\begin{aligned} \partial_{pp}^2 \mathcal{L}[v, u, p](\theta_1, \nu_1)(\theta_2, \nu_2) = & \left(\left\{ 0, -2 \int_{\mathcal{D}} \int_{\mathcal{C}} \partial_{\bar{p}\bar{p}}^2 a(v)((\bar{u}, \tilde{u}), (\bar{p}, \tilde{p}))(\theta_1)(\nu_2)(x, y) \, dy \, dx \right\}, \right. \\ & \left. \left\{ -2 \int_{\mathcal{D}} \int_{\mathcal{C}} \partial_{\bar{p}\bar{p}}^2 a(v)((\bar{u}, \tilde{u}), (\bar{p}, \tilde{p}))(\nu_1)(\theta_2)(x, y) \, dy \, dx, 0 \right\} \right). \end{aligned}$$

A.2. Discretized quantities

Discretized first derivatives:

$$\begin{aligned} \partial_V \mathcal{L}[V, U, P](\nu) = & \\ & 2 \sum_{\bar{T} \in \mathcal{T}} |\bar{T}| \sum_{k \in \bar{K}_{\bar{T}}} \bar{\omega}_k \sum_{\tilde{T} \in \mathcal{T}_{\text{micro}}} |\tilde{T}| \sum_{l \in \tilde{K}_{\tilde{T}}} \tilde{\omega}_l \partial_V a(V)(\nu)((\bar{U}, \tilde{U}), (\bar{U}, \tilde{U}))(\bar{q}_k, \tilde{q}_l) \\ & + \nu \sum_{\bar{T} \in \mathcal{T}} |\bar{T}| \sum_{k \in \bar{K}_{\bar{T}}} \bar{\omega}_k \sum_{\tilde{T} \in \mathcal{T}_{\text{micro}}} |\tilde{T}| \sum_{l \in \tilde{K}_{\tilde{T}}} \tilde{\omega}_l \partial_V \chi(V(x, y))\nu(\bar{q}_k, \tilde{q}_l) \\ & + \beta \frac{1}{2} \sum_{\bar{T} \in \mathcal{T}} |\bar{T}| \sum_{k \in \bar{K}_{\bar{T}}} \bar{\omega}_k \sum_{\tilde{T} \in \mathcal{T}_{\text{micro}}} |\tilde{T}| \sum_{l \in \tilde{K}_{\tilde{T}}} \tilde{\omega}_l \varepsilon \nabla V(x, y) \nabla \nu + \frac{1}{\varepsilon} \partial_V \psi_{MM}(V(x, y))\nu \\ & - 2 \sum_{\bar{T} \in \mathcal{T}} |\bar{T}| \sum_{k \in \bar{K}_{\bar{T}}} \bar{\omega}_k \sum_{\tilde{T} \in \mathcal{T}_{\text{micro}}} |\tilde{T}| \sum_{l \in \tilde{K}_{\tilde{T}}} \tilde{\omega}_l \partial_V a(V)(\theta)((\bar{U}, \tilde{U}), (\bar{P}, \tilde{P}))(\bar{q}_k, \tilde{q}_l), \end{aligned}$$

A. Derivatives of two-scale functionals

$$\begin{aligned}
\partial_U \mathcal{L}[V, U, P](\theta, \nu) = & \\
& \left(2 \sum_{\bar{T} \in \mathcal{T}} |\bar{T}| \sum_{k \in \bar{K}_{\bar{T}}} \bar{\omega}_k \sum_{\tilde{T} \in \mathcal{T}_{\text{micro}}} |\tilde{T}| \sum_{l \in \tilde{K}_{\tilde{T}}} \tilde{\omega}_l \partial_{\bar{U}} a(V)((\bar{U}, \tilde{U}), (\bar{U}, \tilde{U}))(\theta)(\bar{q}_k, \tilde{q}_l) \right. \\
& - 2 \sum_{\bar{T} \in \mathcal{T}} |\bar{T}| \sum_{k \in \bar{K}_{\bar{T}}} \bar{\omega}_k \sum_{\tilde{T} \in \mathcal{T}_{\text{micro}}} |\tilde{T}| \sum_{l \in \tilde{K}_{\tilde{T}}} \tilde{\omega}_l \partial_{\bar{U}} a(V)((\bar{U}, \tilde{U}), (\bar{P}, \tilde{P}))(\theta)(\bar{q}_k, \tilde{q}_l), \\
& 2 \sum_{\bar{T} \in \mathcal{T}} |\bar{T}| \sum_{k \in \bar{K}_{\bar{T}}} \bar{\omega}_k \sum_{\tilde{T} \in \mathcal{T}_{\text{micro}}} |\tilde{T}| \sum_{l \in \tilde{K}_{\tilde{T}}} \tilde{\omega}_l \partial_{\tilde{U}} a(V)((\bar{U}, \tilde{U}), (\bar{U}, \tilde{U}))(\nu)(\bar{q}_k, \tilde{q}_l) \\
& \left. - 2 \sum_{\bar{T} \in \mathcal{T}} |\bar{T}| \sum_{k \in \bar{K}_{\bar{T}}} \bar{\omega}_k \sum_{\tilde{T} \in \mathcal{T}_{\text{micro}}} |\tilde{T}| \sum_{l \in \tilde{K}_{\tilde{T}}} \tilde{\omega}_l \partial_{\tilde{U}} a(V)((\bar{U}, \tilde{U}), (\bar{P}, \tilde{P}))(\nu)(\bar{q}_k, \tilde{q}_l) \right),
\end{aligned}$$

$$\begin{aligned}
\partial_P \mathcal{L}[V, U, P](\theta, \nu) = & \\
& \left(- 2 \sum_{\bar{T} \in \mathcal{T}} |\bar{T}| \sum_{k \in \bar{K}_{\bar{T}}} \bar{\omega}_k \sum_{\tilde{T} \in \mathcal{T}_{\text{micro}}} |\tilde{T}| \sum_{l \in \tilde{K}_{\tilde{T}}} \tilde{\omega}_l \partial_{\bar{P}} a(V)((\bar{U}, \tilde{U}), (\bar{P}, \tilde{P}))(\theta)(\bar{q}_k, \tilde{q}_l) \right. \\
& + \sum_{\partial \bar{T} \in \Gamma_N} \sum_{k \in \bar{K}_{\partial \bar{T}}} \omega_{\Gamma_n, k} g(p_{\Gamma_n, k}) \cdot \theta(p_{\Gamma_n, k}) \, da, \\
& \left. - 2 \sum_{\bar{T} \in \mathcal{T}} |\bar{T}| \sum_{k \in \bar{K}_{\bar{T}}} \bar{\omega}_k \sum_{\tilde{T} \in \mathcal{T}_{\text{micro}}} |\tilde{T}| \sum_{l \in \tilde{K}_{\tilde{T}}} \tilde{\omega}_l \partial_{\bar{P}} a(V)((\bar{U}, \tilde{U}), (\bar{P}, \tilde{P}))(\nu)(\bar{q}_k, \tilde{q}_l) \right).
\end{aligned}$$

Discretized versions of the second derivatives:

$$\begin{aligned}
& \partial_{VV}^2 \mathbf{L}[V, U, P](\nu_1)(\nu_2) \\
& = 2 \sum_{\bar{T} \in \mathcal{T}} |\bar{T}| \sum_{k \in \bar{K}_{\bar{T}}} \bar{\omega}_k \sum_{\tilde{T} \in \mathcal{T}_{\text{micro}}} |\tilde{T}| \sum_{l \in \tilde{K}_{\tilde{T}}} \tilde{\omega}_l \partial_{VV}^2 a(V)(\nu_1)(\nu_2)((\bar{U}, \tilde{U}), (\bar{U}, \tilde{U}))(\bar{q}_k, \tilde{q}_l) \\
& + \nu \sum_{\bar{T} \in \mathcal{T}} |\bar{T}| \sum_{k \in \bar{K}_{\bar{T}}} \bar{\omega}_k \sum_{\tilde{T} \in \mathcal{T}_{\text{micro}}} |\tilde{T}| \sum_{l \in \tilde{K}_{\tilde{T}}} \tilde{\omega}_l \partial_{VV}^2 \chi(V)(\bar{q}_k, \tilde{q}_l) \nu_1 \nu_2(\bar{q}_k, \tilde{q}_l) \\
& + \beta \frac{1}{2} \sum_{\bar{T} \in \mathcal{T}} |\bar{T}| \sum_{k \in \bar{K}_{\bar{T}}} \bar{\omega}_k \sum_{\tilde{T} \in \mathcal{T}_{\text{micro}}} |\tilde{T}| \sum_{l \in \tilde{K}_{\tilde{T}}} \tilde{\omega}_l \varepsilon \nabla \nu_2 \nabla \nu_1 + \frac{1}{\varepsilon} \partial_{VV}^2 \psi_{MM}(V)(\bar{q}_k, \tilde{q}_l) \nu_1 \nu_2 \\
& - 2 \sum_{\bar{T} \in \mathcal{T}} |\bar{T}| \sum_{k \in \bar{K}_{\bar{T}}} \bar{\omega}_k \sum_{\tilde{T} \in \mathcal{T}_{\text{micro}}} |\tilde{T}| \sum_{l \in \tilde{K}_{\tilde{T}}} \tilde{\omega}_l \partial_{VV}^2 a(V)(\nu_1)(\nu_2)((\bar{U}, \tilde{U}), (\bar{P}, \tilde{P}))(\bar{q}_k, \tilde{q}_l),
\end{aligned}$$

$$\begin{aligned}
& \partial_{VU}^2 \mathbf{L}[V, U, P](\nu_1)(\theta_2, \nu_2) \\
&= \left(2 \sum_{\tilde{T} \in \mathcal{T}} |\tilde{T}| \sum_{k \in \tilde{K}_{\tilde{T}}} \tilde{\omega}_k \sum_{\tilde{T} \in \mathcal{T}_{\text{micro}}} |\tilde{T}| \sum_{l \in \tilde{K}_{\tilde{T}}} \tilde{\omega}_l \partial_{V\tilde{U}}^2 a(V)(\nu_1)((\bar{U}, \tilde{U}), (\bar{U}, \tilde{U}))(\theta_2)(\bar{q}_k, \tilde{q}_l) \right. \\
&- 2 \sum_{\tilde{T} \in \mathcal{T}} |\tilde{T}| \sum_{k \in \tilde{K}_{\tilde{T}}} \tilde{\omega}_k \sum_{\tilde{T} \in \mathcal{T}_{\text{micro}}} |\tilde{T}| \sum_{l \in \tilde{K}_{\tilde{T}}} \tilde{\omega}_l \partial_{V\tilde{U}}^2 a(V)(\nu_1)((\bar{U}, \tilde{U}), (\bar{P}, \tilde{P}))(\theta_2), \\
& 2 \sum_{\tilde{T} \in \mathcal{T}} |\tilde{T}| \sum_{k \in \tilde{K}_{\tilde{T}}} \tilde{\omega}_k \sum_{\tilde{T} \in \mathcal{T}_{\text{micro}}} |\tilde{T}| \sum_{l \in \tilde{K}_{\tilde{T}}} \tilde{\omega}_l \partial_{V\tilde{U}}^2 a(V)(\nu_1)((\bar{U}, \tilde{U}), (\bar{U}, \tilde{U}))(\nu_2)(\bar{q}_k, \tilde{q}_l) \\
&\left. - 2 \sum_{\tilde{T} \in \mathcal{T}} |\tilde{T}| \sum_{k \in \tilde{K}_{\tilde{T}}} \tilde{\omega}_k \sum_{\tilde{T} \in \mathcal{T}_{\text{micro}}} |\tilde{T}| \sum_{l \in \tilde{K}_{\tilde{T}}} \tilde{\omega}_l \partial_{V\tilde{U}}^2 a(V)(\nu_1)((\bar{U}, \tilde{U}), (\bar{P}, \tilde{P}))(\nu_2) \right),
\end{aligned}$$

$$\begin{aligned}
& \partial_{VP}^2 \mathbf{L}[V, U, P](\nu_1)(\theta_2, \nu_2) \\
&= \left(- 2 \sum_{\tilde{T} \in \mathcal{T}} |\tilde{T}| \sum_{k \in \tilde{K}_{\tilde{T}}} \tilde{\omega}_k \sum_{\tilde{T} \in \mathcal{T}_{\text{micro}}} |\tilde{T}| \sum_{l \in \tilde{K}_{\tilde{T}}} \tilde{\omega}_l \partial_{V\tilde{P}}^2 a(V)(\nu_1)((\bar{U}, \tilde{U}), (\bar{P}, \tilde{P}))(\theta_2)(\bar{q}_k, \tilde{q}_l), \right. \\
&\left. - 2 \sum_{\tilde{T} \in \mathcal{T}} |\tilde{T}| \sum_{k \in \tilde{K}_{\tilde{T}}} \tilde{\omega}_k \sum_{\tilde{T} \in \mathcal{T}_{\text{micro}}} |\tilde{T}| \sum_{l \in \tilde{K}_{\tilde{T}}} \tilde{\omega}_l \partial_{V\tilde{P}}^2 a(V)(\nu_1)((\bar{U}, \tilde{U}), (\bar{P}, \tilde{P}))(\nu_2)(\bar{q}_k, \tilde{q}_l) \right),
\end{aligned}$$

$$\begin{aligned}
& \partial_{UU}^2 \mathbf{L}[V, U, P](\theta_1, \nu_1)(\theta_2, \nu_2) \\
&= \left(\left\{ 2 \sum_{\tilde{T} \in \mathcal{T}} |\tilde{T}| \sum_{k \in \tilde{K}_{\tilde{T}}} \tilde{\omega}_k \sum_{\tilde{T} \in \mathcal{T}_{\text{micro}}} |\tilde{T}| \sum_{l \in \tilde{K}_{\tilde{T}}} \tilde{\omega}_l \partial_{\tilde{U}\tilde{U}}^2 a(V)((\bar{U}, \tilde{U}), (\bar{U}, \tilde{U}))(\theta_1)(\theta_2)(\bar{q}_k, \tilde{q}_l), \right. \right. \\
& 2 \sum_{\tilde{T} \in \mathcal{T}} |\tilde{T}| \sum_{k \in \tilde{K}_{\tilde{T}}} \tilde{\omega}_k \sum_{\tilde{T} \in \mathcal{T}_{\text{micro}}} |\tilde{T}| \sum_{l \in \tilde{K}_{\tilde{T}}} \tilde{\omega}_l \partial_{\tilde{U}\tilde{U}} a(V)((\bar{U}, \tilde{U}), (\bar{U}, \tilde{U}))(\theta_1)(\nu_2)(\bar{q}_k, \tilde{q}_l) \\
&\left. - 2 \sum_{\tilde{T} \in \mathcal{T}} |\tilde{T}| \sum_{k \in \tilde{K}_{\tilde{T}}} \tilde{\omega}_k \sum_{\tilde{T} \in \mathcal{T}_{\text{micro}}} |\tilde{T}| \sum_{l \in \tilde{K}_{\tilde{T}}} \tilde{\omega}_l \partial_{\tilde{U}\tilde{U}}^2 a(V)((\bar{U}, \tilde{U}), (\bar{P}, \tilde{P}))(\theta_1)(\nu_2)(\bar{q}_k, \tilde{q}_l) \right\}, \\
& \left\{ 2 \sum_{\tilde{T} \in \mathcal{T}} |\tilde{T}| \sum_{k \in \tilde{K}_{\tilde{T}}} \tilde{\omega}_k \sum_{\tilde{T} \in \mathcal{T}_{\text{micro}}} |\tilde{T}| \sum_{l \in \tilde{K}_{\tilde{T}}} \tilde{\omega}_l \partial_{\tilde{U}\tilde{U}}^2 a(V)((\bar{U}, \tilde{U}), (\bar{U}, \tilde{U}))(\nu_1)(\theta_2)(\bar{q}_k, \tilde{q}_l) \right. \\
&- 2 \sum_{\tilde{T} \in \mathcal{T}} |\tilde{T}| \sum_{k \in \tilde{K}_{\tilde{T}}} \tilde{\omega}_k \sum_{\tilde{T} \in \mathcal{T}_{\text{micro}}} |\tilde{T}| \sum_{l \in \tilde{K}_{\tilde{T}}} \tilde{\omega}_l \partial_{\tilde{U}\tilde{U}}^2 a(V)((\bar{U}, \tilde{U}), (\bar{P}, \tilde{P}))(\nu_1)(\theta_2)(\bar{q}_k, \tilde{q}_l), \\
&\left. 2 \sum_{\tilde{T} \in \mathcal{T}} |\tilde{T}| \sum_{k \in \tilde{K}_{\tilde{T}}} \tilde{\omega}_k \sum_{\tilde{T} \in \mathcal{T}_{\text{micro}}} |\tilde{T}| \sum_{l \in \tilde{K}_{\tilde{T}}} \tilde{\omega}_l \partial_{\tilde{U}\tilde{U}}^2 a(V)((\bar{U}, \tilde{U}), (\bar{U}, \tilde{U}))(\nu_1)(\nu_2)(\bar{q}_k, \tilde{q}_l) \right\} \Big),
\end{aligned}$$

A. Derivatives of two-scale functionals

$$\begin{aligned}
& \partial_{UP}^2 \mathbf{L}[V, U, P](\theta_1, \nu_1)(\theta_2, \nu_2) \\
&= \left(\left\{ -2 \sum_{\tilde{T} \in \mathcal{T}} |\tilde{T}| \sum_{k \in \tilde{K}_{\tilde{T}}} \tilde{\omega}_k \sum_{\tilde{T} \in \mathcal{T}_{\text{micro}}} |\tilde{T}| \sum_{l \in \tilde{K}_{\tilde{T}}} \tilde{\omega}_l \partial_{\tilde{U}\tilde{P}}^2 a(V)((\tilde{U}, \tilde{U}), (\tilde{P}, \tilde{P}))(\theta_1)(\theta_2)(\tilde{q}_k, \tilde{q}_l), \right. \right. \\
& \quad \left. \left. -2 \sum_{\tilde{T} \in \mathcal{T}} |\tilde{T}| \sum_{k \in \tilde{K}_{\tilde{T}}} \tilde{\omega}_k \sum_{\tilde{T} \in \mathcal{T}_{\text{micro}}} |\tilde{T}| \sum_{l \in \tilde{K}_{\tilde{T}}} \tilde{\omega}_l \partial_{\tilde{U}\tilde{P}}^2 a(V)((\tilde{U}, \tilde{U}), (\tilde{P}, \tilde{P}))(\theta_1)(\nu_2)(\tilde{q}_k, \tilde{q}_l) \right\}, \right. \\
& \quad \left. \left\{ -2 \sum_{\tilde{T} \in \mathcal{T}} |\tilde{T}| \sum_{k \in \tilde{K}_{\tilde{T}}} \tilde{\omega}_k \sum_{\tilde{T} \in \mathcal{T}_{\text{micro}}} |\tilde{T}| \sum_{l \in \tilde{K}_{\tilde{T}}} \tilde{\omega}_l \partial_{\tilde{U}\tilde{P}}^2 a(V)((\tilde{U}, \tilde{U}), (\tilde{P}, \tilde{P}))(\nu_1)(\theta_2)(\tilde{q}_k, \tilde{q}_l), \right. \right. \\
& \quad \left. \left. -2 \sum_{\tilde{T} \in \mathcal{T}} |\tilde{T}| \sum_{k \in \tilde{K}_{\tilde{T}}} \tilde{\omega}_k \sum_{\tilde{T} \in \mathcal{T}_{\text{micro}}} |\tilde{T}| \sum_{l \in \tilde{K}_{\tilde{T}}} \tilde{\omega}_l \partial_{\tilde{U}\tilde{P}}^2 a(V)((\tilde{U}, \tilde{U}), (\tilde{P}, \tilde{P}))(\nu_1)(\nu_2)(\tilde{q}_k, \tilde{q}_l) \right\} \right),
\end{aligned}$$

$$\begin{aligned}
& \partial_{PP}^2 \mathbf{L}[V, U, P](\theta_1, \nu_1)(\theta_2, \nu_2) = \\
& \left(\left\{ 0, -2 \sum_{\tilde{T} \in \mathcal{T}} |\tilde{T}| \sum_{k \in \tilde{K}_{\tilde{T}}} \tilde{\omega}_k \sum_{\tilde{T} \in \mathcal{T}_{\text{micro}}} |\tilde{T}| \sum_{l \in \tilde{K}_{\tilde{T}}} \tilde{\omega}_l \partial_{\tilde{P}\tilde{P}}^2 a(V)((\tilde{U}, \tilde{U}), (\tilde{P}, \tilde{P}))(\theta_1)(\nu_2)(x, y) \, dx \right\}, \right. \\
& \quad \left. \left\{ -2 \sum_{\tilde{T} \in \mathcal{T}} |\tilde{T}| \sum_{k \in \tilde{K}_{\tilde{T}}} \tilde{\omega}_k \sum_{\tilde{T} \in \mathcal{T}_{\text{micro}}} |\tilde{T}| \sum_{l \in \tilde{K}_{\tilde{T}}} \tilde{\omega}_l \partial_{\tilde{P}\tilde{P}}^2 a(V)((\tilde{U}, \tilde{U}), (\tilde{P}, \tilde{P}))(\nu_1)(\theta_2)(x, y) \, dx, 0 \right\} \right).
\end{aligned}$$

Bibliography

- [AD14] G. Allaire and C. Dapogny. A linearized approach to worst-case design in parametric and geometric shape optimization. *Math. Models Methods Appl. Sci.*, 24(11):2199–2257, 2014.
- [AD15] G. Allaire and C. Dapogny. A deterministic approximation method in shape optimization under random uncertainties. working paper or preprint, June 2015.
- [AF03] R. A. Adams and J. J. F. Fournier. *Sobolev spaces*, volume 140 of *Pure and Applied Mathematics (Amsterdam)*. Elsevier/Academic Press, Amsterdam, second edition, 2003.
- [AFP00] L. Ambrosio, N. Fusco, and D. Pallara. *Functions of bounded variation and free discontinuity problems*. Oxford Mathematical Monographs. Oxford University Press, New York, 2000.
- [AG11] A. Abdulle and M. J. Grote. Finite element heterogeneous multiscale method for the wave equation. *Multiscale Model. Simul.*, 9(2):766–792, 2011.
- [Ahm06] S. Ahmed. Convexity and decomposition of mean-risk stochastic programs. *Math. Program.*, 106(3, Ser. A):433–446, 2006.
- [AJ05] G. Allaire and F. Jouve. A level-set method for vibration and multiple loads structural optimization. *Comput. Methods Appl. Mech. Engrg.*, 194(30-33):3269–3290, 2005.
- [All02] G. Allaire. *Shape optimization by the homogenization method*, volume 146 of *Applied Mathematical Sciences*. Springer-Verlag, New York, 2002.
- [Alt06] H. W. Alt. *Lineare Funktionalanalysis*. Springer Verlag, fifth edition, 2006.
- [AR15] T. Asamov and A. Ruszczyński. Time-consistent approximations of risk-averse multistage stochastic optimization problems. *Math. Program.*, 153(2, Ser. A):459–493, 2015.
- [Arm66] L. Armijo. Minimization of functions having Lipschitz continuous first partial derivatives. *Pacific Journal of Mathematics*, 16(1):1–3, 1966.

Bibliography

- [AVCT07] R. Ansola, E. Veguería, J. Canales, and J. A. Tárrago. A simple evolutionary topology optimization procedure for compliant mechanism design. *Finite Elements in Analysis and Design*, 44(1–2):53–62, 2007.
- [Ben95] M. P. Bendsøe. *Optimization of structural topology, shape, and material*. Springer-Verlag, Berlin, 1995.
- [BMRM16] F. Belzunce, C. Martínez-Riquelme, and J. Mulero. *An introduction to stochastic orders*. Elsevier/Academic Press, Amsterdam, 2016.
- [Bra02] A. Braides. Γ -convergence for beginners, volume 22 of *Oxford Lecture Series in Mathematics and its Applications*. Oxford University Press, Oxford, 2002.
- [Bra06] A. Braides. *A Handbook of Γ -Convergence*, volume III of *Handbook of differential equations: stationary partial differential equations*. Elsevier/North-Holland, Amsterdam, 2006.
- [BT10a] C. Barbarosie and A.-M. Toader. Shape and topology optimization for periodic problems. I. The shape and the topological derivative. *Struct. Multidiscip. Optim.*, 40(1-6):381–391, 2010.
- [BT10b] C. Barbarosie and A.-M. Toader. Shape and topology optimization for periodic problems. II. Optimization algorithm and numerical examples. *Struct. Multidiscip. Optim.*, 40(1-6):393–408, 2010.
- [BT14] C. Barbarosie and A.-M. Toader. Optimization of bodies with locally periodic microstructure by varying the periodicity pattern. *Netw. Heterog. Media*, 9(3):433–451, 2014.
- [BTN02] A. Ben-Tal and A. Nemirovski. Robust optimization—methodology and applications. *Math. Program.*, 92(3, Ser. B):453–480, 2002. ISMP 2000, Part 2 (Atlanta, GA).
- [CD99] D. Cioranescu and P. Donato. *An Introduction to Homogenization*. Oxford University Press, Oxford, 1999.
- [CDHR08] Y. Chen, T. A. Davis, W. W. Hager, and S. Rajamanickam. Algorithm 887: Cholmod, supernodal sparse cholesky factorization and update/downdate. *ACM Trans. Math. Softw.*, 35(3):22:1–22:14, October 2008.
- [CGLR17] S. Conti, B. Geihe, M. Lenz, and M. Rumpf. A posteriori modeling error estimates in the optimization of two-scale elastic composite materials. *ESAIM: Mathematical Modelling and Numerical Analysis*, 2017. to appear.

- [CGRS14] S. Conti, B. Geihe, M. Rumpf, and R. Schultz. Two-stage stochastic optimization meets two-scale simulation. In G. Leugering, P. Benner, S. Engell, A. Griewank, H. Harbrecht, M. Hinze, R. Rannacher, and S. Ulbrich, editors, *Trends in PDE Constrained Optimization*, volume 165 of *International Series of Numerical Mathematics*, pages 193–211. Springer International Publishing, 2014.
- [CGS09] M. Carrión, U. Gotzes, and R. Schultz. Risk aversion for an electricity retailer with second-order stochastic dominance constraints. *Comput. Manag. Sci.*, 6(2):233–250, 2009.
- [CHP⁺09] S. Conti, H. Held, M. Pach, M. Rumpf, and R. Schultz. Shape optimization under uncertainty - a stochastic programming perspective. *SIAM Journal on Optimization*, 19(4):1610–1632, 2009.
- [CHP⁺11] S. Conti, H. Held, M. Pach, M. Rumpf, and R. Schultz. Risk averse shape optimization. *SIAM Journal on Control and Optimization*, 49(3):927–947, 2011.
- [Cia88] P. G. Ciarlet. *Mathematical elasticity. Vol. I*, volume 20 of *Studies in Mathematics and its Applications*. North-Holland Publishing Co., Amsterdam, 1988. Three-dimensional elasticity.
- [CRST17] S. Conti, M. Rumpf, R. Schultz, and S. Tölkes. Stochastic dominance constraints in elastic shape optimization. preprint, 2017.
- [DDH15] M. Dambrine, C. Dapogny, and H. Harbrecht. Shape optimization for quadratic functionals and states with random right-hand sides. *SIAM Journal on Control and Optimization*, 53(5):3081–3103, 2015.
- [DGG⁺11] D. Drapkin, R. Gollmer, U. Gotzes, F. Neise, and R. Schultz. Risk management with stochastic dominance models in energy systems with dispersed generation. In *Stochastic optimization methods in finance and energy*, volume 163 of *Internat. Ser. Oper. Res. Management Sci.*, pages 253–271. Springer, New York, 2011.
- [DHR98] G. P. Dias, J. Herskovits, and F. A. Rochinha. Simultaneous shape optimization and nonlinear analysis of elastic solids. *Computational Mechanics*, 1998.
- [DHR07] D. Dentcheva, R. Henrion, and A. Ruszczyński. Stability and sensitivity of optimization problems with first order stochastic dominance constraints. *SIAM Journal on Optimization*, 18:322–337, 2007.

Bibliography

- [DM93] G. Dal Maso. *An introduction to Γ -convergence*. Progress in Nonlinear Differential Equations and their Applications, 8. Birkhäuser Boston, Inc., Boston, MA, Boston, 1993.
- [DM01] J. Dreyer and L. Martinelli. Hydrodynamic shape optimization of propulsor configurations using continuous adjoint approach. *15th AIAA Computational Fluid Dynamics Conference*, Jun 2001.
- [DR03] D. Dentcheva and A. Ruszczyński. Optimization with stochastic dominance constraints. *SIAM J. Optim.*, 14(2):548–566 (electronic), 2003.
- [DR04] D. Dentcheva and A. Ruszczyński. Optimality and duality theory for stochastic optimization with nonlinear dominance constraints. *Mathematical Programming*, 99:329–350, 2004.
- [DR08] D. Dentcheva and A. Ruszczyński. Stochastic dynamic optimization with discounted stochastic dominance constraints. *SIAM Journal on Control and Optimization*, 47:2540–2556, 2008.
- [DR10] D. Dentcheva and A. Ruszczyński. Inverse cutting plane methods for optimization problems with second-order stochastic dominance constraints. *Optimization*, 59(3-4):323–338, 2010.
- [DR13] D. Dentcheva and W. Römisch. Stability and sensitivity of stochastic dominance constrained optimization models. *SIAM J. Optim.*, 23(3):1672–1688, 2013.
- [DR14] D. Dentcheva and A. Ruszczyński. Risk preferences on the space of quantile functions. *Math. Program.*, 148(1-2, Ser. B):181–200, 2014.
- [DS10] D. Drapkin and R. Schultz. An algorithm for stochastic programs with first-order dominance constraints induced by linear recourse. *Discrete Appl. Math.*, 158(4):291–297, 2010.
- [EE03] W. E and B. Engquist. The heterogeneous multiscale methods. *Commun. Math. Sci.*, 1(1):87–132, 2003.
- [EE05] W. E and B. Engquist. The heterogeneous multi-scale method for homogenization problems. In *Multiscale Methods in Science and Engineering*, volume 44 of *Lecture Notes in Computational Science and Engineering*, pages 89–110. Springer Berlin Heidelberg, 2005.
- [EEH03] W. E, B. Engquist, and Z. Huang. Heterogeneous multiscale method: A general methodology for multiscale modeling. *Physical Review B*, 67(9):1–4, March 2003.

- [EMZ05] W. E. P. Ming, and P. Zhang. Analysis of the heterogeneous multi-scale method for elliptic homogenization problems. *J. Amer. Math. Soc.*, 18(1):121–156, 2005.
- [FMRZ11] C. I. Fábían, G. Mitra, D. Roman, and V. Zverovich. An enhanced model for portfolio choice with SSD criteria: a constructive approach. *Quant. Finance*, 11(10):1525–1534, 2011.
- [GGS11] R. Gollmer, U. Gotzes, and R. Schultz. A note on second-order stochastic dominance constraints induced by mixed-integer linear recourse. *Math. Program.*, 126(1, Ser. A):179–190, 2011.
- [GK95] Y. Grabovsky and R. V. Kohn. Microstructures minimizing the energy of a two phase elastic composite in two space dimensions. I. The confocal ellipse construction. *J. Mech. Phys. Solids*, 43(6):933–947, 1995.
- [GNS08] R. Gollmer, F. Neise, and R. Schultz. Stochastic programs with first-order dominance constraints induced by mixed-integer linear recourse. *SIAM J. Optim.*, 19(2):552–571, 2008.
- [GRB03] J. Guedes, H. Rodrigues, and M. Bendsøe. A material optimization model to approximate energy bounds for cellular materials under multiload conditions. *Struct. Multidiscip. Optim.*, 25(5):446–452, 2003.
- [Has62] Z. Hashin. The elastic moduli of heterogeneous materials. *Trans. ASME Ser. E. J. Appl. Mech.*, 29:143–150, 1962.
- [HKLS10] J. Haslinger, M. Kočvara, G. Leugering, and M. Stingl. Multidisciplinary free material optimization. *SIAM Journal on Applied Mathematics*, 70(7):2709–2728, 2010.
- [HOV16] P. Henning, M. Ohlberger, and B. Verfürth. A new heterogeneous multiscale method for time-harmonic Maxwell’s equations. *SIAM J. Numer. Anal.*, 54(6):3493–3522, 2016.
- [HS07] V. Heuveline and F. Strauß. Hydrodynamic stability control in cfd by shape optimization. *PAMM*, 7(1):4140007–4140008, 2007.
- [Kri05] T. K. Kristoffersen. Deviation measures in linear two-stage stochastic programming. *Math. Methods Oper. Res.*, 62(2):255–274, 2005.
- [KW14] R. V. Kohn and B. Wirth. Optimal fine-scale structures in compliance minimization for a uniaxial load. In *Proceedings of the Royal Society of London A: Mathematical, Physical and Engineering Sciences*, volume 470, page 20140432. The Royal Society, 2014.

Bibliography

- [KW15] R. V. Kohn and B. Wirth. Optimal fine-scale structures in compliance minimization for a shear load. *Communications in Pure and Applied Mathematics*, 2015. to appear.
- [LCYC15] J. Liu, L. Cao, N. Yan, and J. Cui. Multiscale approach for optimal design in conductivity of composite materials. *SIAM J. Numer. Anal.*, 53(3):1325–1349, 2015.
- [LKH05] Z. Liu, J. G. Korvink, and R. Huang. Structure topology optimization: Fully coupled level set method via femlab. *Structural and Multidisciplinary Optimization*, 29:407–417, June 2005.
- [Lue08] J. Luedtke. New formulations for optimization under stochastic dominance constraints. *SIAM J. Optim.*, 19(3):1433–1450, 2008.
- [Lüt16] N. Lüthen. Numerical shape optimization of branching-periodic elastic structures. Master thesis, University of Bonn, 2016.
- [MBD⁺15] V. Müller, B. Brylka, F. Dillenberger, R. Glöckner, and T. Böhlke. Homogenization of elastic properties of short-fiber reinforced composites based on microstructure data. *J. Compos. Mater.*, 50(3):297–312, mar 2015.
- [Mel01] R. Melchers. Optimality-criteria-based probabilistic structural design. *Structural and Multidisciplinary Optimization*, 23(1):34–39, 2001.
- [Mil02] G. W. Milton. *The Theory of Composites*. Cambridge University Press, 2002.
- [MM77] L. Modica and S. Mortola. Un esempio di Γ^- -convergenza. *Boll. Un. Mat. Ital. B (5)*, 14(1):285–299, 1977.
- [MS02] A. Müller and D. Stoyan. *Comparison Methods for Stochastic Models and Risks*. Wiley, 2002.
- [MT85] F. Murat and L. Tartar. Calcul des variations et homogénéisation. In *Homogenization methods: theory and applications in physics (Bréau-sans-Nappe, 1983)*, volume 57 of *Collect. Dir. Études Rech. Élec. France*, pages 319–369. Eyrolles, Paris, 1985.
- [NA16] T. Nakazawa and H. Azegami. Shape optimization of flow field improving hydrodynamic stability. *Jpn. J. Ind. Appl. Math.*, 33(1):167–181, 2016.
- [NNWSA11] S. Nemat-Nasser, J. Wills, A. Srivastava, and A. Amirkhizi. Homogenization of periodic elastic composites and locally resonant materials. *Phys. Rev. B*, 83:104103, Mar 2011.

- [Ohl05] M. Ohlberger. A posterior error estimates for the heterogeneous multiscale finite element method for elliptic homogenization problems. *SIAM Multiscale Mod. Simul.*, 4(1):88–114, 2005.
- [Pac14] M. Pach. *Risikoaverse Formoptimierung - Risikomaße und stochastische Ordnungen*. Dissertation, Universität Duisburg-Essen, 2014.
- [PR07] G. C. Pflug and W. Römisch. *Modeling, Measuring and Managing Risk*. World Scientific, Singapore, 2007.
- [PRW12] P. Penzler, M. Rumpf, and B. Wirth. A phase-field model for compliance shape optimization in nonlinear elasticity. *ESAIM: Control, Optimisation and Calculus of Variations*, 18(1):229–258, 2012.
- [QM] AG Rumpf, Institute for Numerical Simulation, University of Bonn. *The QuocMesh library*.
- [RJA⁺99] J. J. Reuther, A. Jameson, J. J. Alonso, M. J. Rimlinger, and D. Saunders. Constrained multipoint aerodynamic shape optimization using an adjoint formulation and parallel computers, part 1. *Journal of Aircraft*, 36(1):51–60, Jan 1999.
- [RR08] G. Rudolf and A. Ruszczyński. Optimization problems with second order stochastic dominance constraints: duality, compact formulations, and cut generation methods. *SIAM J. Optim.*, 19(3):1326–1343, 2008.
- [RV08] W. Römisch and S. Vigerske. Quantitative stability of fully random mixed-integer two-stage stochastic programs. *Optim. Lett.*, 2(3):377–388, 2008.
- [Sam04] J. Samareh. Aerodynamic shape optimization based on free-form deformation. *10th AIAA/ISSMO Multidisciplinary Analysis and Optimization Conference*, Aug 2004.
- [Sha12] A. Shapiro. Time consistency of dynamic risk measures. *Oper. Res. Lett.*, 40(6):436–439, 2012.
- [SS09] V. Schulz and C. Schillings. On the nature and treatment of uncertainties in aerodynamic design. *AIAA Journal*, 47:646–654, 2009.
- [SS15] C. Schillings and V. Schulz. On the influence of robustness measures on shape optimization with stochastic uncertainties. *Optim. Eng.*, 16(2):347–386, 2015.
- [ST06] R. Schultz and S. Tiedemann. Conditional value-at-risk in stochastic programs with mixed-integer recourse. *Math. Program.*, 105(2-3):365–386, 2006.

Bibliography

- [SW00] J. A. Sethian and A. Wiegmann. Structural boundary design via level set and immersed interface methods. *Journal of Computational Physics*, 163(2):489–528, 2000.
- [Tar85] L. Tartar. Estimations fines des coefficients homogénéisés. In *Ennio De Giorgi colloquium (Paris, 1983)*, volume 125 of *Res. Notes in Math.*, pages 168–187. Pitman, Boston, MA, 1985.
- [Van15] O. Vantzos. Optimization of branching structures. (personal communication), 2015.
- [WB06] A. Wächter and L. T. Biegler. On the Implementation of a Primal-Dual Interior Point Filter Line Search Algorithm for Large-Scale Nonlinear Programming. *Mathematical Programming*, 106(1):25–57, 2006.